Albert-Ludwigs-Universität Freiburg

Controlled Inter-Site Coupling in a two-dimensional Ion Trap Array

Frederick Maximilian Hakelberg

aus Geilenkirchen

2019

Dissertation

zur Erlangung des Doktorgrades
der Fakultät für Mathematik und Physik
der Albert-Ludwigs-Universität Freiburg

Dekan:	Prof. Dr. Wolfgang Soergel
Betreuer & Erstgutachter:	Prof. Dr. Tobias Schätz
Zweitgutachter:	PD Dr. Markus Walther
Tag der mündlichen Prüfung:	26. November 2019
Prüfer:	Prof. Dr. Marc Schumann
	apl. Prof. Dr. Thomas Filk
	Prof. Dr. Tobias Schätz

Abstract

The understanding of quantum mechanical systems is essential to modern physics and its applications. However, already for entangled systems of a few tens of constituents, exact numerical simulations on classical computers can become impossible. Quantum simulators based on well-controlled quantum system might provide the only effective approach to these systems. Trapped atomic ions offer a uniquely precise and controllable platform. They are used as platforms for, e.g., future quantum computers, quantum simulators, and extremely precise clocks. Quantum-simulation problems of interest and out-of-reach for modern theoretical methods include the dynamics of one-dimensional systems on long time scales and more-than-one dimensional systems with long-range interaction. For the latter, two-dimensional arrays of ions, individually trapped and controlled above microfabricated surface-electrode traps, present a promising approach. In the first realizations so far, the inter-site distance between the ions was too large to allow for sufficient inter-site coupling. We aim for a scalable approach to an analog quantum simulator based on a two-dimensional array of individually trapped ions. As a first demonstration, we operate an array of three magnesium ions in triangular arrangement with a side-length of 40 µm. Therein, we previously demonstrated the individual control of internal (electronic) and external (motional) degrees of freedom of the ions. Here, we present the first realization of inter-site coupling in the two-dimensional array. We demonstrate the coupling by a transfer of large coherent states of motion between the sites. We investigate the influence of the amplitude of these motional states in the anharmonic trapping potential and extrapolate to future experiments on the single-phonon level. We apply the real-time control of the coupling and concatenate the two-site coupling to transfer motional excitation between all three sites of the array. To demonstrate the scalability of our techniques, we couple all three sites simultaneously and investigate the evolution of an initial excitation at one and two sites of the array. The latter shows interference effects of the different pathways in the triangle. Current motional heating rates on the order of the inter-site coupling, preclude working with single phonons near the motional ground-state. We present a new experimental apparatus and vacuum chamber which will allow in-situ cleaning of surface-electrode traps. This has shown to reduce motional heating rates by two orders of magnitude. In this apparatus, we additionally realize a magnetic-field insensitive qubit in $^{25}Mg^{+}$ with a coherence time exceeding six seconds. We generate the magnetic field around 10.9 mT by a hybrid magnet assembly based on solid-state magnets and fine-tuned by electric coils. Once we have reduced the heating rate in the triangle trap array using the new setup, first quantum simulation experiments, investigating spin-frustration or artificial gauge fields, will come in reach. Here our triangle represents a basic, scalable, building block of future latices designed at will.

Zusammenfassung

Das Verständnis quantenmechanischer Systeme ist grundlegend für die moderne Physik und ihre Anwendung. Jedoch sind exakte numerische Simulationen auf klassischen Computern bereits für verschränkte Systeme aus einigen zehn Bestandteilen unmöglich. Quanten Simulatoren, basierend auf gut kontrollierten Quanten Systemen, könnten den einzigen effizienten Zugang zu solchen Systemen bieten. Gefangene atomare Ionen bieten eine einzig artig präzise und kontrollierbare Plattform. Sie werden unter anderem als Plattform für zukünftige Quanten Computer, Quanten Simulatoren und extrem präzise Uhren verwendet. Quantensimulationsprobleme von Interesse, und außerhalb der Reichweite moderner theoretischer Methoden, betreffen die Dynamik eindimensionaler Systeme auf langen Zeitskalen und mehrdimensionale Systeme mit langreichweitiger Wechselwirkung. Für Letztere, bieten zweidimensionale Anordnungen von Ionen, individuell gefangen und kontrollierter über Mikrofabrizierten Oberflächenfallen, einen vielversprechenden Ansatz. In ersten Realisierungen solcher Fallen, waren die Abstände zwischen den einzelnen Ionen jedoch zu groß für eine ausreichende Wechselwirkung zwischen den einzelnen Ionen. Unser Ziel ist ein skalierbarer Ansatz für einen analogen Quanten Simulator basierend auf zweidimensional angeordneten, individuell gefangenen Ionen. Als erste Demonstration betreiben wir ein Array dreier Magnesium Ionen, angeordnet in einem Dreieck mit einer Seitenlänge von 40 µm. Darin demonstrierten wir bereits die individuelle Kontrolle interner (elektronischer) und externer (bewegungs) Freiheitsgrade der Ionen. In dieser Arbeit präsentieren wir die erste Umsetzung einer Wechselwirkung zwischen einzelnen Ionen in einem zweidimensionalen Array. Wir demonstrieren diese Wechselwirkung durch den Transfer kohärenter Bewegungszustände von großer Amplitude. Wir untersuchen den Einfluss dieser Amplitude im anharmonischen Fallenpotential und extrapolieren zu zukünftigen Experimenten auf dem Level einzelner Photonen. Wir verwenden die Echtzeitkontrolle der Kopplung um die Kopplung zwischen zwei Ionen wiederholt auszuführen und so Bewegungszustände zwischen allen drei Ionen zu transferieren. Um die Skalierbarkeit unserer Techniken zu demonstrieren, koppeln wir alle drei Ionen gleichzeitig und untersuchen die Entwicklung einer anfänglichen Anregung von einem und zwei Ionen. Letzteres zeigt Interferenzeffekte aufgrund der möglichen Pfade im Dreieck. Derzeit hindern uns Heizraten der Bewegungsfreiheitsgrade, von Größenordnung der Kopplungsrate, daran, die Kopplung mit einzelnen Phononen durchzuführen. Wir präsentieren einen neuen Experimentellen Aufbau und eine Vakuumkammer, welche das Reinigen der Oberflächenfalle, im eingebauten Zustand, erlauben wird. Es wurde gezeigt, dass dies Heizraten um bis zu zwei Größenordnungen reduzieren kann. Zusätzlich, realisieren wir in diesem Aufbau ein magnetfeldinsensitives Qubit in $^{25}Mg^{+}$ mit einer Kohärenzzeit von über sechs Sekunden. Wir erzeugen dieses Magnetfeld von rund 10.9 mT mithilfe eines Hybridaufbaus basierend auf Permanentmagneten und elektrischen Spulen zur Feinjustage. Sobald wir mithilfe des neuen Aufbaus, die Heizrate in der Dreickesfalle reduziert haben, kommen erste Quantensimulationsexperimente, von Spin-frustration oder künstlicher Eichfelder, in Reichweite. Für dies stellt unser Dreieck einen elementaren, skalierbaren, Baustein zukünftiger, nach Belieben entworfener, Gitter dar.

Contents

1 Introduction

Quantum mechanics is required to describe many experimental observations in the smallest physical systems. The theory allows access to unintuitive phenomena such as superposition and entanglement. While we do not directly observe such effects in everyday life, quantum mechanics is relevant to many modern technologies. These include, for example, superconductivity, lasers, the understanding of photosynthesis, and the construction of modern computer chips where transistor sizes are reaching down to a few nanometres. For quantum mechanical systems, the information scales exponentially with the system size (Nielsen and Chuang 2010). This limits the ability to perform numerical calculations for such systems or even simply to save the systems state at one instance of time on a classical memory. Already Richard Feynman proposed to simulate quantum mechanical systems not on a classical computer but to construct a similar, but well-controlled quantum system to gain insights into the system of interest (Feynman 1982). Today Quantum Simulations have become an active field of research, roughly separable into two classes of simulators: The first are digital quantum simulators (DQS), where the system is programmed onto a quantum computer and the dynamics are replaced by a discrete set of gates (Lloyd 1996). Up to now only small proof-of-concept systems of quantum computers with a few qubits have been realized (Gulde et al. 2003; Helmer et al. 2009; Yao et al. 2012) and it is still a long way to a universal quantum computer with a suitable number of error-corrected qubits and high-fidelity gate operations. The second type are analog quantum simulators (AQS), more closely to Feynman's original idea: Here one aims to experimentally realize a quantum system that resembles the system of interest but allows for precise control including the preparation, manipulation, and detection of the state of the system. This AQS, while not being a universal simulator but tailored to a specific class of problems, might be easier to construct (Buluta and Nori 2009) and more robust against imperfections (Cirac and Zoller 2012). Similar to the DiVincenzo criteria (DiVincenzo 2000) for a universal quantum computer, Cirac and Zoller (2012) list the following five criteria for an AQS: (1) A quantum system of multiple (quantum) particles, which (2) can be prepared in a known state. Then (3) interactions either external or within the system can be made by local and global control of the particles, followed by (4) detection of the final state of the system. Finally, (5) these results should be compared to known solutions, where possible, and AQS based on different physical platforms. Several platforms have been investigated for realizing such an AQS, including photons using waveguide technology (Aspuru-Guzik and Walther 2012), neutral atoms stored in three-dimensional optical lattices (Barredo et al. 2018), superconducting qubits (Roushan et al. 2017), and trapped ions in Paul (Bernien et al. 2017; Zhang et al. 2017), and Penning traps (Britton et al. 2012). For an extensive

overview of quantum simulations, investigated platforms and applications we refer to the review article by Georgescu et al. (2014).

Trapped ions provide one of the most promising platforms for envisioned quantum computers and simulators. They are identical particles and experimental techniques are available which allow for precise, high-fidelity control of internal (electronic) and external (motional) degrees of freedom (Leibfried et al. 2003; Wineland et al. 1998). Trapped ions are investigated for instance as a platform of future quantum computers (Cirac and Zoller 1995; Kielpinski et al. 2002) but are also used in the most stable clocks to date (Brewer et al. 2019; Huntemann et al. 2016). Early on trapped ions have been proposed as a platform for quantum simulations where the electronic degrees of freedom can simulate spin-1/2 systems, while motional degrees of freedom represent (quantum) harmonic oscillators (Blatt and Roos 2012; Porras and Cirac 2004; Schaetz et al. 2007, 2004, 2013; Schmitz et al. 2009a; Schneider et al. 2012). With first experimental realisations of the quantum Ising model (Friedenauer et al. 2008; Kim et al. 2010) or the quantum random walk (Schmitz et al. 2009b; Zähringer et al. 2010). Up to now, all these experiments have been performed in linear Paul traps on one-dimensional Coulomb crystals with up to approximately 50 ions (Bernien et al. 2017; Zhang et al. 2017).

Cirac and Zoller (2012) and Hauke et al. (2012) state two classes of problems which lie beyond what is solvable numerically by modern theoretical techniques: The first one being the simulation of the long-term evolution of closed or open systems, and the second one, strongly entangled, multi-dimensional systems. The first can be already realized in one-dimensional systems as done, for example, in Clos et al. (2016) reaching beyond numerical tractability by increasing an effective system size. We aim towards the latter class of problems of realizing an AQS by a fully-connected two-dimensional lattice of individually trapped ions coupled at long range. Therein quantum spin Hamiltonians can be studied, but also the motional degrees of freedom can be harnessed to investigate for instance transport phenomena (Bermudez and Schaetz 2016; Bermudez et al. 2012) or spin-boson models (Porras et al. 2008). In Figure 1.1 we schematically sketch the idea of assembling a fully connected lattice based on our prototype of a triangular array of individually trapped ions. The scalable approach allows to preserve the controllability and performance of single trapped ions while increasing the system in two dimensions. Here our triangle trap is a basic building block of future lattices.

Surface-electrode ion traps (Chiaverini et al. 2005; Seidelin et al. 2006) where, inspired by neutral-atom chips (Dekker et al. 2000; Folman et al. 2000; Müller et al. 1999), all electrodes lie in a single common chip plane, are today slowly replacing the conventional, three-dimensional Paul trap design. They allow for modern microfabrication and engineering capabilities developed, e.g. in the field of computer chips. Still, most implementations aim towards linear traps where a linear chain of ions is confined along a single potential minimum. Early on also two-dimensional trapping structures have been proposed based on an array of microtraps (Chiaverini and Lybarger 2008; Cirac and Zoller 2000; DeVoe 1998; Schaetz et al. 2007). Here the idea is that the lattice structure is built from individual trapping sites filled with one or

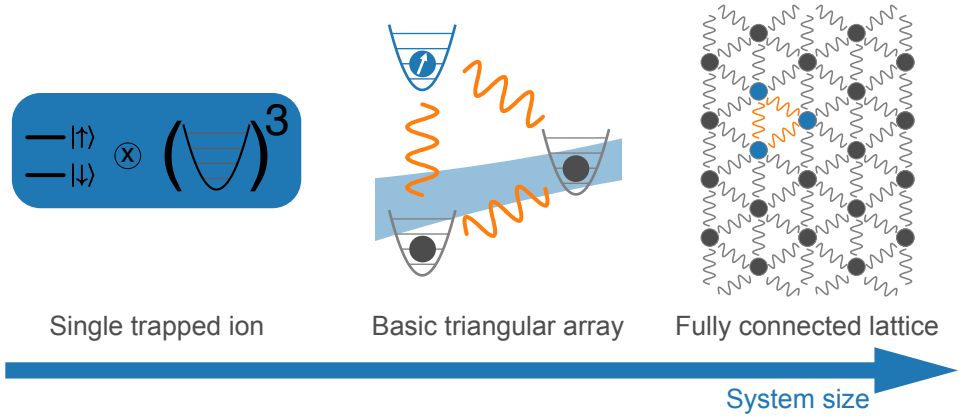

Figure 1.1: Scalable approach of a two-dimensional quantum simulator. Building on the remarkable results achieved in single trapped ions with internal (spin) and external (motional) degree of freedom we realize a basic triangular array. Therein we retain this performance of local and global control by focused lasers and electric control potentials while realizing the essential inter-site coupling. Our triangular array represents a basic building block of future large scale fully-connected lattices suitable for quantum simulations.

(optionally) multiple ions and individual sites are coupled via the Coulomb interaction of the individual charged ions in neighbouring sites. This coupling can be modelled by coupled harmonic oscillators where the coupling scales with the inter-site distance r as $1/r^3$. This stems from the fact that the coupling is induced by small variations of the ion positions around the equilibrium position, an effective dipole-dipole interaction. For suitable interaction timescales of (100–1000) µs, limited by coherence times of spin and motional degrees of freedom, the inter-site distance has to be smaller than approximately 50 µm. This coupling has been demonstrated between two sites in linear traps (Brown et al. 2011; Harlander et al. 2011) and was later used to implement an effective spin-spin coupling between the sites (Wilson et al. 2014). Several groups are working towards realizing two-dimensional arrays of single trapped ions (Bruzewicz et al. 2016; Clark et al. 2009; Jain et al. 2018; Kumph et al. 2016; Rattanasonti et al. 2013). However, so far, the inter-site distances realized therein are in the range of $r \approx$ (270–1500) µm limited by design and fabrication methods.

In a collaboration with the ion storage group at the National Institute of Standards and Technology (NIST, Boulder, CO), we presented two trap arrays each forming an equilateral triangle with side lengths of 40 µm and 80 µm respectively, fabricated by Sandia National Laboratories (Albuquerque, NM) (Mielenz et al. 2016). The traps follow a scalable approach in the numerical design of the electrode shapes and in fabrication which should allow scaling up to tens to hundred sites (Mielenz et al. 2016; Schmied et al. 2009). We demonstrated the individual control of the internal and external degrees of freedom of the single trapped ions including cooling to the motional ground-state by spin-motion coupling using local laser interactions, and local tuning of the trapping potential by electric control potentials. Following, we presented new

methods for the reconstruction of motional mode orientations of the single trapped ions which is essential for enabling tunable inter-site coupling (Kalis et al. 2016). Remaining limitations included limited coherence timescales of the internal (electronic) and external (motional) degrees of freedom (approx. 100 µs), where the latter are affected by fluctuations of motional frequencies and motional heating rates of typically 10 quanta/ms, and the missing realisation of the inter-site coupling.

In this thesis, we present the first realization of inter-site coupling in a scalable, two-dimensional prototype of an analogue quantum simulator based on individually trapped ions (published in Hakelberg et al. (2019)). We establish the necessary control techniques to implement the coupling and show the coherent exchange of coherent states of motion between sites of our array. To clearly demonstrate the coupling, we work with coherent states of large amplitude on the order of 1000 quanta, due to motional heating rates of several motional quanta within timescales of the exchange. For this, we develop an extended reconstruction method of the motional state amplitude based on site-specific calibration measurements. On the scale of the motional amplitude of these states, the trapping potential features anharmonic contributions, which alter the observed coupling. We analyse this systematically and extrapolate to the regime of low excitation, which we find in agreement with calculations for harmonically trapped ions. To further investigate the real-time control of the coupling we concatenate the two-site coupling protocol to transfer motional excitation between all three sites of our array. Furthermore, we employ the simultaneous control at all three trapping sites to implement global coupling of all sites. Here we investigate the evolution of an initial motional excitation at one or two sites of the array. The latter displays interference effects of the coherent states along the different pathways in the array dependent on the relative phase difference between the initial excitations. Additionally, we describe the construction and operation of a new experimental apparatus and vacuum chamber compatible with our traps that incorporates the ability of in-situ cleaning of the trap by bombardment with argon-ions which has been shown, in other groups with comparable devices, to reduce motional heating rates by two-orders of magnitude (Hite et al. 2012). In this experimental apparatus we realize a magnetic-field insensitive transition (qubit) (C. Langer et al. 2005) in $^{25}Mg^{+}$ ions using a novel hybrid setup to generate a magnetic field of 10.9 mT and find a coherence timescale of 6.6(9) s (published in Hakelberg et al. (2018)). We employ this qubit to perform a first exemplary quantum sensing experiment of oscillating magnetic fields which we attribute to stray currents in the radio-frequency electrode of the trap.

Outline In Chapter 2 we discuss the essential theories and methods relevant to this thesis. We start with the internal (spin) degree of freedom (Section 2.2) where we introduce the magnetic field-independent qubit, and methods for state preparation, manipulation, and coherence measurement. In Section 2.3 we explain the underlying principles of Paul traps and introduce surface-electrode ion traps, especially trap arrays and the design methods. We introduce the traps used for this thesis and considerations for the design of future traps. In Section 2.4 we describe the control of

motional degrees of freedom of the trapped ions. This includes Doppler cooling and methods for the preparation and detection of coherent states. We introduce control potentials and the underlying calculations, followed by the methods we use to control and analyse the orientations and frequencies of motional modes. In Section 2.5 we derive the theory of coupled harmonic oscillators describing the coupling of single trapped ions in our array. In Chapter 3 we summarize the experimental setup starting with the control system and laser setup. After a short summary of the established vacuum chamber housing the triangle trap array, we describe the design and assembly of the new experimental apparatus including a new vacuum chamber and a hybrid magnetic field setup (Section 3.3). In Section 3.4 we present the results obtained in this new setup with regards to realizing a magnetic-field independent qubit using a combination of solid-state magnets and coils, which we published in Hakelberg et al. (2018). In Chapter 4 we present the main results of this thesis, the realization of inter-site coupling in the triangle trap array, published in Hakelberg et al. (2019). Starting from the basics of coupling two sites (Section 4.1) we follow by a systematic study of the effect of anharmonic contributions to the trapping potential on the coupling (Section 4.2). We extend this coupling to two dimensions by employing the real-time individual controllability in our array: In Section 4.3 we demonstrate real-time tuning of the coupling to transfer motional excitation in the triangle trap array, while in Section 4.4 we demonstrate simultaneous coupling of all three sites showing interference effects of multiple motional excitations in the array. In Chapter 5 we summarize the findings and give an outlook towards future improvements and the prospects for experimental applications.

Personal contribution I started working at the triangle-trap experiment with the senior doctoral candidates Manuel Mielenz and Henning Kalis. I participated in the first publication demonstrating the trap architecture and showing the first results of individual control (Mielenz et al. 2016). There, my contribution was the reconstruction of motional states and motional mode configurations from two-photon stimulated Raman transitions. Together with Henning Kalis as a first author, I published a novel technique to measure the orientation of motional modes of single trapped ions by coherent excitation via control electrodes (Kalis et al. 2016) where I participated in the measurements and the analysis of results. I took over the experiment from Henning Kalis and was joined by the doctoral student Philip Kiefer. I continued to operate the experimental system which includes maintaining and improving the optical (laser) and electronic setup, and performing measurements and analysing results. Together with Philip Kiefer, I measured and analysed the results presented in this thesis (Chapter 4), which we published (equally contributing) in Hakelberg et al. (2019). Building on these results, Philip Kiefer and I realized phonon-assisted coupling in the triangular trap array which led to a second shared publication (equally contributing) Kiefer et al. (2019) and is presented in Philip Kiefer's dissertation (Kiefer 2019).

In parallel to these experiments, I designed a new vacuum chamber for surface-electrode traps incorporating an argon-ion gun which can be used to for in-situ cleaning

of traps to reduce motional heating rates (presented in Section 3.3). Raphaël Saint-Jalm started characterizing the argon-ion gun during an internship in our group and I continued these characterizations. I designed the vacuum chamber, managed the production of parts in the mechanical workshop of the physics institute and assembled the chamber. I set up the necessary optics, electronics and data-acquisition system for controlling the experiment and implemented ablation loading. I supervised the master student Leonard Nitzsche who helped in setting up the experiment and characterized the ablation loading; and the bachelor student Valentin Vierhub-Lorenz who designed and constructed the imaging optics. I designed and constructed the hybrid-magnetic system and, together with Philip Kiefer, characterized the system, performed the measurements and analysed the results presented in Section 3.4. Additionally, we performed ground-state cooling and heating-rate measurements in this new chamber, results that are not part of this thesis. Currently, we are preparing the setup for first argon-ion cleaning experiments.

Publications

As first author or equally contributing with first author

Hakelberg, F., Kiefer, P., Wittemer, M., Warring, U. and Schaetz, T., 'Interference in a Prototype of a Two-Dimensional Ion Trap Array Quantum Simulator', Physical Review Letters **123** (2019) 10.1103/PhysRevLett.123.100504.

Hakelberg, F., Kiefer, P., Wittemer, M., Schaetz, T. and Warring, U., 'Hybrid setup for stable magnetic fields enabling robust quantum control', Scientific Reports **8** (2018) 10.1038/s41598-018-22671-5.

Kiefer, P., Hakelberg, F., Wittemer, M., Bermúdez, A., Porras, D., Warring, U. and Schaetz, T., 'Floquet-Engineered Vibrational Dynamics in a Two-Dimensional Array of Trapped Ions', Physical Review Letters **123** (2019) 10.1103/PhysRevLett.123.213605.

As a co-author

Mielenz, M., Kalis, H., Wittemer, M., Hakelberg, F., Warring, U., Schmied, R., Blain, M., Maunz, P., Moehring, D. L., Leibfried, D. and Schaetz, T., 'Arrays of individually controlled ions suitable for two-dimensional quantum simulations', Nature Communications **7**, 11839 (2016) 10.1038/ncomms11839.

Kalis, H., Hakelberg, F., Wittemer, M., Mielenz, M., Warring, U. and Schaetz, T., 'Motional-mode analysis of trapped ions', Physical Review A **94** (2016) 10.1103/PhysRevA.94.023401.

Wittemer, M., Hakelberg, F., Kiefer, P., Schröder, J.-P., Fey, C., Schützhold, R., Warring, U. and Schaetz, T., 'Phonon Pair Creation by Inflating Quantum Fluctuations in an Ion Trap', Physical Review Letters **123** (2019) 10.1103/PhysRevLett.123.180502.

2 Theoretical and Experimental Methods

In this Chapter, we discuss the theoretical and experimental methods used in this thesis. Extensive literature is available on the field of trapped ions including the review articles by Leibfried et al. (2003) and Wineland et al. (1998) and we refer to these and cites therein for further details. In Table 2.1 we give an overview of the toolbox of single trapped ions, which allow to realize two quantum mechanical systems, the spin-1/2 system in internal (electronic) degrees of freedom and the three-dimensional harmonic oscillator in external (motional) degrees of freedom.

	Spin-1/2 system *E.g. hyperfine sub levels*	3D (harmonic) oscillator *Motional degrees of freedom*
Initialization	Optical pumping *Arbitrary superpositions*	Doppler & sideband cooling *Thermal, coherent, fock states*
Manipulation	Microwave & Raman transitions	Electric control potentials
	Spin-phonon coupling by Raman transitions	
Coherence	Clock states	Isolation from external noise
Detection	State selective detection	Fluorescence ($\bar{n} \gtrsim 100$ quanta) & state reconstruction

Table 2.1: The toolbox of (single) trapped ions. Both a spin-1/2 system and the harmonic oscillator system can be realized in internal and external degrees of freedom respectively. For the spin-1/2 system arbitrary superposition states can be prepared using optical pumping and by driving microwave and Raman transitions. Coherence can be increased by magnetic-field insensitive clock states and detection performed by state-selective detection. For the harmonic oscillator system cooling to the motional ground state and preparation of various motional states is possible. Electric control potentials allow to tune motional frequencies and motional mode orientations. State reconstruction can be performed for average motional amplitudes ($\bar{n}$) or on the single Fock state level. Both systems can be coupled (spin-phonon coupling) by driving motional-sensitive Raman transitions. For details see text and, e.g. Leibfried et al. (2003) and Wineland et al. (1998).

In the following, we describe general methods concerning these internal and external degrees of freedom of trapped ions. We summarize the techniques of ion traps, focusing on surface-electrode traps used in this thesis, including the design and fabrication. As essential control parameters, we describe the calculation and verification of electronic control potentials to tune the motional degrees of freedom of the trapped ions. We finish by a discussion of the theory of coupled harmonic oscillators as a description

of two ions trapped at two sites of our trap array and coupled via the Coulomb interaction.

2.1 Basic building blocks

Trapped ions allow the realisation of two basic building blocks of quantum mechanics. A two-level, or spin-1/2 system and the (three-dimensional) harmonic oscillator. Both systems can be used as building blocks of an envisioned quantum simulator. In the following, we summarize a subset of the theory of both systems as relevant to this thesis.

2.1.1 Two-level system

Two-level systems are one fundamental concept of quantum mechanics especially used as a model system. They are described by two states $|0\rangle$ and $|1\rangle$ with energy difference $\Delta E = \hbar\omega_0$ with the reduced planks constant $\hbar$ and corresponding frequency ω_0. With regard to spin$-1/2$ systems the states are often labelled $|\downarrow\rangle$ and $|\uparrow\rangle$ a convention we are using in this thesis.

Rabi oscillations

Following Sakurai (1994) a driving field oscillating with frequency ω_d can be used to drive transitions between these two states. Starting from an initial state $|\downarrow\rangle$ and for a resonant driving field, $\omega_\mathrm{d} = \omega_0$ the probability for the system to be in state $|\uparrow\rangle$ is given by:

$$P_{|\uparrow\rangle}(t) = \sin^2(\Omega/2\,t) \tag{2.1}$$

The system oscillates between the two states with the coupling rate Ω. These coherent oscillations are termed *Rabi Oscillations* after I. I. Rabi. For a detuned drive $\omega_\mathrm{d} \neq \omega_0$ with detuning $\Delta = \omega_\mathrm{d} - \omega_0$, Equation (2.1) changes to

$$P_{|\uparrow\rangle}(t, \Delta) = \frac{\Omega^2}{\Omega_\Delta^2} \sin^2(\Omega_\Delta/2\,t) \tag{2.2}$$

with the increased coupling rate

$$\Omega_\Delta = \sqrt{\Omega^2 + \Delta^2}$$

In Figure 2.1 we exemplarily sketch Equation (2.2) for variable detuning. We additionally plot the resonance line-shape observed when keeping the driving duration fixed at $t = \pi/\Omega$ and varying the detuning.

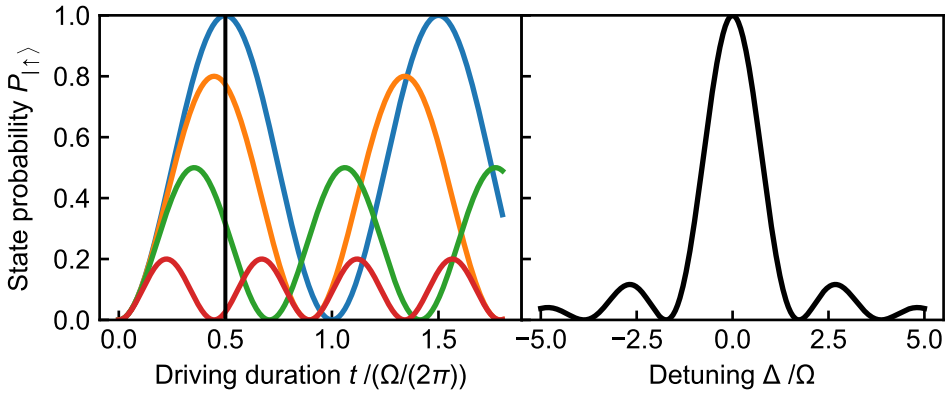

Figure 2.1: Rabi Oscillations of a driven two-level system. Initially in state $|\downarrow\rangle$ the driven system oscillates between states $|\downarrow\rangle$ and $|\uparrow\rangle$ (left). We plot these oscillations on resonance (blue line) and for three different detunings $\Delta = 0.5\,\Omega$ (orange line), $\Delta = \Omega$ (green line), and $\Delta = 2\,\Omega$ (red line). Additionally, for a fixed driving duration ($t = \pi/\Omega$, black vertical line), we plot the effect of a variable detuning (black line, right).

2.1.2 Three-dimensional harmonic oscillator

The harmonic oscillator is in two ways important for quantum simulations with trapped ions. On the one hand, a single trapped ion can be described by a three-dimensional harmonic oscillator, and on the other hand, the quantum harmonic oscillator is one of the essential concepts in quantum physics and a possible building block of analog quantum simulators.

In classical mechanics

In classical mechanics, the harmonic oscillator is given by a particle of mass m trapped in a harmonic potential. In one dimension (x) this potential is given by $V = 1/2\,kx^2$ and a corresponding position-dependent force $F(x) = -kx$. The particle, if not at rest, undergoes oscillations with a frequency $\omega = \sqrt{k/m}$. Extending to three dimensions with position $\boldsymbol{r}$ the general potential is given by

$$V(\boldsymbol{r}) = \frac{1}{2}\boldsymbol{r}^{\mathrm{T}}\boldsymbol{K}\boldsymbol{r} \tag{2.3}$$

With the 3×3 matrix $\boldsymbol{K}$. In the orthogonal eigenbasis $\{\hat{\boldsymbol{x}}, \hat{\boldsymbol{y}}, \hat{\boldsymbol{z}}\}$ of $\boldsymbol{K}$, the potential can be written as:

$$V(\boldsymbol{r}) = \frac{1}{2}(k_{\hat{\boldsymbol{x}}}\hat{\boldsymbol{x}}^2 + k_{\hat{\boldsymbol{y}}}\hat{\boldsymbol{y}}^2 + k_{\hat{\boldsymbol{z}}}\hat{\boldsymbol{z}}^2) \tag{2.4}$$

a superposition of three one-dimensional harmonic oscillators with three corresponding frequencies ω_i, $i \in \{\hat{\boldsymbol{x}}, \hat{\boldsymbol{y}}, \hat{\boldsymbol{z}}\}$, given by the eigenvalues λ_i of $\boldsymbol{K}$, $\lambda_i/m = \omega_i^2$. These three pairs of eigenvector and eigenvalue are known as the three motional modes of the particle, with mode vector $\boldsymbol{u_i}$ and frequency ω_i.

In quantum mechanics

For the quantum-mechanical three-dimensional harmonic oscillator, a similar separation in three one-dimensional oscillators can be made. We will here, therefore, consider the one-dimensional quantum harmonic oscillator, as relevant in the context of this thesis, and follow the introduction by Sakurai (1994). The corresponding Hamiltonian is given by:

$$H = \frac{p^2}{2m} + \frac{m\omega^2 x^2}{2} \tag{2.5}$$

with the momentum operator p and position operator x. With lowering and raising operators a and $a^\dagger$, and the number operator $N = a^\dagger a$, the Hamiltonian can be rewritten as:

$$H = \hbar\omega(N + \frac{1}{2}) \tag{2.6}$$

with eigenstates $|n\rangle$ with energy $E_n = (n + \frac{1}{2})\hbar\omega$. These are the Fock- or number states.

Coherent states of motion Following Carruthers (1965) coherent states of motion are defined by:

$$|\alpha\rangle = \exp\left(-\frac{1}{2}|\alpha|^2\right) \sum_{n=0}^{\infty} \frac{\alpha^n}{\sqrt{n!}} |n\rangle \tag{2.7}$$

where α is a complex value denoting oscillation amplitude and phase of the coherent state. The distribution over the number states follows a Poisson distribution:

$$P(n) = e^{-|\alpha|^2} \frac{|\alpha|^{2n}}{n!} \tag{2.8}$$

with expectation value (phonon number) $\bar{n} = |\alpha|^2$ which is equal to the variance of the distribution $\langle \Delta n^2 \rangle = \bar{n}$. These states correspond, for large α, to excitations of the classical harmonic oscillator. Coherent states of motion can be created by a resonant driving force acting on the particle, i.e. $F(t) \propto \sin(\omega t)$. In the context of trapped ions, one can make use of the electric charge of the ions and realize the driving force by an oscillating electric field. In Section 2.4.2 we describe our experimental tools for creating and detecting coherent states of motion.

2.2 The ion - electronic degrees of freedom

In our experiments we are working with magnesium ions (Mg^+). In the following, we summarize the electronic properties of the ion with a focus on the parts relevant to this work. For a detailed overview motivating the choice and explaining our usage of magnesium ions in our trapped-ion experiments we refer to Friedenauer (2010).

2.2.1 Level scheme

From the three naturally stable isotopes of magnesium with masses (24, 25, 26) u, we here work with $^{24}Mg^+$ and $^{25}Mg^+$. In Figure 2.2 we show an overview of the level scheme of magnesium ions as relevant to this thesis. A more involved level scheme including higher excited levels can be found in Clos (2017). Two excited states $P_{1/2}$

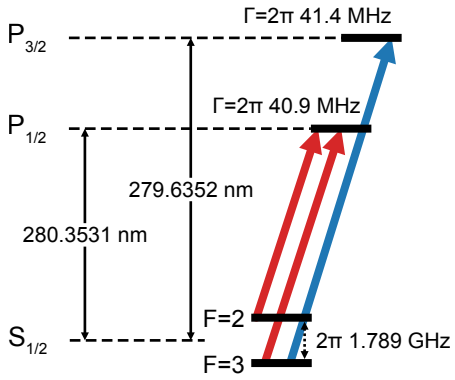

Figure 2.2: Subset of the finestructure of magnesium ions as relevant to this work. From the ground state $S_{1/2}$ transitions at around 280 nm connect to the excited $P_{1/2}$ and $P_{3/2}$ states with linewidths on the order of $2\pi \times 41$ MHz . For the $^{25}Mg^+$ isotope with nuclear spin $I = 5/2$ the ground $S_{1/2}$ state is further split into Hyperfine sublevels with a splitting of $2\pi \times 1.789$ GHz. We use lasers to drive transitions for Doppler cooling and state-detection (blue arrow) as well as repumping and state preparation (red arrows). Energies taken from Clos et al. (2014) and transition rates from Kelleher and Podobedova (2008).

and $P_{3/2}$ are accessible from the ground $S_{1/2}$ state by ultra-violet laser radiation around 280 nm. We employ lasers driving these transitions for Doppler cooling of the ions and state detection ($S_{1/2} \rightarrow P_{3/2}$) as well as state-preparation by repumping ($S_{1/2} \rightarrow P_{1/2}$). The isotopes $^{24}Mg^+$ and $^{26}Mg^+$ have a zero nuclear spin $I = 0$, while for $^{25}Mg^+$ $I = 5/2$. This leads to a hyperfine splitting of the $S_{1/2}$ state by $2\pi \times 1.789$ GHz which we use to implement a robust two-level system (see next Section). Additional lasers (not shown here) allow us to drive two-photon stimulated Raman transitions in the $S_{1/2}$ manifold via a virtual level detuned by several $2\pi \times 10$ GHz from the $P_{3/2}$ level.

2.2.2 Field independent qubit

A stable two-level system is one essential building block not only in our approach to scalable quantum simulations but also in other quantum simulation and computation applications. We implement this in the electronic degrees of freedom of $^{25}Mg^{+}$: We lift the degeneracy of the hyperfine states (see Figure 2.3) by an external magnetic quantization field and choose two levels labelled $|\uparrow\rangle$ and $|\downarrow\rangle$ of the $S_{1/2}$ manifold to realize a two-level system or qubit. These states have a (compared to experimental

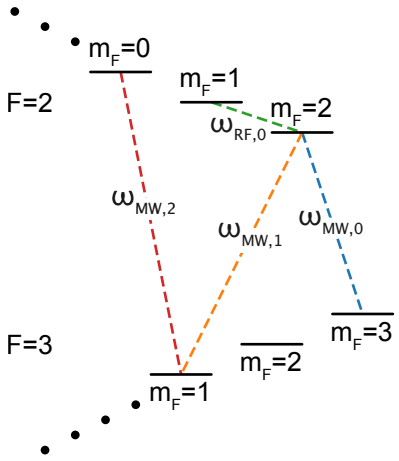

Figure 2.3: Hyperfine splitting of the $S_{1/2}$ ground state of $^{25}Mg^{+}$. The applied magnetic field of about 10.9 mT lifts the degeneracy of the hyperfine manifolds $F = 2$ and $F = 3$ and splits these into $(2F + 1)$ sublevels m_F (additional sublevels indicated as dots). Dashed lines indicate the transitions investigated in this work. We group these into microwave ($\omega_{MW,i}/(2\pi) \approx$ (1500–1700) MHz) and radio-frequency transitions ($\omega_{RF,i}/(2\pi) \approx 55$ MHz), based on their frequency. Corresponding energy splittings at this magnetic field are given in Table 3.2.

timescales) infinite lifetime on the order of 10^6 years (Kalis 2017). However, shifts in the energy difference E_Δ between the states can still lead to a dephasing of prepared states, limiting the timescale of experiments. The energy difference between the levels varies as a function of the magnetic field as calculated in detail in (for example) Kalis (2017). Here at selected points E_Δ becomes stationary as a function of the magnetic field strength $|\boldsymbol{B}_0|$, i.e.

$$\frac{dE_\Delta}{d\,|\boldsymbol{B}_0|} = 0$$

This allows the realization of a qubit that is first-order insensitive to magnetic field fluctuations. This significantly lowers the influence of fluctuations of the magnetic field strength, which can never be excluded completely in an experiment (Bollinger et al. 1991; C. Langer et al. 2005). For $^{25}Mg^{+}$ the lowest magnetic field to realize such a qubit, apart from $|\boldsymbol{B}_0| \approx 0$ T where the hyperfine sub levels states are degenerate, is at $|\boldsymbol{B}_0| \approx 10.9$ mT. Here the levels $|\downarrow\rangle = |F = 3, m_F = 1\rangle$ and $|\uparrow\rangle = |F = 2, m_F = 0\rangle$ become first-order insensitive with a splitting of $\omega_{MW,2} \approx 2\pi \times 1763$ MHz. While in

atomic physics experiments, magnetic fields are often realized with electric coils, in this work we present a realization based on a hybrid-setup where the main part of the magnetic field is realized by permanent magnets and fine-tuned by electric coils. In the triangle-trap setup, we use ferrite magnets generating a magnetic field of 4.66 mT (Kalis 2017).

2.2.3 State preparation, manipulation and detection

To prepare the ion in a defined state we employ the technique of optical pumping using dedicated laser beams. The σ^+-polarized beams couple the $S_{1/2}$ states to the $P_{1/2}$ level, increasing the m_F quantum number by one. From there the state decays with a rate of $\Gamma \approx 2\pi \times 41\,\mathrm{MHz}$ and $\Delta m_F \in \{-1, 0, +1\}$, on average increasing m_F by one. As there exists no $m_F = 4$ state in the $P_{1/2}$ manifold, the $|F = 3, m_F = 3\rangle$ state of $S_{1/2}$ is a dark state with respect to this laser frequency and the ion is *pumped* to this state. In the following, we use $|F, m_F\rangle$ as a short form for $S_{1/2}$ states, e.g. $|2, 2\rangle$.

To drive transitions between the states we employ microwave radiation resonant with the respective transition ($\Delta m_F \in \{-1, 0, +1\}$), with typical t_π times of (10–100) µs, i.e. the time needed to fully transfer the ion from one state to another. Alternatively, we can use two-photon stimulated Raman transitions where the states are coupled via two lasers tuned to a virtual level detuned by several $2\pi \times 10\,\mathrm{GHz}$ from $P_{3/2}$ (Leibfried et al. 2003). Additionally, in the new setup, we can drive $\Delta F = 0$ transitions, e.g. $|2, 2\rangle \leftrightarrow |2, 1\rangle$ using a radio-frequency voltage near $2\pi \times 55\,\mathrm{MHz}$ that we apply directly to the radio-frequency electrode at the trap side of the helical resonator (see Section 3.1.1). To prepare variable states we concatenate microwave transitions, e.g. $|3, 3\rangle \rightarrow |2, 2\rangle \rightarrow |3, 1\rangle$ to prepare the $|\downarrow\rangle$ state of the field-independent qubit.

To detect the electronic state, we use resonant light to detect the population of the $|3, 3\rangle$ state. We employ a σ^+-polarized laser resonant to the $|3, 3\rangle \leftrightarrow P_{3/2}$ transition with a decay rate of the excited state of $\Gamma \approx 2\pi \times 41\,\mathrm{MHz}$ and collect the scattered photons. Due to the detuning of more than $2\pi \times 1500\,\mathrm{MHz}$, the $|S_{1/2}, F = 2\rangle$ states are not excited by this laser. To perform detection of the field-independent qubit we implement a reversed preparation sequence $|3, 1\rangle \rightarrow |2, 2\rangle \rightarrow |3, 3\rangle$ to transfer the population of $|3, 1\rangle$ to the detected state $|3, 3\rangle$ before shining in the detection laser.

To infer the state populations we follow a method also described in C. E. Langer (2006). We perform the same experiment for several realizations on the order of $N_{\mathrm{exp}} = (100\text{–}1000)$ times. For each realization the ion is projected either into a bright ($|\downarrow\rangle$) or dark ($|\uparrow\rangle$) state. In the new setup during the detection interval of 100 µs, we collect on average around $\bar{N}_{|\downarrow\rangle} = 2.5$ photons for an ion in $|\downarrow\rangle$ and around $\bar{N}_{|\uparrow\rangle} = 0.2$ photons for an ion in $|\uparrow\rangle$. Both counts follow a Poisson distribution:

$$P(N|\bar{N}) = \frac{\bar{N}^N}{N!} e^{-\bar{N}} \tag{2.9}$$

giving the probability to collect N photons for an average of $\bar{N}$ photons. For an ion in a superposition state:

$$\Psi = \sqrt{\alpha} e^{-i\phi_{|\uparrow\rangle}} |\uparrow\rangle + \sqrt{(1-\alpha)} e^{-i\phi_{|\downarrow\rangle}} |\downarrow\rangle \tag{2.10}$$

with probability amplitude $\alpha \in [0;1]$, and arbitrary (real) phase factors $\phi_{|\uparrow\rangle}$ and $\phi_{|\downarrow\rangle}$, the count probability distribution is given by a sum of the two corresponding Poisson distributions:

$$P(N|\alpha) = \alpha P(N|\bar{N}_{|\uparrow\rangle}) + (1-\alpha)P(N|\bar{N}_{|\downarrow\rangle}) \tag{2.11}$$

To reconstruct the state populations from the data of an experimental sequence, with N_{data} data points with varied experimental parameters and N_{exp} experimental realisations per data point, we follow a two-step process. In the first step, we take the full dataset of $k = N_{\text{exp}} \times N_{\text{data}}$ entries with N_i counts each. We fit Equation 2.11 to this dataset by maximizing the log-likelihood function:

$$\begin{aligned}\log \mathcal{L}(\alpha, \bar{N}_{|\uparrow\rangle}, \bar{N}_{|\downarrow\rangle}) &= \log \prod_{i=1}^{k} P(N_i|\alpha, \bar{N}_{|\uparrow\rangle}, \bar{N}_{|\downarrow\rangle}) \\ &= \sum_{i=1}^{k} \log P(N_i|\alpha, \bar{N}_{|\uparrow\rangle}, \bar{N}_{|\downarrow\rangle})\end{aligned}$$

From this, we infer the two mean values $\bar{N}_{|\uparrow\rangle}$ and $\bar{N}_{|\downarrow\rangle}$ corresponding to the respective electronic states. In the second step, for each data point with N_{exp} entries we again fit Equation 2.11 by a log-likelihood fit, this time only varying α and setting $\bar{N}_{|\uparrow\rangle}$ and $\bar{N}_{|\downarrow\rangle}$ from the previous step. The first calibration step could, in theory, be done only once. In the experiment, however, fluctuations of, for instance, the detection laser intensities will affect the average counts on timescales of minutes.

To exemplarily demonstrate this technique, we consider data collected for driving the $|3,3\rangle \leftrightarrow |2,2\rangle$ transition for variable time t_{drive} followed by detection. The normalized histogram of the full experimental data shown in Figure 2.4 is fitted by the two Poisson distributions centred at $\bar{N}_{|2,2\rangle} = 0.207(5)$ and $\bar{N}_{|3,3\rangle} = 2.686(9)$. Keeping these values fixed we fit the probability amplitude α for each histogram corresponding to a fixed driving duration t_{drive} with 1000 entries each. The resulting data in Figure 2.5 of the probability of $|3,3\rangle$, $P_{|3,3\rangle}$ given by α shows coherent Rabi oscillations (cf. Section 2.1.1) between the states $|2,2\rangle$ and $|3,3\rangle$. We attribute the fact that $P_{|3,3\rangle}$ does not reach 0 or 1 to imperfect preparation of the initial state.

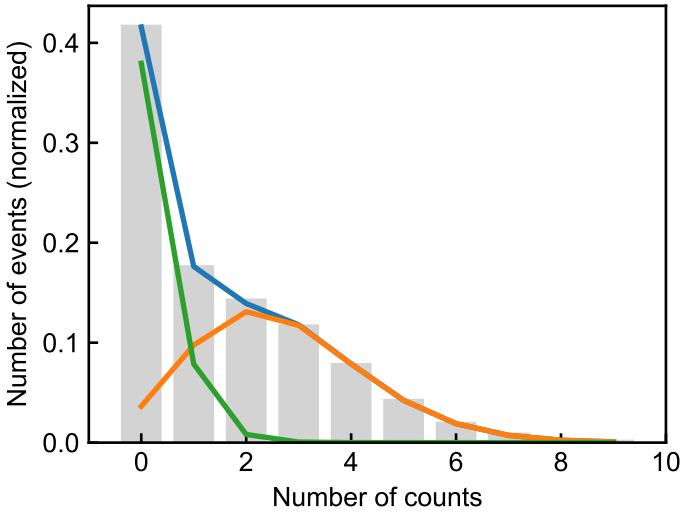

Figure 2.4: Exemplary state reconstruction histogram. From 50 000 experiments driving the transition for variable duration we plot the normalized histogram of the detected counts (grey bars). We fit the data by a sum (blue line) of two Poisson distributions corresponding to light scattered by state $|2,2\rangle$ (green line) and state $|3,3\rangle$ (orange line).

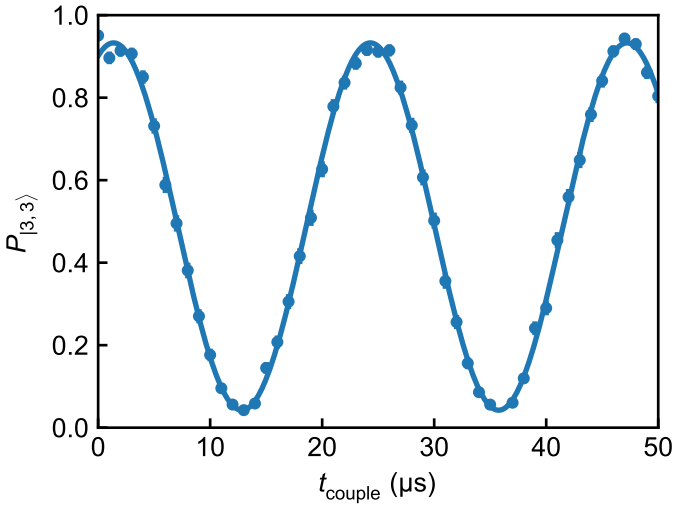

Figure 2.5: Rabi oscillations on the $|3,3\rangle \leftrightarrow |2,2\rangle$ transition. From 1000 experiments per data point we use the measured count histograms to reconstruct the probability for the ion to be in state $|\downarrow\rangle$. The resulting data shows Rabi oscillations with a period of about 25 µs. We attribute the initial deviation from $P_{|3,3\rangle} = 1$ to imperfect state preparation. As a guide to the eye we plot a sinusoidal model fit. The delayed onset of approximately 1.4 µs is explained by the rise-time of the microwave circuit which can be calibrated. Error bars (SEM) are smaller than the marker size.

2.2.4 Qubit coherence measurements

Long qubit coherence times, with respect to typical experimental sequences, are essential for envisioned quantum simulation experiments. In ion trap experiments coherence of the qubit is mostly limited by fluctuations of the magnetic quantization fields leading to fluctuations in the energy difference between the two-qubit states. As part of this work, we realized a stable first-order magnetic-field-insensitive qubit by a magnetic quantization field generated from solid-state magnets (results in Section 3.4). To quantify the coherence timescales, we perform two types of experiments explained in the following.

Ramsey experiment

The first experiment is a so-called *Ramsey experiment* proposed by Ramsey (1950). The experiment consists of two resonant pulses of duration $\pi/(2\Omega)$ driving the qubit transition where Ω refers to the Rabi rate. After preparation of, e.g. state $|\downarrow\rangle$, the first pulse prepares a superposition state of $1/\sqrt{(2)}(|\downarrow\rangle + |\uparrow\rangle)$. After a variable waiting duration T_{Ramsey} a second pulse of the same duration and with variable phase ϕ is applied. In the ideal case with resonant pulses and no fluctuations of the magnetic field, depending on ϕ the final state is either $|\uparrow\rangle$ ($\phi/(2\pi) = n$, for $n = 0, 1, 2, ..$), $|\downarrow\rangle$ ($\phi/(2\pi) = n(1 + 0.5)$, for $n = 0, 1, 2, ..$) or a variable supposition. The probability to find the system in state $|\downarrow\rangle$ after projection in the $|\downarrow\rangle/|\uparrow\rangle$ basis is given by:

$$P_{|\downarrow\rangle}(\phi) = \cos^2(\phi/2) \tag{2.12}$$

If we now consider noise, for instance of the quantization magnetic field amplitude, the energy splitting of the two states changes by a detuning $\Delta\omega_{\text{noise}}$. This leads to a phase of $\Delta\omega_{\text{noise}} \cdot T_{\text{Ramsey}}$ accumulated during the waiting duration T_{Ramsey}. Here we assume that the pulse durations are short compared to typical coherence timescales, i.e. the pulses are not affected by the detuning. For a single realisation of the experiment this shifts the probability distribution of Equation (2.12):

$$P_{|\downarrow\rangle}(\phi, T_{\text{Ramsey}}) = \cos^2\left[(\phi + \Delta\omega_{\text{noise}} \cdot T_{\text{Ramsey}})/2\right] \tag{2.13}$$

To simulate this in the context of an experiment we assume a Gaussian noise distribution of $\Delta\omega_{\text{noise}}$, i.e. of the underlying magnetic field amplitude noise. To extract state probabilities $P_{|\downarrow\rangle}$, in the experiment we repeat the same experiment several 100 times. To numerically illustrate this, for fixed T_{Ramsey} and variable ϕ, we sample 10 000 values of $\Delta\omega_{\text{noise}}$ from a Gaussian distribution with a width of $2\pi\times1\,\text{kHz}$ for each ϕ and calculate the average $P_{|\downarrow\rangle}(\phi, T_{\text{Ramsey}})$. We fit the resulting data by a $\cos^2$ function with a variable amplitude (contrast) C. In Figure 2.6 we show the resulting contrast as a function of T_{Ramsey}. The data is described by a Gaussian decay model:

$$C(T_{\text{Ramsey}}) = \exp\left[-\left(\frac{T_{\text{Ramsey}}}{\tau}\right)^2\right] \tag{2.14}$$

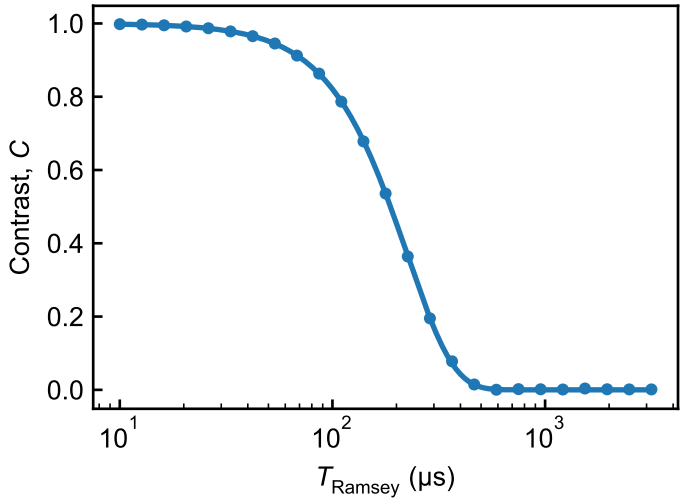

Figure 2.6: Exemplary numerical data extracted from simulating a Ramsey experiment with noise sampled from a Gaussian distribution (blue points). The calculated contrast decays with T_{Ramsey} following a Gaussian decay (blue line).

Here we introduce the coherence timescale τ. For the numerical data in Figure 2.6, we fit $\tau \approx 225\,\mu\text{s}$. In nuclear magnetic resonance experiments, this is often referred to as the T_2^* time.

Spin-echo experiment

An extension of the Ramsey experiment protocol was proposed shortly after by Erwin Hahn (Hahn 1950). Here in between the two pulses, after $T_{\text{Ramsey}}/2$, an additional pulse of duration π/Ω is applied. This pulse refocuses the effect of a detuning (for example, due to noise) that is constant during a single experimental realisation (i.e. during T_{Ramsey}): The phase accumulated during the first $T_{\text{Ramsey}}/2$ phase is cancelled out by the phase accumulated in the second half. Under noise constant within T_{Ramsey}, the resulting state will therefore always be the initial state $|\downarrow\rangle$. This allows one to investigate additional effects induced during one half of the experiment by, e.g. by displacing the ion.

2.3 The traps - surface-electrode ion traps

In 1989 Wolfgang Paul was awarded the Nobel prize (shared with Hans G. Dehmelt and Norman F. Ramsey) for his invention of the Paul trap to confine charged particles by rapidly oscillating electric fields. This technique is essential to the field of trapped ions. In the following, we will give a brief overview of the physics behind trapping ions in view of surface-electrode ion traps. We follow by a description of the traps used for the work presented here and finish with considerations for future trap designs.

2.3.1 Trapping ions

We consider a particle in a conservative, three-dimensional potential Φ. The particle is trapped at position $\boldsymbol{r}_0$ if changes of the particles position $\boldsymbol{r}_0 \to \boldsymbol{r}_0 + \boldsymbol{r}$ lead to a restoring force $\boldsymbol{F} \propto -\boldsymbol{r}$, effectively pushing it back. The lowest-order polynomial potential fulfilling these constraints is a harmonic potential. Setting $\boldsymbol{r}_0 = \mathbf{0}$ this potential is given by:

$$\Phi = \frac{1}{2}\, \boldsymbol{r}^{\mathrm{T}}\, \mathbf{H}\, \boldsymbol{r}$$

it is fully defined by the Hessian matrix

$$\mathbf{H}_{i,j} = \frac{\partial^2 \Phi}{\partial x_i \partial x_j}$$

a three-dimensional symmetric ($\mathbf{H}_{i,j} = \mathbf{H}_{j,i}$) square matrix of the partial derivatives of Φ. The movement of the particle in this potential is described by the model of the three-dimensional harmonic oscillator (cf. Section 2.1.2). The motional modes of the oscillator are given by the eigenvectors $\boldsymbol{u}_i$ of the matrix $\mathbf{H}$ and the corresponding eigenvalues λ_i are related to the motional frequencies $\omega_i^2 \propto \lambda_i$. The particle is trapped, if $\boldsymbol{r}_0 = \mathbf{0}$ is a minimum of the potential, which is true if $\forall i : \lambda_i > 0$.

Earnshaw's theorem To trap ions, we make use of their electrical charge. Therefore, the trapping potential should be an electrical potential Φ_{el}. Gauss's law (Maxwell's first equation) states that the electric field

$$\boldsymbol{E} = -\nabla \Phi_{\mathrm{el}}$$

in the charge-free space the divergence vanishes:

$$\nabla \cdot \boldsymbol{E} = 0$$

The divergence can also be calculated from the Hessian matrix by $\nabla \cdot \boldsymbol{E} = \mathrm{Tr}(\mathbf{H})$ with the trace given by the sum of the eigenvalues of $\mathbf{H}$,

$$\mathrm{Tr}(\mathbf{H}) = \sum_{i=0}^{3} \lambda_i.$$

From this it follows that $\sum_{i=0}^{3} \lambda_i = 0$, meaning that at least one eigenvalue is negative or all are zero. As described above, a particle can only be trapped at positions where all eigenvalues are larger than 0. Therefore, a configuration of static electric fields cannot be used to trap a particle in free-space. This is known as Earnshaw's theorem (Earnshaw 1842).

Paul trap In the 1950s Wolfgang Paul developed the Paul trap, a solution towards the problems described above. The general idea is to replace the static potential an oscillating electric potential, rapidly alternating confining and de-confining axes. The motion of a particle in such a time-dependent potential

$$\tilde{\Phi}_{\mathrm{rf}}(t) = \Phi_{\mathrm{rf},0} \cdot \sin(\Omega_{\mathrm{RF}} \cdot t) \tag{2.15}$$

with oscillation frequency Ω_{RF} on the order of $2\pi \times (1\text{–}100)\,\mathrm{MHz}$ (radio frequency) can be described by the Matthieu equations. Characteristic features of the equations of motion are slow oscillations (secular motion) superimposed with fast oscillations with Ω_{RF} of smaller amplitude (micromotion). Neglecting fast oscillations $\propto \Omega_{\mathrm{RF}}$ allows to describe the motion with the harmonic oscillator model. In particular, it allows to define a static, pseudopotential Φ_{RF}:

$$\Phi_{\mathrm{RF}} = \frac{q}{4m{\Omega_{\mathrm{RF}}}^2} \left|\nabla \Phi_{\mathrm{rf},0}\right|^2$$

This pseudopotential is not subject to Gauss's law. It can be confining in all directions. In Figure 2.7 we show a cut-through of a typical design of a Paul trap, consisting of four linear rods. This design allows one to confine a charged particle in the plane orthogonal to the rods. Additional control electrodes at both ends are used to apply a static electric field, confining the particle in axial direction (along to the rods).

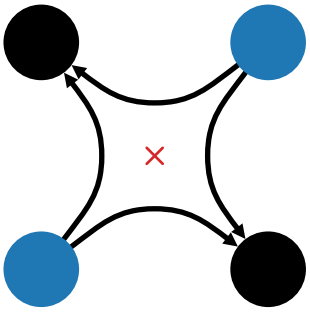

Figure 2.7: Cut through a simple, linear Paul trap. The electrodes are arranged as four rods reaching into the page. The radio-frequency electrodes (blue) in combination with the ground electrodes (black) generate an electric field (black arrows). At the centre a field free point (red cross) allows trapping of charged particles. The ground electrodes could be additionally used as control electrodes.

As stated before, the particle will additionally move with fast oscillations at Ω_{RF}. This intrinsic micromotion is additionally increased if the particle is displaced from

the trap centre, e.g. by an electric field. Here the stronger trapping field will lead to a larger micromotion amplitude called excess micromotion (Berkeland et al. 1998).

Conventional Paul traps suffer from shortcomings that limit their usability for envisioned quantum simulators and quantum computers: They allow to trap a Coulomb crystal of ions along a linear trapping region. This crystal cannot extend into more than one dimension without excess micromotion. In these crystals, typical inter-ion spacings are on the order of (2–10) µm (for $^{25}Mg^{+}$ ions with an axial centre-of-mass frequency of $2\pi\times(0.5\text{–}5)$ MHz) (James 1998). At the same time, typical ion-electrode distances are on the order of a few 100 µm (Schaetz et al. 2007). This limits the ability to control the electric potential individually for single ions in the crystal.

2.3.2 Surface-electrode ion traps

Surface-electrode traps, where the trapping and control electrodes are placed on a single surface, were developed to tackle the shortcomings of conventional Paul traps described above. The concept was inspired by chips used to trap neutral atoms (Dekker et al. 2000; Folman et al. 2000; Müller et al. 1999; Shin et al. 2005).

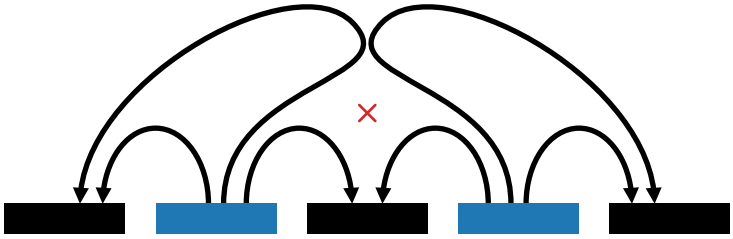

Figure 2.8: Cut through a simple, linear surface-electrode trap. All electrodes are placed in a single plane. The radio-frequency electrodes (blue) in combination with the ground electrodes (black) generate an electric field (black arrows). At the centre, above the electrodes a field free point (red cross) allows trapping of charged particles. The ground electrodes could be additionally used as control electrodes.

As shown in Figure 2.8, the electrode structure is reduced to a single plane to generate a trapping potential above. This two-dimensional trapping structure can be produced using advanced microfabrication techniques as used in producing microchips, and the backside of the chip can be used, e.g. for electrical interconnections.

Linear surface-electrode traps In first trapped-ion applications linear trapping configurations, as in a Paul trap, were realized with two parallel radio-frequency rails generating the trapping potential and additional control electrodes embedded into the surface (Allcock et al. 2012; Brady et al. 2011; Chiaverini et al. 2005; Moehring et al. 2011; Mount et al. 2013; Pearson et al. 2006; Seidelin et al. 2006; Stick et al. 2010, 2006). We use one of these traps, first described by Stick et al. (2010), for some of the experiments and describe the trap in detail in Section 2.3.3.

Surface-electrode trap arrays Early theoretical publications proposed the use of two-dimensional arrays of individually trapped ions as a platform for quantum computing (Cirac and Zoller 2000; DeVoe 1998). The realization of two-dimensional platforms is additionally required for quantum simulations of physical problems of interest that are not accessible by current theoretical methods (Cirac and Zoller 2012).

In the last decade, several ion-trapping groups have worked towards a realization of two-dimensional arrays of individually trapped ions. We summarize some in Table 2.2 where we also layout our trap arrays described in Section 2.3.3. Here it becomes

Group Publications	Array size	Inter-site distance (µm)	Details
R. Blatt - Innsbruck Kumph et al. (2011) Kumph et al. (2016)	4 x 4	1500	Individually adjustable RF amplitudes (one per site), no control electrodes.
J. Chiaverini - MIT Bruzewicz et al. (2016)	2 x 2	500	5 control electrodes per site.
W. Hensinger - Sussex Rattanasonti et al. (2013) Sterling et al. (2014)	29, triangular	270.5	6 control electrodes in total.
J. Home - ETH Zürich Jain et al. (2018)	concept	20	Theoretical proposal of an array of Penning microtraps.
Ours Mielenz et al. (2016) Hakelberg et al. (2019)	3, triangle	80 & 40	10 control electrodes per site for tuning of local electric potential up to 2nd order (fields and curvatures).

Table 2.2: Overview of the experimental research towards two-dimensional ion trap arrays in various groups with relevant publications. We show the number of sites and geometry as well as the inter-site distance.

evident that all other realized approaches have inter-site distances of $r \gg 200\,\mu\text{m}$. This limits the usability as inter-site coupling via the Coulomb interaction of individual ions (described in Section 2.5) scales with r^{-3}, resulting in an approximate requirement of $r < 50\,\mu\text{m}$.

Design

In the following, we describe the procedure used for designing surface-electrode trap geometries for trap arrays. To design trap geometries, one needs the ability to calculate the electric potential of a given geometry. Based on this, optimization criteria can be defined and used to optimize the geometry with respect to these criteria. To calculate the electric potential of a surface-electrode trap we use two methods we describe in the following:

Boundary element method In the Boundary Element Method (BEM, an introduction can be found in Nicolet (1995)), the geometry is reduced to the surfaces of all electrodes. These surfaces are subdivided into a typically triangular mesh. The method then allows one to calculate the surface-charge at each triangle induced by a voltage applied to one of the electrodes. From this charge distribution, the electric potential at an arbitrary point in space can be calculated. The advantages of this method are the possibility to implement arbitrary trapping shapes, for example, to take account of the finite gaps. The disadvantage is the numerical complexity in calculating the charge density. The quality of the calculation increases with a finer mesh size, while the memory scales $\mathcal{O}(n^2)$ with the number of mesh elements n (storing a two-dimensional matrix covering the effect of each mesh element on all other elements), limiting the scalability of the approach. A speed-up and lower memory demand can be achieved by the fast-multipole method, where nearby sources are grouped together when calculating the effect at a larger distance (Engheta et al. 1992; Rokhlin 1985).

Gapless-plane approximation In the gapless-plane approximation, all electrodes are assumed to lie in a single two-dimensional infinite surface. Additionally, there are no gaps between the electrodes, i.e. the complete surface not filled by electrodes is kept at ground potential, essentially forming an additional electrode. It was shown that under these assumptions the electric potential generated by a single electrode of arbitrary shape can be analytically calculated from the outline of the electrodes, similar to the Biot-Savart law for electromagnetism (Oliveira and Miranda 2001; Wesenberg 2008). The disadvantages of this method are that the aforementioned constraints have to be fulfilled, meaning that only two-dimensional traps can be simulated. The constraints of non-existing gaps cannot be realized in real traps, as electrodes would not be isolated from each other. However, the effect is negligible for realistic traps with gap sizes sufficiently small compared to electrode and trapping-site to gap distances (Schmied 2010). The advantage of the method is the analytic description that allows for fast computations of the electric potential. This is especially important when optimising electrode structures where many evaluations of varying electrode geometries are performed.

Based on the gapless-plane approximation a software package was developed by Schmied et al. (2009) to generate optimal electrode geometries for arbitrary finite or infinite lattices of individual (micro-)traps. This software package was used to design our triangle trap array, first published in Mielenz et al. (2016). From a given set of trapping sites, e.g. three sites in an equilateral triangle, the software partitions the surface into two categories, the radio-frequency electrode, and the ground electrode. Note, the attribution is arbitrary and could be reversed, generating the same electric potential assuming there are no additional electrodes. The optimization aims at maximizing a *dimensionless curvature* a value characterizing the *strength* of the individual traps given by the curvature of the trapping field. Constraints to the optimization include that the trapping sites are field-free, and the curvature tensor of the potential

at the trapping sites apart from a variable scaling factor. After assigning the radio-frequency electrode, the residual surface can be further sub-divided into individual control electrodes, which allow to tune the electric potential (see Section 2.4).

2.3.3 Our traps

The experiments presented in this thesis were performed in two different surface-electrode traps: A linear trap with one linear trapping region and a trap array featuring three individual trapping sites arranged in an equilateral triangle. Both traps were produced by Sandia National Laboratories (Albuquerque, NM) using a process described in the supplement to Tabakov et al. (2015).

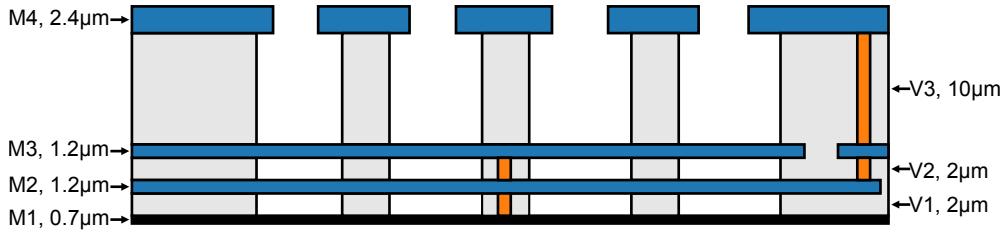

Figure 2.9: Overview over the multilayer architecture. Electrically conducting layers Mi (blue, black for the ground layer) are connected by vias (orange) and separated by isolating layers Vi (grey). This allows the routing of radio-frequency and control voltages to electrodes on the surface of the trap (layer M4). Figure adapted from Maunz and Blain (2013).

The architecture sketched in Figure 2.9, is based on fabrication techniques used in the field of semiconductor/CMOS chips and MEMS[1] processes. The multilayer design allows to route electronic connections to the individual electrodes, while the ion is, except for the gaps, only directly exposed to the top layer. The overhangs of the top layer above the gaps shield the ion from a direct line-of-sight of the isolating SiO_2 (Silicon dioxide) layer. This lowers the influence of charges accumulating on isolators, especially under ultra-high vacuum conditions, e.g. by charging from UV lasers. The trap chips are packaged and bonded onto chip carriers with pins as electrical connections, which allows mounting the package onto a socket in the experimental setup (see Section 3.3.1).

In the following, we will describe the two traps used for the results presented here. The linear trap was used in the new vacuum setup (described in Section 3.3, experiments in Section 3.4) and the triangular array was used in the established vacuum setup for the main results of this thesis in Chapter 4.

The linear trap

The linear trap is used by several groups and described in several publications, e.g. by Allcock et al. (2011), Brady et al. (2011), Mount et al. (2013) and Stick et al. (2010).

[1] MEMS: Micro-electro-mechanical systems

For this trap a simplified architecture was used based on two instead of the four metal layers depicted in Figure 2.9 (Stick et al. 2010).

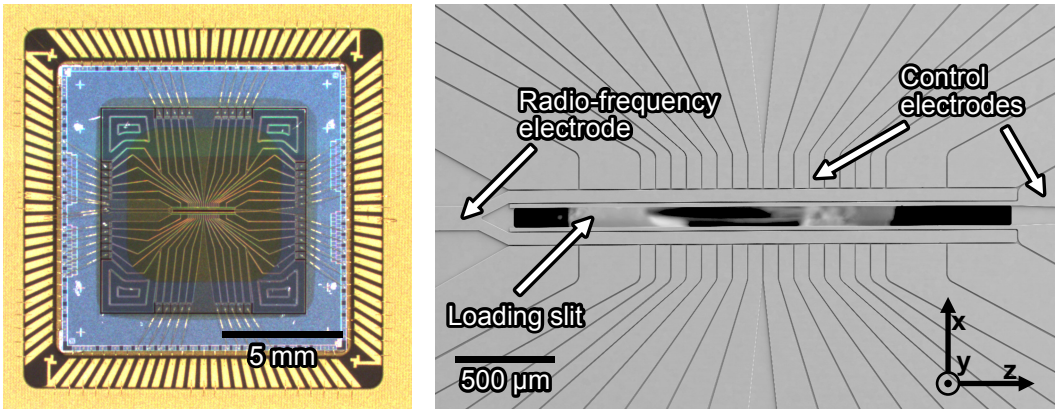

Figure 2.10: Overview of the linear surface-electrode trap. Left: A photo of the packaged trap chip shows the trap in the centre, connected to the chip carrier via wire bonding. Right: A close-up SEM image (right) shows the segmented radio-frequency and control electrodes. The trapping potential is generated by the two central radio-frequency rails. The gaps between the electrodes are approximately 7 µm wide. A central loading slit allows back-side loading of the trap. Pictures courtesy of Sandia National Laboratories (Maunz and Blain 2013).

The trap, pictured in Figure 2.10, features a single radio-frequency electrode split into two rails (each 2.5 mm by 60 µm) in the trapping region. The resulting trapping potential features a linear minimum in the centre of the trap, parallel to the rails and approximately 83 µm above the trap. 42 control electrodes allow to tune the electric potential. The electrodes are separated by 7 µm wide gaps. In our experiments we drive the radio-frequency electrode with $\Omega_{\mathrm{RF}} \approx 2\pi \times 57.3\,\mathrm{MHz}$ and a zero-peak amplitude we estimate to $U_{\mathrm{RF}} \approx 80\,\mathrm{V}$. Our version of the trap additionally features on-chip trench capacitors of 1 nF between each electrode and ground (Maunz and Blain 2016). They are used to filter out pick-up voltage from the radio-frequency electrode, capacitively coupling to the control electrodes. In experiments without on-chip filtering, this pick-up led to additional micromotion that could not be compensated by repositioning the ion (Allcock et al. 2012).

In this trap, in the new vacuum chamber, we observe storage times of single ions of up to 20 h and typically 8 h (while Doppler cooling).

The triangle trap array

The triangle trap array was conceived in collaboration with Roman Schmied and Dietrich Leibfried from the ion storage group (NIST). It was first described in the joint publication Mielenz et al. (2016). A detailed description can be found in Kalis (2017) and Mielenz (2016). The trap chip features two different trap arrays where only one is active at a time. Both traps feature three-trapping sites in an equilateral

triangle approximately 40 µm above the chip. In the first one, used for the results presented in Mielenz et al. (2016), the inter-site distance (side-length of the triangle) is 80 µm, while in the second trap, used here, it is 40 µm. In the first trap, we realized the individual control of the electric potential at the three sites (Mielenz et al. 2016), but the inter-site distance does not permit to demonstrate inter-site coupling (see Section 2.5). We therefore here use the 40 µm array. We will here only describe this second, smaller array, used for the results of this work, and previously in Kalis (2017) and Kalis et al. (2016). In Figure 2.11 we show images of the trap. Two

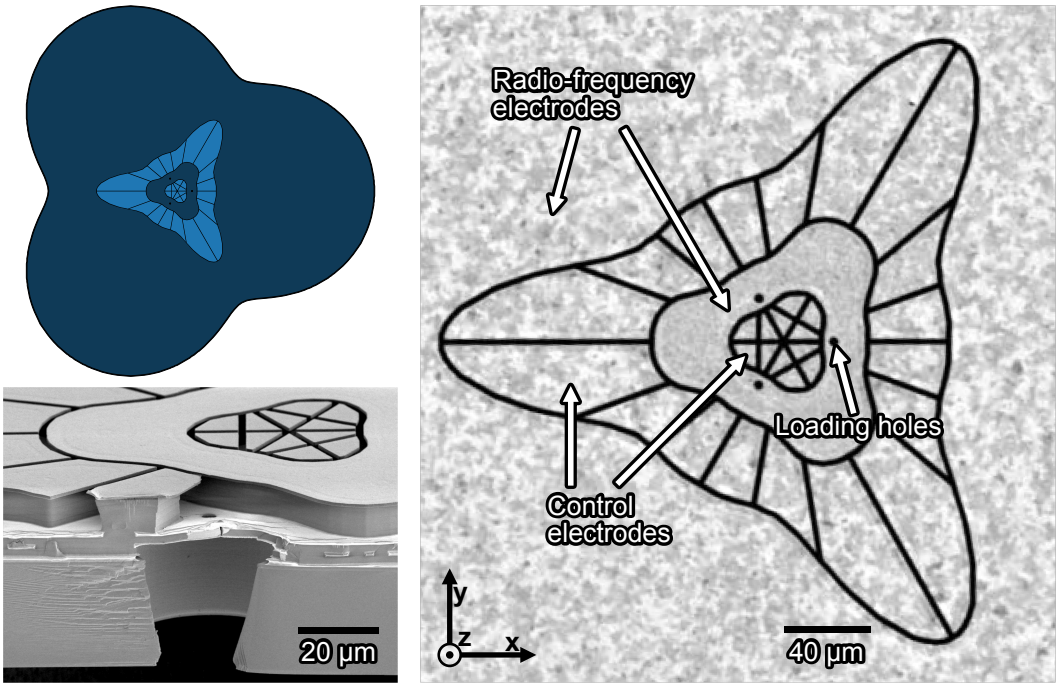

Figure 2.11: Overview of the triangle trap chip. Top left: For given trap positions and motional-mode orientations the optimization algorithm yields two radio-frequency electrodes (dark blue). The remaining inner surface is segmented into single control electrodes (light blue). Right: An SEM image of the final trap chip fabricated by Sandia National Laboratories. The radio-frequency and control electrodes are separated by (1–2) µm wide gaps. Three loading holes below the calculated trapping sites allow back-side loading. Bottom left: An SEM image of a cut-through trap shows overhanging control electrodes to prevent a direct line-of-sight between the ion and the isolating layer below the electrodes. Note, for this revision of the chip the loading holes were placed incorrectly. SEM images courtesy of Sandia National Laboratories (Maunz and Blain 2013).

radio-frequency electrodes, connected on-chip, generate the trapping potential. 30 control electrodes allow individual tuning of the electric potential. Typically, we want to control local electric fields (three degrees-of-freedom, dof) and curvatures (5 dof), demanding 8 dof per trapping site (Section 2.4.3). The overhead of 2 electrodes per site lowers the voltages required for realizing desired control potentials. Electrodes

are separated by (1–2) µm wide gaps. Three holes in the chip below the trapping sites allow loading the trap from atoms passing through the chip. This allows to install an oven evaporating the atoms below the trap that shields the electrode from excess coating by (in our case) magnesium. To filter pick-up of radio-frequency voltages on the control electrodes, each electrode is connected to ground via an 820 pF on-chip capacitor. The top layer is coated with a 50 nm thick gold layer (Maunz and Blain 2013).

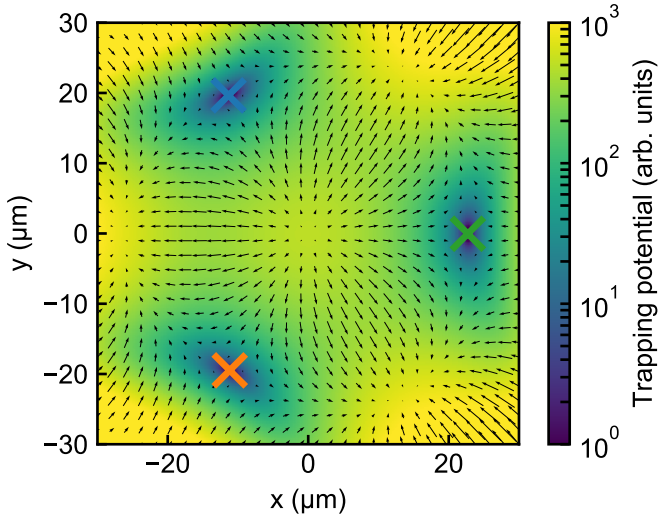

Figure 2.12: Numerically calculated trapping potential generated by the triangle-trap array. We plot the electric field lines generated by the radio-frequency electrodes (black arrows) and the resulting trapping potential in the $\boldsymbol{x}$-$\boldsymbol{y}$-plane at height of the trapping sites. The trapping sites are at minima of the trapping potential forming an equilateral triangle of sites T_0 (blue cross), T_1 (orange cross), and T_2 (green cross).

In Figure 2.12 we plot the calculated trapping potential in the $\boldsymbol{x}$-$\boldsymbol{y}$-plane, parallel to the trap chip at height of the trapping sites ($z \approx 40$ µm). The arrows indicate the electric field generated by the radio-frequency electrode, while the colour depicts the resulting time-averaged pseudopotential (Section 2.3.1). The three crosses mark the three calculated minima, three trapping sites, which we label T_0 (blue), T_1 (orange), and T_2 (green), in counter-clockwise direction.

In this trap, we can load single (or multiple) ions at all three sites. To fill selected sites we reposition the ions using dedicated control potentials. The lifetime of single ions in the trap is in the rage of a few seconds up to 30 min, but typically on the order of 5 min, while continuously Doppler cooling. We see evidence that the lifetime varies for different control potential configurations we are using in our experiments. Here, further investigation might help to increase the lifetime by control potentials and when designing new traps (see next Section).

2.3.4 Considerations for upcoming traps

In this Section we want to summarise a few considerations that could be taken into account when designing new surface-electrode traps, especially two-dimensional arrays.

Design of control electrodes In the current designs, the control electrodes are chosen more or less arbitrarily following symmetrical arguments. In an optimal case, the control potentials generated by the control electrodes would span an orthogonal basis of the relevant parameters of the trapping potential at all trapping sites, typically electric fields and curvatures (cf. Section 2.4.3). However, due to geometrical constraints (all electrodes laying in one plane) this might not be feasible. Partitioning the space of the surface not used for the radio-frequency electrode into *many* small sub-electrodes (much more than required control electrodes), the problem can be reduced to grouping these small sub-electrodes into control electrodes. We propose to classify each sub-electrode by the respective contribution to the electric field (3 degrees of freedom) and curvature (5 degrees of freedom) at each trapping site (N_{sites} sites). Following, each electrode is described by a vector of dimension $(3+5) \times N_{\text{sites}}$. Note, it might be beneficial to normalize these vectors, e.g. by the highest (absolute) entry. It is favourable to group sub-electrodes with similar contributions, such that the contributions of different electrodes (assembled from sub-electrodes) are different. This should allow for lower control voltages to realize the same control potential. To group the sub-electrodes, available clustering algorithms, like k-means clustering (MacKay 2003) can be employed. The resulting electrode configuration can be benchmarked numerically by calculating control voltages for different fixed control potentials and comparing the required voltage amplitudes.

Another point to consider is that there should be no direct line-of-sight between the ion and isolating surfaces. This is considered by the overhanging control electrodes in the traps described above. However, gaps between the electrodes running towards a trapping site (as it is the case for the triangle trap array) result in a line of sight, not covered by overhangs.

Design of radio-frequency electrode In the code used to calculate the geometry of the triangular trap array (Schmied et al. 2009), one has to set the motional-mode orientation and curvature at each trapping site. The algorithm then optimizes the dimensionless curvature under these constraints. When using the trap, however, the control electrodes allow one to control the motional mode orientation, while they cannot increase the dimensionless curvature (as described in Section 2.3.1). It could be advisable, to optimize the constraints in the trap calculation for the highest achievable dimensionless curvature. Finding this optimum could be accelerated by using Gaussian-Process Regression (Rasmussen and Williams 2006)[2].

An additional optimization goal could be the escape barrier from the trapping sites, meaning the closest saddle point via that an ion with sufficient motional energy can

[2]We thank Rodrigo A. Vargas-Hernández for making us aware of this technique in a different context.

escape the trap. To find these saddle points, numerical methods used in chemistry for potential-energy surface calculations, as well as molecular-dynamics simulations of the trap could be used. As these simulations might be time consuming, again, the optimization could be sped up by Gaussian-Process Regression.

Adding an additional trapping site for loading and potentially storing ions could increase the duty-cycle when using larger arrays. We already use repositioning of ions between different sites of the triangular array, this could be studied systematically, and the geometry could be optimized to yield *channels* between the trapping sites.

Additional technologies Future trap chips could additionally incorporate technologies developed or being developed by other groups: Microwave rails embedded in the trap surface allow to implement laser-free spin-motion coupling (Ospelkaus et al. 2011) with individual addressing (Warring et al. 2013b). Waveguides in the chip will allow to focus light directly on the site of the ion without interfering with the other trapping sites (Mehta et al. 2016). This also relaxes the constraint on beam pointing stability as only the coupling into the waveguide has to be stable. For detection superconducting nanowires can be incorporated into the trap to allow for local detection while also collecting a large solid angle increasing the detection efficiency (Slichter et al. 2017).

2.4 Controlling motional degrees of freedom

In our envisioned quantum-simulator architecture the motional degrees of freedom of the individually trapped ions are used to couple the individual ions (Mielenz et al. 2016; Schneider et al. 2012). Furthermore, the individual harmonic oscillators could be used to implement (sub-)systems investigated by quantum simulations. In the following, we will first explain the cooling of motional modes by Doppler cooling. Further cooling to the motional ground-state by Raman side-band cooling could be performed but was not needed for the work presented here. For a more detailed explanation of both Doppler and Raman side-band cooling of magnesium ions, we refer to Friedenauer (2010). We follow with the experimental tools to prepare and detect coherent states of motion (see Section 2.1.2) as used during the coupling experiments in this work. Then we explain the methods used to calculate electric control potentials and the motional-mode analysis methods to analyse the effect of these potentials. Finally, we introduce the concept of coupled-harmonic oscillators in view of single trapped ions in the triangle trap array coupled by the common Coulomb interaction.

2.4.1 Cooling

To store ions in a trap they need to be cooled as external influences, e.g. fluctuating electric fields, will lead to heating and ultimately a kinetic energy above the trap depth. Further cooling to the quantum mechanical ground-state of motion allows one to use the ions as quantum harmonic oscillators and prepare classical or non-classical states of motion. Several cooling techniques have been developed. In our experiment we are using Doppler cooling, optionally followed by Raman side-band cooling to the motional ground state. Extensive literature is available describing these cooling techniques, e.g. in the reviews of Eschner et al. (2003) and Leibfried et al. (2003). Here, we give a brief overview of the basic ideas behind Doppler cooling and refer the reader to the aforementioned literature for a more detailed, quantitative description. We will not describe Raman side-band cooling as we did not use it for the experiments presented in this thesis. For a detailed description of side-band cooling in an experiment similar to ours, we refer to Friedenauer (2010) where also Doppler cooling of magnesium ions is described. Furthermore, side-band cooling in our setup is described in Kalis (2017) and Mielenz (2016).

Doppler cooling

Doppler cooling was first proposed by Wineland and Dehmelt (1975) for a single ion and by Hänsch and Schawlow (1975) for a gas of atoms. It was first realized by Neuhauser et al. (1978) and Wineland et al. (1978) with an elaborate description by Wineland and Itano (1979). A description similar to our experiment is given in Friedenauer (2010). A trapped ion with an internal transition at a wavelength λ_i is irradiated by a laser with a wavelength λ_laser. For a moving ion, the Doppler effect will shift the wavelength of the light in the reference frame of the ion. If the ion is

moving towards the laser, the wavelength is shifted *blue*, to shorter wavelengths and for moving with the laser *red* to longer wavelengths. Each absorption of a photon for the ion moving towards the laser will transfer momentum from the photon, decelerating the ion, while absorption when moving with the laser will accelerate the ion. If the laser is red detuned with response to the ion, i.e. $\lambda_{\text{laser}} > \lambda_{\text{i}}$, the ion at rest will scatter less light. However, if the ion is moving towards the laser, the wavelength in the reference frame of the ion will approach λ_{i}, leading to a larger scattering rate, and for the ion moving away from the laser to a lower scattering rate. On average this will decelerate the ion, i.e. reduce its motional energy and thereby cool the ion. For each absorption, the ion will spontaneously emit a photon a in random direction. This leads to a heating effect, which ultimately limits the cooling to the Doppler limit on the order 600 µK for our experiment (Friedenauer 2010). For typical motional frequencies in our experiments, this corresponds to around (5–10) quanta. For a free ion, three pairs of counter-propagating cooling beams would be needed to cool the ion in all three dimensions. In a trap however one laser is sufficient, as long as the three normal modes of the ion (see Section 2.1.2) have sufficient overlap (are non-orthogonal) to the laser's propagation direction.

2.4.2 Coherent states of motion

This part focuses on the experimental preparation and detection of coherent states of motion. As described in Section 2.1.2 coherent states of motion represent the quantum-mechanical analogue to an excited classic harmonic oscillator. In the following, we describe our experimental methods used to prepare and detect coherent states of variable amplitude. We further introduce experimental sequences to measure the coherence of motional states and discuss the problem of motional heating in (especially) surface-electrode ion traps.

Preparation

A central experimental tool of our experiment is the creation of coherent states of motion $|\alpha\rangle$ on a selected motional mode $\boldsymbol{u}_i$, with corresponding frequency ω_i, while not exciting other motional modes of the same, or other ions. Coherent states of motion can be created by a time-dependent classical driving force (Carruthers 1965). Especially by resonantly driving the oscillator with a force oscillating with ω_i. To realize the needed time-dependent force we make use of the electrical charge q of the ion: For a duration t_{exc}, we apply a time-dependent voltage $U_{\text{exc}}(t) = U_{\text{exc}} \sin(\omega_{\text{exc}} t)$ to a control electrode. At the position of the ion this creates an electric field

$$\boldsymbol{E}_{\text{exc}}(t) = \begin{cases} 0 & t \leq 0 \\ \boldsymbol{E}_{\text{exc}} \sin(\omega_{\text{exc}} t) & 0 < t \leq t_{\text{exc}} \\ 0 & t > t_{\text{exc}} \end{cases} \tag{2.16}$$

and thereby a force acting on the ion

$$\boldsymbol{F}_{\text{exc}}(t) = q \cdot \boldsymbol{E}_{\text{exc}}(t)$$

For the resonance condition $\omega_i = \omega_{\mathrm{exc}}$ this leads to a coherent state with average phonon number

$$\bar{n} = |\alpha|^2 = \underbrace{\langle \boldsymbol{E}_{\mathrm{exc}} \cdot \boldsymbol{u}_i \rangle^2}_{=E_\parallel^2} \frac{t_{\mathrm{exc}}^2 q^2}{8m\hbar\omega_i} \tag{2.17}$$

where $E_\parallel := \langle \boldsymbol{E}_{\mathrm{exc}} \cdot \boldsymbol{u}_i \rangle$ represents the electric field amplitude projected onto the motional mode vector. In Kalis et al. (2016) we used this dependence to retrieve information of the motional mode orientations from multiple excitations with known electric field vectors. Both the excitation duration t_{exc} and amplitude U_{exc} can be controlled in the experiment. This allows us to excite coherent states of selected amplitude. For a non-zero detuning $\Delta\omega = \omega_i - \omega_{\mathrm{exc}}$ the average phonon number scales with

$$\begin{aligned} \bar{n}(\Delta\omega, t_{\mathrm{exc}}) &\propto \frac{\sin^2(\Delta\omega\ t_{\mathrm{exc}}/2)}{(\Delta\omega\ t_{\mathrm{exc}})^2} \\ &\leq \frac{1}{(\Delta\omega\ t_{\mathrm{exc}})^2} \end{aligned} \tag{2.18}$$

as approximated for a detuning small compared to motional frequencies $\Delta\omega \ll \omega_i$. This allows isolation of spectrally separated motional modes by choosing $t_{\mathrm{exc}} \gg (\Delta\omega)^{-1}$. In a typical experiment, we are working with up to three ions distributed over the three trapping sites. To excite along one selected motional mode, we first choose an electrode with a corresponding electric field component strongest along this mode. This allows us to isolate the two other ions. Typically, all other motional modes at all sites are detuned by at least $\Delta\omega/(2\pi) \approx 100\,\mathrm{kHz}$ and we choose $t_{\mathrm{exc}} \geq 25\,\mu\mathrm{s} > 2\pi/\Delta\omega \approx 10\,\mu\mathrm{s}$. In Figure 2.13 we show exemplarily reconstructed average phonon numbers, after excitation of a motional mode at T_0 with frequency $\omega_i/(2\pi) = 3.76\,\mathrm{MHz}$ for $t_{\mathrm{exc}} = 20\,\mu\mathrm{s}$. We excite for variable control voltage amplitude $U_{\mathrm{exc,ctrl}}$, that is, the amplitude of oscillation we set in our control system. The actual amplitude at the electrode is further reduced by filter effects. We fit Equation 2.17 to extract the projected electric field $E_\parallel$ as a function of $U_{\mathrm{exc,ctrl}}$. The fit yields $E_\parallel(U_{\mathrm{exc,ctrl}}) = 22.863(1)\,(\mathrm{V/m})/\mathrm{V} \cdot U_{\mathrm{exc,ctrl}}$. Using this method, we are able to excite arbitrary coherent states from single up to several tens of thousand quanta.

Detection and reconstruction

Our method of reconstructing the amplitude of coherent states in the range of (100–10 000) quanta is based on the method we described in Kalis et al. (2016) (based on DeVoe et al. (1989), explained in more detail in Kalis (2017)), which we will illustrate shortly, followed by changes made during this work to compensate for additional effects. The detection of motional excitation is based on the optical Doppler effect modulating the detection laser in the reference frame of the oscillating ion. In the following, we consider one single $^{24}\mathrm{Mg}^+$ ion moving along one motional mode with corresponding frequency ω_i. A laser beam resonant with the detection transition

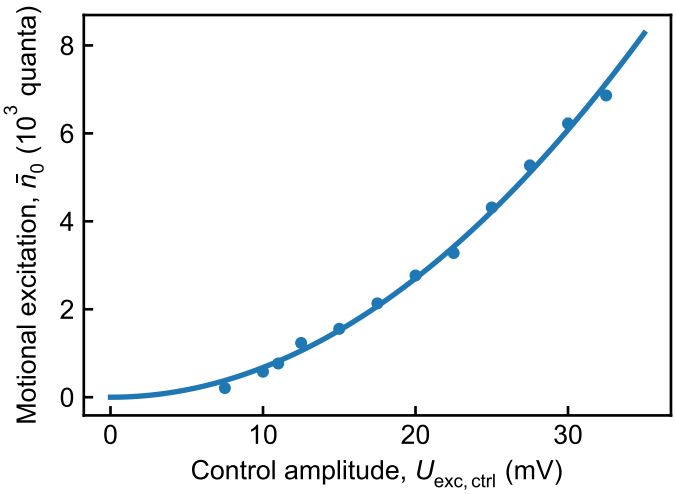

Figure 2.13: Exemplary preparation and reconstruction of coherent states we excite at site T_0 with variable control amplitude $U_{\text{exc,ctrl}}$ for constant duration $t_{\text{exc.}} = 20\,\mu\text{s}$. We fit the detected motional state amplitudes (blue data points) by a squared function $\bar{n}_0 \propto U^2_{\text{exc,ctrl}}$. We extract an effective electrical field amplitude of $22.863(1)\,\text{V/m/V}_{\text{exc,ctrl}}$. Error bars are smaller than the marker size.

frequency $f_{\text{det}} \approx 1072\,\text{THz}$ is shifted in frequency in the reference frame of an ion moving with speed $v_{\parallel}$ parallel to the beam. The relative frequency shift is given by:

$$\Delta f = f_{\text{det}} \frac{v_{\parallel}}{c} \tag{2.19}$$

The ion scatters photons with a rate

$$\mathcal{F}(\Delta_{\text{det}}) = \frac{\Gamma}{2} \cdot \frac{s}{1 + s + \left(\frac{2\Delta_{\text{det}}}{\Gamma}\right)^2} \tag{2.20}$$

where $\Gamma/(2\pi) \approx 41\,\text{MHz}$ is the natural linewidth of the transition, Δ_{det} denotes a detuning between the detection laser and the detection transition and $s = I/I_{\text{sat}}$ is the saturation parameter, given from the laser intensity I divided by the saturation intensity $I_{\text{sat}} = 2550\,\text{W m}^{-2}$ of the transition (Friedenauer 2010). For an ion oscillating with amplitude A_i in a harmonic potential the Doppler effect (Equation 2.19) leads to a modulation of the laser frequency in the reference frame of the ion and thereby a dependence of the scattering rate on the motional oscillation amplitude. This modulation is characterized by a modulation index

$$\beta = |\langle \boldsymbol{u}_i \cdot \boldsymbol{k}_{\text{laser}} \rangle| \, A_i \tag{2.21}$$

with the wave vector of the detection laser $\boldsymbol{k}_{\text{laser}}$. Here, as for the excitation above, another dependence on $\boldsymbol{u}_i$ allows us to infer information about the motional mode

orientation, we used in Kalis et al. (2016). Taking only this into account the scattering rate can be calculated by (Kalis et al. 2016):

$$\mathcal{F}_{\omega_i}(\Delta_{\mathrm{det}}, \beta) = \sum_{n=-\infty}^{\infty} \frac{J_n^2(\beta)\ (\Gamma/2)^2}{(\Delta_{\mathrm{det}} + n\omega_i)^2 + (\Gamma/2)^2} \tag{2.22}$$

where J_n are the n-th Bessel function of the first kind. This can be interpreted as a sideband spectrum with resonances spaced by ω_i and relative amplitudes scaling with the Bessel functions. Due to the transition linewidth $\Gamma \gg \omega_i$ the spectrum is not resolved and the fluorescence decreases as a monotonic function of β. In the experiment we perform calibration measurements, detecting a Doppler cooled ion to infer the maximal fluorescence rate and detecting when the ion is removed from the trap to measure a background signal from laser light scattered on the trap surface. This allows us to correct and normalize fluorescence data before calculating motional excitation amplitudes.

During this thesis, for measurements in the triangle trap array, it became evident that for our motional amplitudes on the order of (100–1000) nm, additional site-specific effects have to be taken into account. While we do compensate for excess micromotion (see Section 2.3.1) at all sites, theses oscillation amplitudes lead to significant micromotion contributions along the trajectory of the ions. In general, micromotion leads to a modulation of the detection transition, comparable to the effect due to the secular motion with ω_i described above. For an ion at rest, this leads to a fluorescence spectrum given by:

$$\mathcal{F}_{\mathrm{MM.}}(\Delta_{\mathrm{det}}, \beta_{\mathrm{MM}}) = \sum_{n=-\infty}^{\infty} J_n^2(\beta_{\mathrm{MM}})\, \mathcal{F}(\Delta_{\mathrm{det}} - n\,\Omega_{\mathrm{RF}}) \tag{2.23}$$

Here the modulation index β_{MM} is given by the ions micromotion due to the radio-frequency field oscillating at Ω_{RF}. In Figure 2.14 we plot Equation 2.23 for several values of β_{MM} and $\Omega_{\mathrm{RF}}/(2\pi) = 89\,\mathrm{MHz}$ as used in the triangle trap setup. For a resonant detection laser ($\Delta_{\mathrm{det}} = 0$) in this range, the fluorescence decreases for larger micromotion contributions.

In Figure 2.15 we plot numeric calculations of the radio-frequency field in the triangle trap at the trapping sites in the $\boldsymbol{x}$-$\boldsymbol{y}$-plane. We additionally show the micromotion modulation index (normalized to the highest value) with respect to our detection laser propagating in $\sqrt{1/2}(\boldsymbol{x} + \boldsymbol{y})$ direction. Here we see that, for example, comparing sites T_0 (blue) and T_1 (orange) a displacement of an ion along $\boldsymbol{y}$ at T_1 leads to a larger modulation index than at T_0. Here the detection laser breaks the symmetry of the two sites that apart from this are mirrored along the x-axis. This leads to a further decreased fluorescence from a motionally excited ion at T_1, which in turn results in a systematic overestimation of the reconstructed motional amplitude when using Equation 2.22.

To take these effects into account we perform additional calibration measurements for each site: Using electric control potentials, we displace a single ion along $\boldsymbol{u}_i$ tracking the fluorescence. This allows us to calculate the position-dependent modulation index

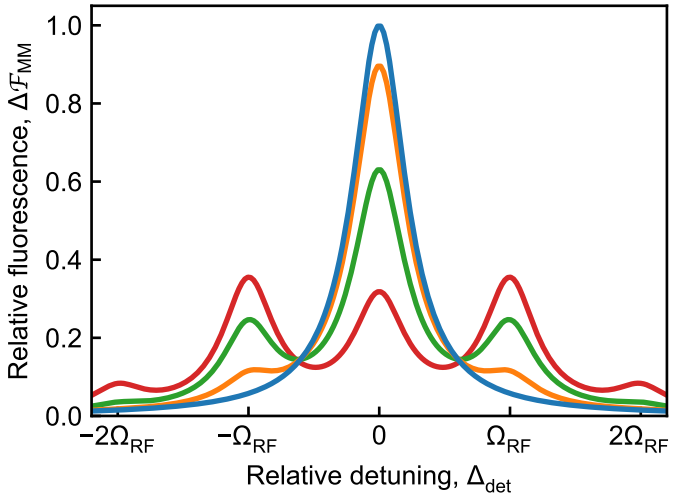

Figure 2.14: Calculated fluorescence spectrum for variable amplitudes of micromotion with corresponding modulation indices $\beta_{\mathrm{MM}} \in \{0, 0.5, 1.0, 1.5\}$ (blue, orange, green, red). The width of the resonances is given by the linewidth of the transition, in our case $\Gamma/(2\pi) \approx 42\,\mathrm{MHz}$ and the individual resonances are separated by the radio-frequency driving frequency of, in the triangle trap array, $\Omega_{\mathrm{RF}}/(2\pi) \approx 89\,\mathrm{MHz}$. We normalize the spectrum to the highest value, on resonance for $\beta_{\mathrm{MM}} = 0$.

$\beta_{\mathrm{MM}}(\Delta x')$ (here $\Delta x'$ refers to the displacement along $\boldsymbol{u}_i$) index. We additionally track the motional frequency $\omega_i(\Delta x')$, which due to higher-order contributions to the trapping potential is not constant along $\boldsymbol{u}_i$ (see also Section 2.4.4). Using the results from these calibration measurements we numerically calculate the fluorescence of an ion at a specific site as a function of the excitation amplitude: For a fixed initial excitation $\bar{n}$ we numerically calculate the trajectory of the ion along the trapping potential using the Leapfrog integration scheme (Hut and Makino 2007) on time steps of typically $10^{-11}\,\mathrm{s}$, small compared to inverse motional frequencies on the order of $2\pi\times(2\text{–}10)\,\mathrm{MHz}$. For each time step t, from the position $\Delta x'_t$, we calculate a micromotion modulation index $\beta_{\mathrm{MM,t}}$ from interpolated measurements and, from the speed of the ion v_t, calculate the detuning $\Delta_{\mathrm{det,t}}$ of the detection laser in the reference frame of the ion. Using equation Equation 2.23 we can then calculate the scattering rate at this time step. Integrating the scattering rate for many oscillations (choosing an integration time large with respect to the inverse motional frequency) leads to an excitation dependent scattering rate as a function of the initial excitation $\mathcal{F}_{\mathrm{num}}(\bar{n})$. We normalize this function by $\mathcal{F}_{\mathrm{num}}(0)$ and use the numerical inverse to reconstruct excitation amplitudes from measured fluorescence values $\bar{n}_{\mathrm{num}}(\mathcal{F}_{\mathrm{measured}}) = \mathcal{F}^{-1}_{\mathrm{num}}(\bar{n})$.

In Figure 2.16 we show exemplarily the difference between this adapted reconstruction method and Equation 2.23 for calibration data taken at T_1. Here, for example, for a motional state of 1000 quanta, corresponding to a relative fluorescence of around 0.5,

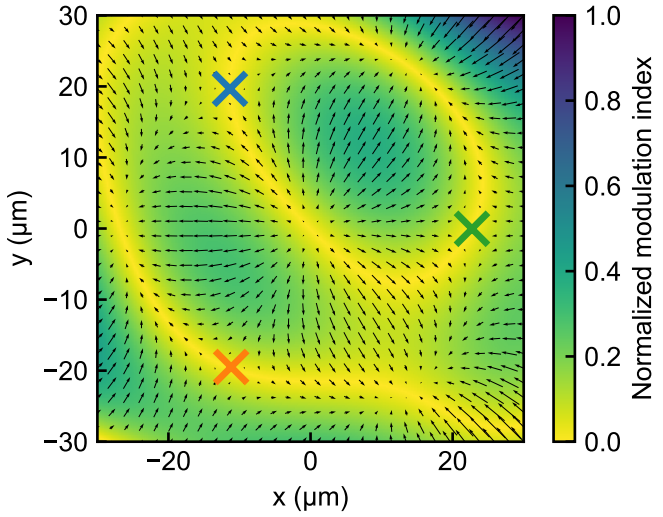

Figure 2.15: Electric field (black arrows) generated by the radio-frequency electrode of the triangle trap array in the $\boldsymbol{x}$-$\boldsymbol{y}$-plane at height of the trapping sites T_0, T_1, and T_2 (blue, orange, and green cross). The field projected onto the detection laser direction (along $\sqrt{1/2}(\boldsymbol{x}+\boldsymbol{y})$) yields the micromotion modulation index which we normalize to the highest value (colours). Due to the detection laser orientation the symmetry of the triangle is broken and different modulation indices are found for displacements along the same direction at different trapping sites.

Equation 2.23 would yield a systematically increased result of 2500 quanta. This confirms the importance of the additional calibration measurements taking into account the micromotion and anharmonic contributions to the trapping potential.

An additional effect we became aware of during this thesis is a systematic error in the reconstructed motional state for a detuning of the detection beam with respect to the detection transition. In previous experiments, the laser was *red* detuned by $2\pi \times 5\,\mathrm{MHz}$ to avoid motional heating by the laser. However, we see that this leads to a cooling of motionally excited ions during the detection interval, which leads to a systematically lower reconstructed motional state. To prevent this effect, we perform a dedicated calibration experiment: We prepare a coherent state of motion, turn on the detection laser for a variable duration t_{laser} followed by detection using the same laser. We perform this for variable frequency of the laser and variable motional-state amplitudes. In Figure 2.17 we plot the resulting data exemplarily for a single ion at T_0. We show the observed fluorescence, which can be used to calculate the motional state. Lower fluorescence values indicate a large motional amplitude. We find a frequency of the laser where both motional states are not affected by the detection laser while a change of $\pm 2\pi \times 1\,\mathrm{MHz}$ leads to measurable heating/cooling of the ion.

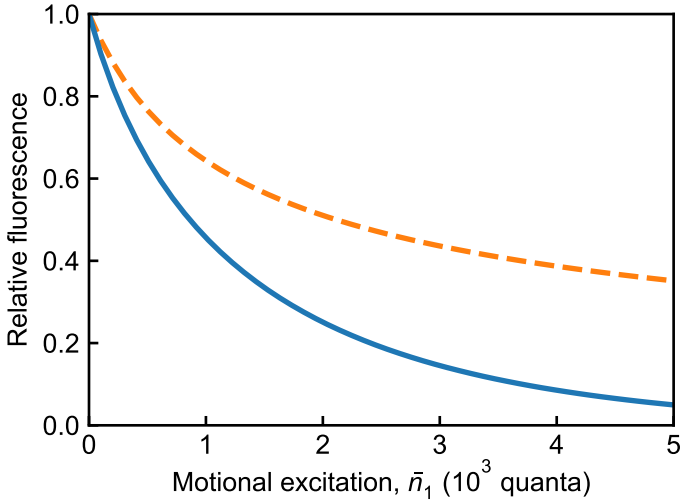

Figure 2.16: Exemplary calculated dependence of the relative fluorescence on the motional excitation at T_1 (motional frequency of $2\pi\times3.59\,\mathrm{MHz}$) using Equation 2.23 (orange dashed line) and our adapted method (blue line) taking into account additional calibration measurements. Here, the significant influenece of these calibrations can be seen. We use the adapted calculation to reconstruct motional state amplitudes from fluorescence measurements in the experiment.

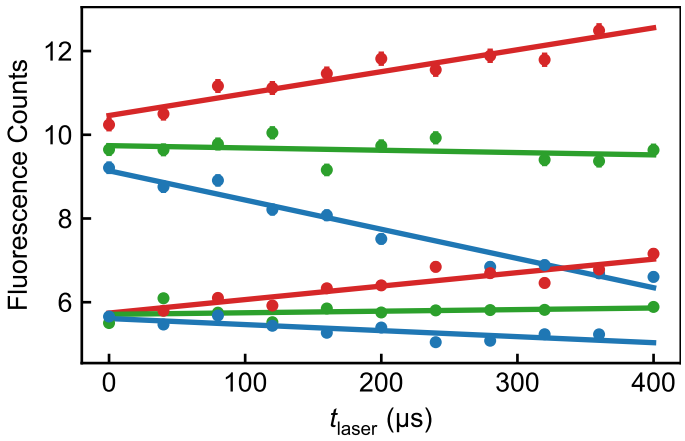

Figure 2.17: Exemplary data to set the frequency of the detection laser. We prepare two motional states with fluorescence counts around 10 and 5.5. For both states we turn on the detection laser for variable duration t_{laser} followed by detection. For an optimized frequency of the detection laser (green data points) the fluorescence and thereby the reconstructed motional amplitude are constant as indicated by linear guides to the eye (green lines). Detuning the laser by $+2\pi\times1\,\mathrm{MHz}$ (blue data points) or $-2\pi\times1\,\mathrm{MHz}$ (red data points) significantly alters the fluorescence. Error bars (SEM) are partially smaller than the marker size.

Motional coherence measurements

For envisioned experiments based on the motional degrees of freedoms, e.g. the coupling between sites in the triangle trap array the phase coherence is an essential parameter. Fluctuations in, for example, the trapping potential amplitude lead to a random evolution of the phase of motional states. To characterize the timescale of this decoherence, we perform a designated calibration experiment described in Schnell (2018) and similarly (using radiation pressure instead of electric fields for excitation) in Talukdar et al. (2016). The protocol, similar to a Ramsey experiment (see Section 2.2.4 and detailed experiments in Section 3.4.2), consists of two motional excitation pulses with a variable phase-difference separated by a waiting duration. The phase difference leads to an additional excitation (in-phase) or de-excitation (out-of-phase) that is limited by variations of the phase of the ion's oscillation between experimental realizations. In Figure 2.18 we show exemplarily two measurements for

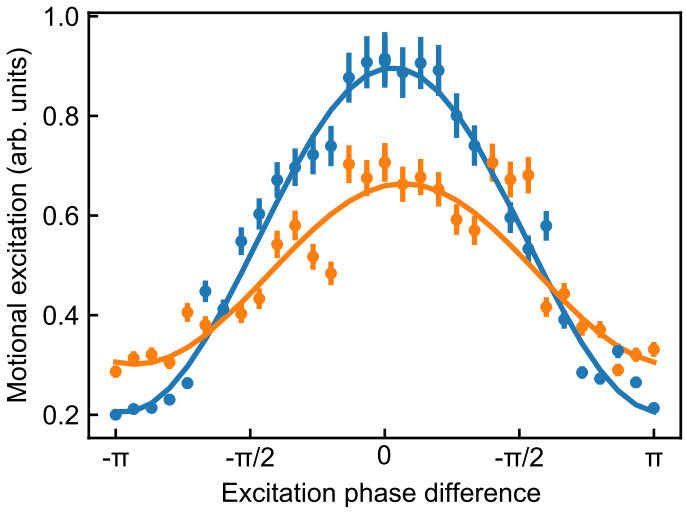

Figure 2.18: Exemplary motional coherence measurement consisting of two motional excitation pulses of variable phase difference and fixed waiting duration between the pulses. We show the reconstructed motional excitation for two waiting durations of 10 µs (blue data points) and 100 µs (orange data points) and fit the data using a sine function (lines). In-phase excitation increases and out-of phase excitation decreases the final motional excitation. The contrast (amplitude of the sine function) as a function of the waiting duration allows to extract a coherence time scale.

a waiting duration of 10 µs and 100 µs in the triangle trap array. From the difference in excitation between maximal excitation and de-excitation, we extract a contrast as a measure for the motional coherence between the two pulses.

In the triangle trap array, we measure typical coherence times in the range of (60–600) µs. We see a strong dependence on the control potential configuration leading to changes by up to one order of magnitude. We attribute this partly to fluctuations of the

radio-frequency amplitude generating the trapping potential. These fluctuations could impact individual motional modes differently based on the individual combination of static and trapping potential along the motional mode vector.

In the future, an active stabilization of the radio-frequency amplitude measured close to the trapping electrodes, as described by Johnson et al. (2016), could help to improve these coherence times.

Additionally, for large coherent states, the finite width of the motional-amplitude distribution might lead to dephasing in the anharmonic trap potential. This will become negligible when working with motional-excitations on the order of single quanta.

Motional heating

In surface-electrode traps, a motional heating coined anomalous heating was observed, which seems to be increased by the small ion-electrode distances in such traps (Hite et al. 2013). Experimentally a scaling with the distance to the closest surface d and motional mode frequency ω has been found

$$\dot{\bar{n}} \propto d^{-\alpha}\omega^{-\beta} \tag{2.24}$$

with exponents $\alpha \approx 4$ and $\beta \approx 2$ measured, for example, in Allcock et al. (2012), Daniilidis et al. (2014), Hite et al. (2012) and Sedlacek et al. (2018). Currently, this is explained by surface-effects for instance from carbon contaminations on the trap chip surfaces. These heating rates, in our case on the order of several motional quanta per ms, limit the timescale of experiments performed near the motional ground state. Several methods have been employed to reduce heating rates: One established method to reduce the heating rates is cooling the trap chip to cryogenic temperatures (Labaziewicz et al. 2008). This imposes rigorous constraints on the vacuum setup, materials used, etc., while the cryogenic setup has the additional advantage of reducing the vacuum pressure by cryo-pumping, i.e. condensation of residual gasses on cold surfaces. Another method is in-situ sputtering of the surface with argon ions as done in Hite et al. (2012). Here the idea is to clean the surface under vacuum conditions, in-situ, i.e. without the need to break the vacuum again. In the new vacuum setup designed and built during this thesis, we implement the possibility for in-situ argon ion sputtering (see Section 3.3).

2.4.3 Control potential calculation and optimization

The control of motional mode orientations and motional frequencies is essential for the operation of a quantum simulator based on the approach of individually trapped ions. It allows, e.g. to orient motional modes for preparation, allows to switch the coupling between sites and tune the coupling strength. In the traps presented in this work and most radio-frequency (ion) traps, in general, the trapping potential Φ is composed of three electric potentials:

$$\Phi = \Phi_{\mathrm{RF}} + \Phi_{\mathrm{ctrl}} + \Phi_{\mathrm{stray}}$$

the time-averaged radio-frequency pseudopotential Φ_{RF} (see Section 2.3.1), a quasi-static control potential Φ_{ctrl}, and an additional electric potential combining the effects of electric charges present around the trapping region, for instance on the electrode surface. In almost all experiments presented in this work, we assume Φ_{RF} as constant. This potential provides the divergence needed for trapping, which is forbidden by Earnshaw's theorem for static electric potentials, cf. Section 2.3.1. It is generated by an oscillating voltage applied to the radio-frequency electrodes of the trap.

The control potential Φ_{ctrl} is used experimentally to shape the total trapping potential Φ. Primarily it is used for two tasks: Firstly, to compensate for electric fields generated by Φ_{stray}. These displace the trapped ions from the minima of Φ_{RF}, which in return leads to excess micromotion. And secondly, to tune the curvature tensor of the trapping potential.

We consider here a single ion with resting position $\boldsymbol{r}$ trapped in the potential $\Phi(\boldsymbol{r})$. From this it follows that $\nabla\Phi(\boldsymbol{r}) = 0$, the electric field vanishes at $\boldsymbol{r}$, and the potential is, in harmonic approximation, fully characterized by the Hessian matrix $\mathbf{H}$. The three orthogonal eigenvectors $\boldsymbol{v}_i$ of $\mathbf{H}$ define the motional mode orientations, while the corresponding eigenvalues λ_i are proportional to the squared motional frequencies $\omega_i^2 \propto \lambda_i$. The application of an additional control potential Φ_{ctrl} leads to a new combined potential

$$\Phi_{\mathrm{new}} = \Phi + \Phi_{\mathrm{ctrl}}$$

and new curvature matrix $\mathbf{H}_{\mathrm{new}}$. In our setup Φ_{ctrl} is generated from static electric fields therefore from Maxwell's first equation it follows that $\mathrm{Tr}(\mathbf{H}_{\mathrm{ctrl}}) = 0$. In combination with the symmetry $\mathbf{H}_{i,j} = \mathbf{H}_{j,i}$, this reduces the number of free parameters in $\mathbf{H}$ to two diagonal and three off-diagonal elements, e.g. $\mathbf{H}_{x,x}$, $\mathbf{H}_{x,y}$, $\mathbf{H}_{x,z}$, $\mathbf{H}_{y,y}$, and $\mathbf{H}_{yz}$. The superposition principle allows to separate $\mathbf{H}_{\mathrm{new}}$ into $\mathbf{H}$ and the control contribution $\mathbf{H}_{\mathrm{ctrl}}$:

$$\mathbf{H}_{\mathrm{new}} = \mathbf{H} + \mathbf{H}_{\mathrm{ctrl}}$$

For the control potentials we follow a basic-function approach described by Hucul et al. (2008): The experimental access to the control potential is given by a set of voltages $\boldsymbol{U}_i$ applied to the control electrodes. The electric potential generated at position $\boldsymbol{r}$ by an electrode i biased at voltage $\boldsymbol{U}_i$ is given by:

$$\Phi_i(\boldsymbol{r}) = \boldsymbol{U}_i \cdot \bar{\Phi}_i(\boldsymbol{r})$$

where $\bar{\Phi}_i(\boldsymbol{r})$ is the dimensionless potential generated by the electrode biased at 1 V. The total control potential is given by summation over all electrodes:

$$\Phi_{\mathrm{ctrl}} = \sum_{i \in \mathrm{El.}} U_i \cdot \bar{\Phi}_i \tag{2.25}$$

In typical experimental application, we are interested in finding a set of voltages $\boldsymbol{U}$ to generate a desired control potential Φ_{ctrl}. Given the dimensionless potentials $\bar{\Phi}_i$, this problem can be solved by linear programming. We use two methods to calculate these $\bar{\Phi}_i$:

The first method is using the gapless-plane approximation. As explained in Section 2.3.2, the advantages of this method are that the calculations are fast, and higher-order derivatives (electric fields, curvatures, etc.) can be calculated directly. The main disadvantage is the limitation to the simplified picture of a gapless, conducting, plane, i.e. the three-dimensional structure of the trap are neglected.

The second method applied is the boundary-element-method. Here the trap is modelled in three dimensions and, for one electrode biased at 1 V, an algorithm calculates charge densities across a finite mesh on the trap surfaces. From this charge density, one can then calculate the electric potential at a given position. We typically evaluate the potential on a finite grid covering the trapping region and store this file, for each electrode, to avoid re-calculation. Derivatives of the potential could also be calculated from the surface charge but we calculate them by finite differences, using the evaluated potential. Here the spacing of the grid we evaluate the potential on limits the accuracy of (higher-order) derivatives calculated from finite differences. For the results in this thesis calculations based on the boundary-elements-method were used. We collaborated with Peter Maunz from Sandia National Laboratories (Albuquerque, NM) who kindly provided us with the potential files.

In the following, we elaborate the calculation of the voltages needed to create desired control potentials, exemplarily for the triangle trap array with three trapping sites and 30 control electrodes. When running the experiments, it is unpractical to always calculate one global control potential satisfying all requirements. The superposition principle allows us to apply a set of control potentials calculated for specific effects independently, for instance, to tune $\mathbf{H}$ at specific sites of the triangle trap array. Following this, we realise sets of control potentials that allow us to tune the field (3 degrees of freedom) and curvatures (5 degrees of freedom) at all three sites independently. This means that we, for example, seek a potential $\Phi_{\mathrm{ctrl,Ex0}}$ that generates an electric field at site T_0 not generating additional fields or curvatures at all three sites:

$$\nabla\Phi_{\mathrm{Ex0}}(\mathrm{T}_0) = \begin{pmatrix} 1000 \\ 0 \\ 0 \end{pmatrix} \mathrm{V\,m^{-1}} \tag{2.26}$$

$$\nabla\Phi_{\mathrm{Ex0}}(\mathrm{T}_i) = \begin{pmatrix} 0 \\ 0 \\ 0 \end{pmatrix} \mathrm{V\,m^{-1}}, \qquad \forall i \in \{1,2\} \tag{2.27}$$

$$\mathbf{H}_{\Phi_{\mathrm{Ex0}}}(\mathrm{T}_i) = \begin{pmatrix} 0 & 0 & 0 \\ 0 & 0 & 0 \\ 0 & 0 & 0 \end{pmatrix} \mathrm{V\,m^{-2}}, \qquad \forall i \in \{0,1,2\} \tag{2.28}$$

Using Equation 2.25, this results in a set of $(3+5)\times 3 = 24$ linear constraints on the voltages U_i:

$$\begin{aligned}
&\sum_{i\in\mathrm{El.}} U_i \cdot \left(\nabla\bar{\Phi}_i(\mathrm{T}_0)\right)_x && = 1000\,\mathrm{V\,m^{-1}} && && \\
&\sum_{i\in\mathrm{El.}} U_i \cdot \left(\nabla\bar{\Phi}_i(\mathrm{T}_0)\right)_j && = 0\,\mathrm{V\,m^{-1}} && && \forall j \in \{y,z\} \\
&\sum_{i\in\mathrm{El.}} U_i \cdot \left(\nabla\bar{\Phi}_i(\mathrm{T}_k)\right)_j && = 0\,\mathrm{V\,m^{-1}} && \forall k \in \{1,2\}\,, && \forall j \in \{x,y,z\} \\
&\sum_{i\in\mathrm{El.}} U_i \cdot \left(\mathbf{H}_{\bar{\Phi}_i(\mathrm{T}_k)}\right)_j && = 0\,\mathrm{V\,m^{-2}} && \forall k \in \{0,1,2\}\,, && \forall j \in \{(x,x),(y,y),\\
& && && && \quad (x,y),(x,z),(y,z)\}
\end{aligned}$$

As we have 30 control electrodes and 24 constraints the set of constraints forms an underdetermined system with infinitely many solutions (assuming that the contributions of the control electrodes are linearly independent). We use this to implement an optimization goal, for instance, to minimize the square norm of the voltages:

$$\min_{U_i}\left(\sum_{i\in\mathrm{El.}} U_i^2\right)$$

or the maximum norm:

$$\min_{U_i}\left(\max_i |U_i|\right)$$

By this, we take into account that in the experiment there will always be a limit on the voltages that can be applied. We solve this constrained optimization problem either by the *cvxpy* Python software package (Agrawal et al. 2018; Diamond and Boyd 2016) or the *CVX* Matlab package (Grant and Boyd 2008, 2014).

In the experiment we sum several of these control potentials $\Phi_{\mathrm{ctrl,k}}$ with variable scaling factors κ_k to a combined control potential $\Phi_{\mathrm{ctrl,profile}}$ that we refer to as a control profile:

$$\Phi_{\mathrm{ctrl,profile}} = \sum_{k\in\mathrm{El.}} \kappa_k \cdot \Phi_{\mathrm{ctrl,k}} \tag{2.29}$$

Each control profile is used to realize a certain configuration of the trapping potential at all three sites, for example, a motional mode orientation for Doppler cooling, or to match the mode-orientation and frequencies for coupling two sites. This allows us to transition between several profiles by ramping, e.g. linearly, between the corresponding control voltages. Note, while the voltage amplitudes are optimized for the individual $\Phi_{\mathrm{ctrl,k}}$, a set of smaller voltages might be available to realize a combined potential $\Phi_{\mathrm{ctrl,profile}}$. We used this to optimize certain profiles where voltages exceeded our technical specifications, but in future experiments the optimization algorithm could be implemented directly into the control system, always optimizing U_i for the desired control profile.

2.4.4 Motional mode analysis

In this Section, we describe our methods used to analyse motional mode configurations, i.e. motional mode frequencies and orientations, at dedicated trapping sites. We focus here on the methods used in the triangle trap array, which are also applicable to ion traps in general. In Kalis et al. (2016) and Mielenz et al. (2016) we already published methods partly used in the following.

Frequencies

To measure motional frequencies, we apply the scheme of resonant excitation described in Section 2.4.2. We trap a single ion and, after Doppler cooling, apply an oscillating

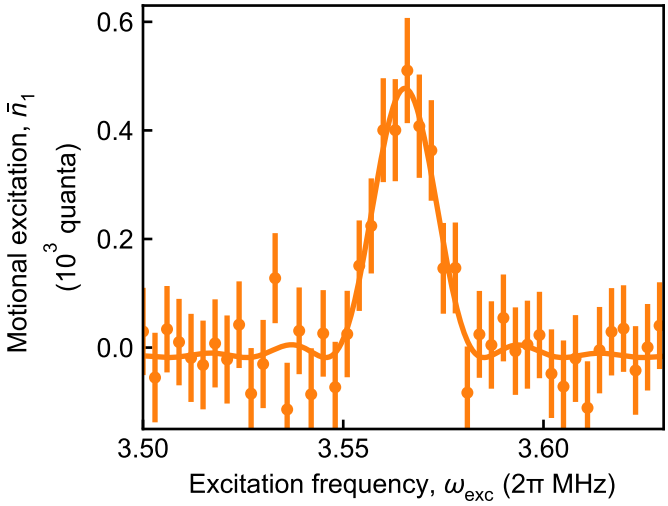

Figure 2.19: Exemplary motional excitation experiment of a single ion trapped at T_1. We excite the ion for 50 µs with constant amplitude and variable frequency ω_{exc} and reconstruct the resulting motional excitation (orange data points). A model fit (orange line) yields a resonance at $2\pi\times3.5654(8)$ MHz with an excitation amplitude of 500(54) quanta and a resonance width corresponding to an excitation duration of 51(5) µs. The unphysical negative excitation amplitudes are a result of the uncertainty of average fluorescence rates and subtracted background fluorescence. Error bars indicate the SEM.

voltage with frequency ω_{exc} to a designated electrode, followed by motional state detection. If ω_{exc} becomes resonant with a motional frequency ω_i the motion of the ion is excited. This allows us to resolve all three motional modes as long as there is sufficient overlap between the detection laser and the corresponding motional mode. If this is not the case we can make use of a dedicated control profile to which we adiabatically (timescales long compared to inverse motional frequencies) switch for Doppler cooling and detection. In Figure 2.19 we show an exemplary measurement of

the lowest frequency motional mode of a single ion trapped at T_1. We excite the ion for 50 µs and a fit of Equation 2.18 yields a centre frequency of $2\pi \times 3.5654(8)$ MHz.

Mode orientation - Analysis on camera

We explored several methods to measure the orientation of motional modes, e.g. based on motional-sensitive two-photon Raman transitions, or the excitation and detection of coherent states of motion (both published in Kalis et al. (2016)). For the coupling experiments presented here, we are mainly interested in the orientation of the lowest-frequency mode $\boldsymbol{u}_{\mathrm{lf}}$ with frequency ω_{lf}, as the coupling rate scales with the inverse mode frequency. We, therefore, focus on the orientation of this mode and use a method based on imaging with the camera: If we load two ions at a single site they form a Coulomb crystal. The axis of the two ions is oriented along the axis of weakest confinement of the local potential, which, ignoring higher-order contributions to the trapping potential, is also the direction of the lowest-frequency mode of a single ion. We use this to measure rotations in the $\boldsymbol{x}$-$\boldsymbol{y}$-plane with an in-plane angle α_{ip} with respect to the $\boldsymbol{x}$-axis (Mielenz et al. 2016). An advantage of this method is that no lengthy measurements and analysis have to be performed as the orientation is directly accessible as a live feed from the camera. This allows for fast manual tuning of relevant control potentials with direct feedback of, e.g. additional displacements caused by electric fields due to imperfections in the control potential calculations. For the coupling experiments we are additionally interested in the out-of-plane orientation of the motional mode, i.e. whether the mode is oriented parallel to the chip/camera plane, or tilted out of this plane. To derive information about this orientation we can again use the camera image. The distance between the two ions is given by the curvature of the trapping potential along this axis. This curvature is proportional to the (squared) motional frequency along this axis, more precisely the lowest centre-of-mass frequency of the two ions, which is, in a harmonic potential, the same as for a single ion. The ion-ion spacing d_{ii} is given by (James 1998):

$$d_{\mathrm{ii}} = \sqrt[3]{\frac{2q^2}{4\pi\epsilon_0 m\omega_{\mathrm{lf}}^2}} \tag{2.30}$$

Using an experiment as described above we can measure ω_{lf} for the two ions. From this, we calculate d_{ii}, which we compare to the ion-ion spacing projected into the $\boldsymbol{x}$-$\boldsymbol{y}$-plane d'_{ii} measured by the camera. The out-of-plane angle α_{oop} between $\boldsymbol{u}_{\mathrm{lf}}$ and the $\boldsymbol{x}$-$\boldsymbol{y}$-plane is then given by:

$$d_{\mathrm{ii}} = \frac{d'_{\mathrm{ii}}}{\cos\alpha_{\mathrm{oop}}} \tag{2.31}$$

For the actual reconstruction of the angles, we additionally take into account the anharmonic contributions to the trapping potential described below by calculating the distance of two ions numerically from the measured trapping potential. We estimate systematic uncertainties of this method on the order of 15°. This method to measure

the out-of-plane angle is limited in the sense that we cannot extract the sign of the angle. For the motional state reconstruction, this is not relevant as only the relative angle with respect to the detection laser is needed. One possibility to extract this angle apart from more involved methods (Kalis et al. 2016) with uncertainties on the order of 4°, is to observe two ions and vary the focal plane of the detection optics and by this extract relative z-positions of the two ions as described for a single ion in Kalis (2017). This information (which ion is *above* the other) then allows to determine the sign of the rotation.

Anharmonicities

For the coupling experiments presented in this work, oscillation amplitudes of the ions reach up to approximately 1 µm. Due to the small scale of the triangle trap array, i.e. the size of the electrodes, the ion-electrode distance, and the inter-site distance, the trapping potential features higher-order contributions relevant for these oscillation amplitudes. This means that the trapping potential is no longer described by a harmonic oscillator. To analyse these anharmonic contributions we displace a single ion along the lowest-frequency mode $\boldsymbol{u}_{\mathrm{lf}}$, tracking the position on the camera. For each position, we locally probe the potential by a coherent excitation experiment as described above. There we use small oscillation amplitudes on the order of 300 nm. In

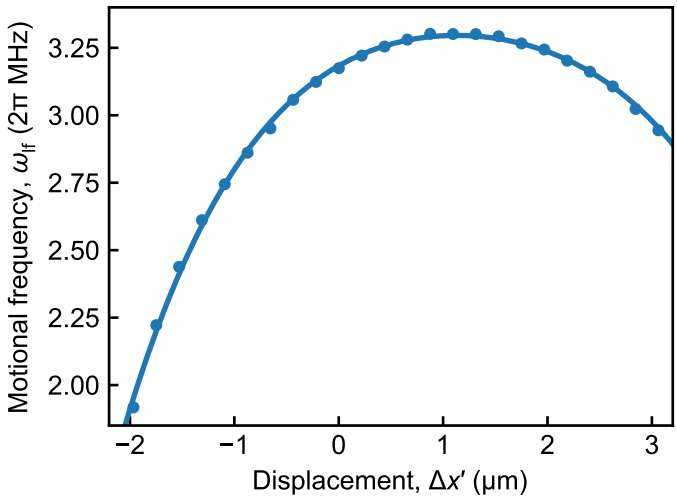

Figure 2.20: Exemplary characterization of the anharmonic contributions to the trapping potential of a single ion at T_0. For variable displacements along the low-frequency motional mode $\Delta x'$ we measure the corresponding motional mode frequency ω_{lf} (blue data points). We fit the data by a fourth-order polynomial (blue line) to interpolate the data. Error bars (SEM) are smaller than the marker size.

Figure 2.20, we show exemplarily the results of such a measurement for an ion trapped at site T_0. Here displacing the ion by 1 µm changes the motional frequency by more

than $2\pi\times0.5\,\mathrm{MHz}$. We fit the data by a fourth-order polynomial for interpolation. For our experiments, we try to optimize the positions of the ions close to a point where the motional frequency is first-order insensitive to displacements.

It is important to note that we here assume relevant anharmonic contributions only along the low-frequency motional mode and that the control potential displaces the ion along this motional mode. We assume that this limits the significance of the reconstructed anharmonic contributions for larger displacements ($> 1\,\mu\mathrm{m}$). Here, if needed, further studies tracking all three motional modes and ideally the ions position in all three dimensions using an additional camera detecting from the side might improve uncertainties.

2.4.5 Tuning motional modes and frequencies

We combine the aforementioned techniques of control potentials and motional-mode analysis to tune the motional mode orientations and frequencies in our experiment. In the following, we describe exemplary results for tuning the motional mode orientation at one trapping site of the triangle trap array, followed by results for real-time tuning, i.e. during an experimental sequence, as used for coupling experiments in this work.

Curvature tuning

To demonstrate the tuning of the in-plane orientation of $\boldsymbol{u}_{\mathrm{lf}}$ we examine two ions trapped at T_0 in the triangle trap array. For the coupling experiments, it is favourable to orient $\boldsymbol{u}_{\mathrm{lf}}$ towards the trapping site we want to couple to (see Section 2.5). We, therefore, realize two control profiles $\Phi_{\mathrm{ctrl,A}}$ and $\Phi_{\mathrm{ctrl,B}}$ where $\boldsymbol{u}_{\mathrm{lf}}$ is oriented towards T_1, along $\boldsymbol{x}$, or towards T_2, rotated by $\alpha_{\mathrm{ip}} = 60°$. In Figure 2.21, we show camera

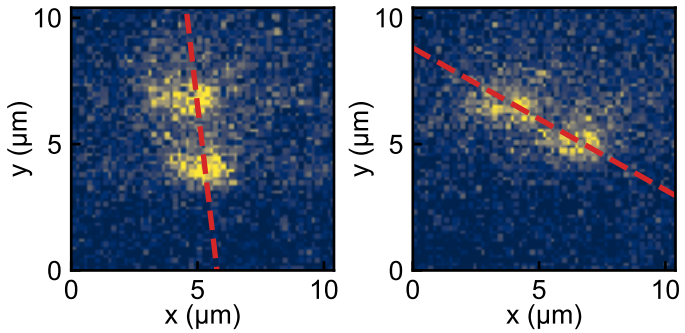

Figure 2.21: Experimental measurement of the low-frequency motional mode orientation at T_0. We load two ions which orient along the low-frequency mode and apply two control profiles $\Phi_{\mathrm{ctrl,A}}$ (left) and $\Phi_{\mathrm{ctrl,B}}$ (right). From fits of the ion centres we infer in-plane angles with respect to the y-axis of 7(2)° (left) an orientation towards T_1 and 60(2)° (right) an orientation towards T_2.

images of two ions at T_0 for each of these profiles. In profile $\Phi_{\mathrm{ctrl,A}}$, we have a residual

in-plane angle of $\alpha_{\mathrm{ip}} = 7(2)^\circ$ and for $\Phi_{\mathrm{ctrl,B}}$ $\alpha_{\mathrm{ip}} = 60(2)^\circ$ oriented towards T_2. To switch between the two profiles, we linearly ramp between the corresponding sets of control voltages $\boldsymbol{U}_{\mathrm{ctrl,A}}$ and $\boldsymbol{U}_{\mathrm{ctrl,B}}$:

$$\boldsymbol{U}_{\mathrm{ctrl}}(\kappa_{\mathrm{A-B}}) = \boldsymbol{U}_{\mathrm{ctrl,A}} + \kappa_{\mathrm{A-B}}\,(\boldsymbol{U}_{\mathrm{ctrl,B}} - \boldsymbol{U}_{\mathrm{ctrl,A}}) \tag{2.32}$$

Where we introduce a tuning parameter $\kappa_{\mathrm{A-B}} \in [0, 1]$. We analyse the effect of this ramp statically for intermediate values of $\kappa_{\mathrm{A-B}}$ and track the rotation angle and all three motional-mode frequencies ω_i of a single ion. Additionally, we calculate the sum of squared eigenfrequencies $\sum_i \omega_i^2$, which is proportional to the trace of the local $\mathbf{H}$ and unchanged by static electric fields. This value is, therefore, a measure of displacements of the ion in the radio-frequency field (Kalis 2017). We plot the data in Figure 2.22. Tuning $\kappa_{\mathrm{A-B}} \in [0, 1]$ smoothly changes the rotation angle and the motional frequencies, this is important as rapid (with respect to inverse motional frequencies), non-adiabatic changes of motional frequencies could lead to additional motional excitation. Furthermore, the motional frequencies do not cross, which could lead to a transfer of excitation between motional modes. The sum of squared eigenfrequencies changes by $< 10\,\%$, which we explain by a displacement of the ion smaller than 1 µm along $\boldsymbol{z}$ and displacements (detected by the camera) of < 0.3 µm in the $\boldsymbol{x}$-$\boldsymbol{y}$-plane.

Real-time tuning

During the coupling experiments, we want to change (ramp) between control profiles on timescales t_{ramp} of several 10 µs, fast compared to typical coupling and motional decoherence rates. We, therefore, want to choose t_{ramp} as small as possible without introducing additional motional decoherence. To analyse this, we perform a Ramsey-like motional coherence experiment (see Section 2.4.2) depicted in Figure 2.23 (top). We analyse the effect of ramping between two profiles similar to $\Phi_{\mathrm{ctrl,A}}$ and $\Phi_{\mathrm{ctrl,B}}$ above rotating the lowest-frequency mode by approximately 60° for a single ion at T_0. After the first excitation pulse, we ramp to the second control profile linearly in time t_{ramp} hold this profile for 20 µs, ramp back again in t_{ramp}, hold for 20 µs followed by the second excitation pulse. The waiting duration before the last pulse ensures that the voltages on the electrodes have settled and motional frequencies do not drift during the second excitation. We perform this experiment for variable t_{ramp} and extract the contrast. Additionally, we perform the same experiment without changing the voltages, to measure the intrinsic decoherence rate for comparison. In Section 2.2.4 (bottom) we plot the resulting data normalized to the contrast of $t_{\mathrm{ramp}} = 0$ for the calibration experiment with constant voltages. For short timescales ($t_{\mathrm{ramp}} < 20$ µs) we see a reduced contrast due to the ramp between profiles, which we attribute to decoherence induced by the ramp. From around 20 µs on the effect of decoherence due to the ramping is (within uncertainties) the same as when not changing the voltages. We, therefore, in this example, choose $t_{\mathrm{ramp}} = 20$ µs.

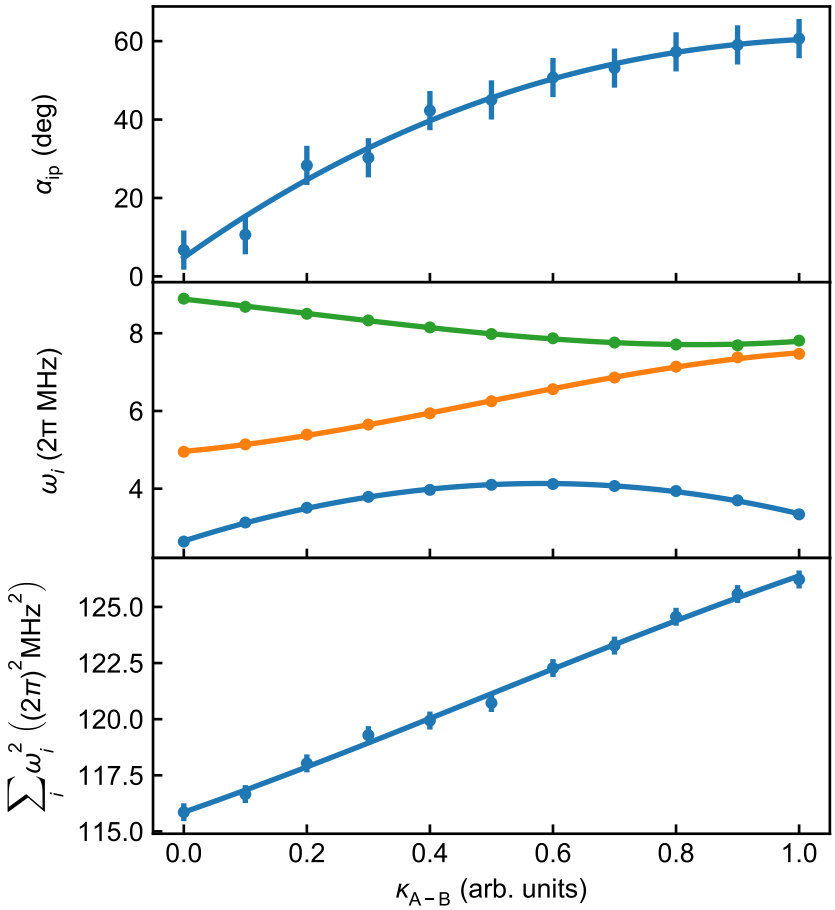

Figure 2.22: Linear tuning of the control profile at T_0 from $\Phi_{\text{ctrl,A}}$ with the low-frequency mode oriented towards T_0 ($\kappa_{A-B} = 0$) to $\Phi_{\text{ctrl,B}}$ with orientation towards T_1 ($\kappa_{A-B} = 0$). For variable κ_{A-B} we measure the motional mode orientation (top), all three motional frequencies of a single ion at T_0 (middle, colors indicated different motional modes), and calculate the sum of squared eigenfrequencies (bottom). The tuning angle shows a smooth transition from the configuration $\alpha_{ip} = 7(2)°$ to $\alpha_{ip} = 60(2)°$. During this tuning the low-frequency mode stays separated in frequency from the two higher-frequency modes. From the change in the sum of squared eigenfrequencies below 10 % we estimate a displacement along z smaller than 1 µm. Error bars indicate the SEM and lines are plotted as a guide to the eye.

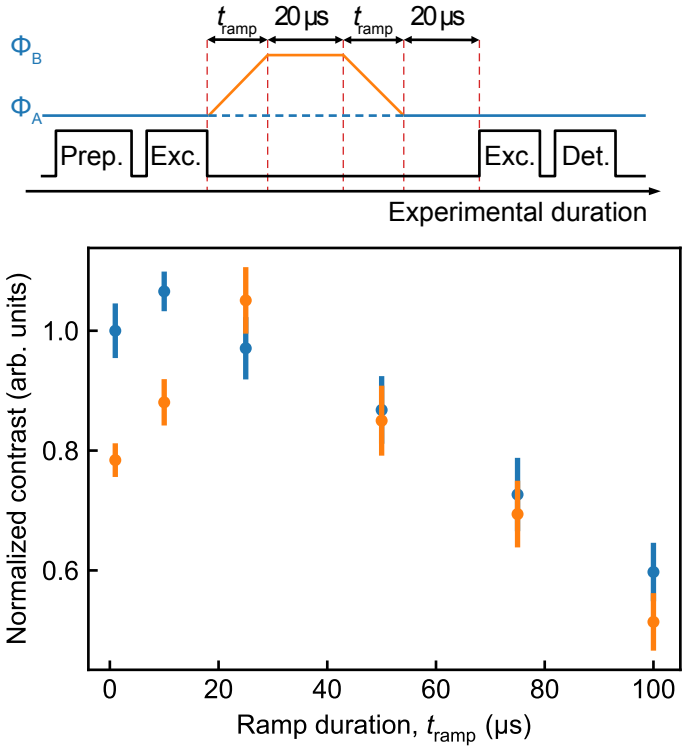

Figure 2.23: Calibration experiment to measure motional decoherence induced by ramping between control profiles. The experimental sequence (top) consists of a motional coherence measurement (see Section 2.4.2). During the two excitation pulses of we linearly ramp the control profile from $\Phi_{\mathrm{ctrl,A}}$ to $\Phi_{\mathrm{ctrl,B}}$ in a variable duration t_{ramp} followed by a constant holding duration of 20 µs, a second ramp back to $\Phi_{\mathrm{ctrl,A}}$ in t_{ramp} and a final holding duration of 20 µs (orange line). We additionally perform experiments of the same duration staying in $\Phi_{\mathrm{ctrl,A}}$ to estimate the dephasing rate not induced by ramping between profiles (blue dashed line). The normalized contrast as a measure for the coherence decreases for $t_{\mathrm{ramp}} = 20\,\mu\mathrm{s}$ when ramping (orange data points) with respect to the case without the ramp (blue data points). In this case we choose $t_{\mathrm{ramp}} \leq 20\,\mu\mathrm{s}$ as there the ramping does not induce additional decoherence. Error bars indicate the SEM.

2.5 Coupled harmonic oscillators

Inter-site coupling is the essential ingredient to make the toolbox of trapped-ion quantum simulations available in two-dimensional arrays of individually trapped ions. To realize this coupling, we make use of the electric charge of the ions, i.e. the Coulomb interaction. In Figure 2.24 we sketch a simple model of two-coupled ions where we

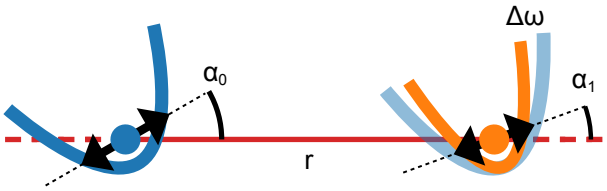

Figure 2.24: Model of two coupled harmonic oscillators. In a simplified picture we consider two ions, each harmonically trapped in an individual one-dimensional potential. We consider effects of a detuning $\Delta\omega$ between the motional frequencies and in-plane rotations of mode orientations from the connecting axis by angles α_0 and α_1. Figure adapted from Hakelberg et al. (2019).

simplify the problem to one motional-mode per ion and one rotational degree of freedom per site in a common plane. We consider two ions separated by distance r along the unit vector $\boldsymbol{e}_r$. For each ion, we consider the harmonic motion along one motional mode $\boldsymbol{u}_i$ with frequency ω_i, $i \in \{0, 1\}$. Each ion can be interpreted as an electric dipole $\boldsymbol{d}_i = d_i\, q_i\, \boldsymbol{u}_i$ with displacement d_i along $\boldsymbol{u}_i$ and charge q_i. Following Harlander et al. (2011), the energy of the dipole-dipole interaction is given by:

$$U_{\mathrm{dd}} = \frac{1}{4\pi\epsilon_0} \frac{\boldsymbol{d}_0\, \boldsymbol{d}_1 - 3\,(\boldsymbol{d}_0\, \boldsymbol{e})(\boldsymbol{d}_1\, \boldsymbol{e}_r)}{r^3} \tag{2.33}$$

with the vacuum permittivity ϵ_0. In a simple picture, the displacements of the ions are along the connecting axis $\boldsymbol{e}_r \parallel \boldsymbol{d}_0 \parallel \boldsymbol{d}_i$ and U_{dd} simplifies to:

$$U_{\mathrm{dd},\parallel} = -\frac{1}{4\pi\epsilon_0} \frac{2\,(d_0\, q_0\, d_1\, q_1)}{r^3} \tag{2.34}$$

The coupling rate is then given by (Brown et al. 2011; Harlander et al. 2011):

$$\Omega_{\mathrm{C,res}} = \frac{1}{2\pi\epsilon_0} \frac{1}{r^3} \frac{q_0\, q_1}{\sqrt{m_0\, m_1}\sqrt{\omega_0\, \omega_1}} \tag{2.35}$$

That is the rate with which the two oscillators if tuned to resonance, exchange their initial excitations. Our definition varies from that given in (Brown et al. 2011; Harlander et al. 2011) by a factor of two. For our definition, the energy is transferred between the oscillators such that after $(2\pi)/\Omega_{\mathrm{C,res}}$ the energy is transferred back and forth, reverting to the initial state. For the coupled case the individual coupled eigenfrequencies of the oscillators are detuned by the coupling rate $\Omega_{\mathrm{C,res}}$, a so-called avoided crossing.

In larger arrays, especially in two dimensions, non-parallel motional-mode orientations are relevant as tuning parameters. Considering rotations of $\boldsymbol{u}_i$ in a common plane with angles α_i with respect to $\boldsymbol{e}_r$ (see Figure 2.24) the dipole-dipole energy is given by:

$$\begin{aligned} U_{\mathrm{dd,rot}} &= \frac{1}{4\pi\epsilon_0}\frac{d_0\, q_0\, d_1\, q_1 \cos(\alpha_1-\alpha_0) - 3\, d_0\, q_0\, d_1\, q_1 \cos(\alpha_0)\cos(\alpha_1)}{r^3} \\ &= \frac{1}{4\pi\epsilon_0}\frac{d_0\, q_0\, d_1\, q_1}{r^3}\left(\cos(\alpha_0-\alpha_1) - 3\cos(\alpha_0)\cos(\alpha_1)\right) \\ &= -\frac{1}{4\pi\epsilon_0}\frac{d_0\, q_0\, d_1\, q_1}{r^3}\frac{1}{2}\left(\cos(\alpha_0-\alpha_1) + 3\cos(\alpha_0+\alpha_1)\right) \\ &= U_{\mathrm{dd},\parallel}\,\frac{1}{4}\left[\cos\left(\alpha_0-\alpha_1\right) + 3\cos\left(\alpha_0+\alpha_1\right)\right] \end{aligned} \tag{2.36}$$

Which in turn results in a coupling rate:

$$\Omega_{\mathrm{C,rot}} = \Omega_{\mathrm{C,res}}\,\frac{1}{4}\left[\cos\left(\alpha_0-\alpha_1\right) + 3\cos\left(\alpha_0+\alpha_1\right)\right] \tag{2.37}$$

$$= \Omega_{\mathrm{C,res}}\left[\cos\left(\alpha_0\right)\cos\left(\alpha_1\right) - \frac{1}{2}\sin\left(\alpha_0\right)\sin\left(\alpha_1\right)\right] \tag{2.38}$$

In Figure 2.25 we visualize this tunability of the coupling strength. Rotations allow

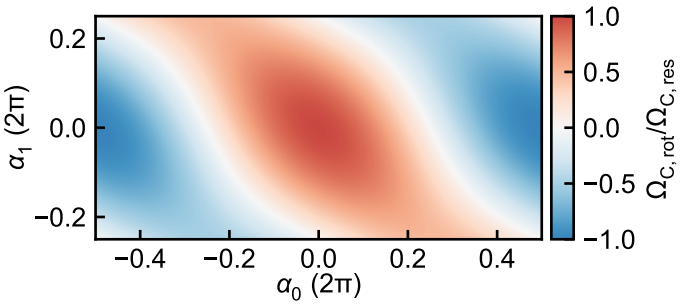

Figure 2.25: The effect of variable mode orientations on the coupling strength between the sites. We normalize the coupling rate $\Omega_{\mathrm{C,rot}}$ by the rate for collinear mode orientation $\Omega_{\mathrm{C,res}}$ ($\alpha_0 = \alpha_1 = 0$). For parallel mode orientations $\alpha_0 = \alpha_1 = 90\,^\circ$ the coupling rate is reduced by a factor of 0.5. Figure adapted from Hakelberg et al. (2019).

to tune the coupling strength up to switching off the coupling completely. In surface-electrode traps the close proximity of the trapping electrodes (on the same order as the inter-site distance) leads to additional effects: In Schmied et al. (2011) the authors investigate the effect of mirror charges induced in the surface and their effect on the coupling strength. We calculate that for our trap where the inter-ion spacing is equal to the ion-electrode distance the effects on the coupling rates are below 2 %.

Up to now we discussed resonantly coupled harmonic oscillators, i.e. the oscillation frequencies of the uncoupled oscillators are equal $\omega_0 = \omega_1$. A detuning of the frequencies

$\Delta\omega = \omega_0 - \omega_1$ yields an additional control parameter. Similar to Rabi-oscillations (cf. Section 2.1.1) the detuning leads to an increased coupling rate:

$$\Omega_{\mathrm{C,det}} = \sqrt{\Omega_{\mathrm{C,res}}^2 + (\Delta\omega)^2} \tag{2.39}$$

and a decreased coupling efficiency

$$\kappa_{\mathrm{C,det}} = \frac{\Omega_{\mathrm{C,res}}^2}{\Omega_{\mathrm{C,res}}^2 + (\Delta\omega)^2} = \frac{\Omega_{\mathrm{C,res}}^2}{\Omega_{\mathrm{C,det}}^2} \tag{2.40}$$

We define the coupling efficiency as the fraction of energy that is maximally transferred from an initially excited oscillator to the second oscillator initially at rest. In the resonant case, the efficiency is 1. In Figure 2.26 we illustrate numerically the excitation

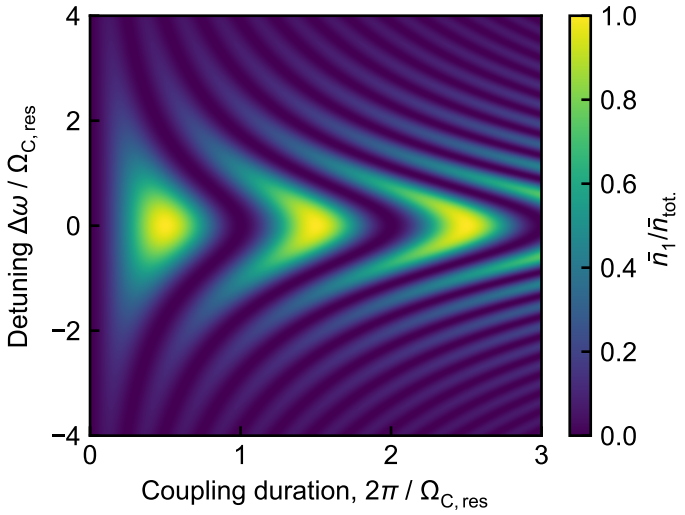

Figure 2.26: Illustration of the effects of a detuning on the coupling between two harmonic oscillators. We show the excitation amplitude at the second oscillator, initially at rest, relative to the total excitation. The excitation oscillates between the two sites. In the resonant case ($\Delta\omega = 0$) all excitation is transferred with a rate of $\Omega_{\mathrm{C,res}}$. A detuning leads to a faster coupling rate and a smaller efficiency, i.e., the maximally transferred excitations is smaller. Figure adapted from Hakelberg et al. (2019).

at the second oscillator as a function of the coupling duration and detuning. For zero detuning the excitation oscillates with $\Omega_{\mathrm{C,res}}$, transferring all initial excitation. In our experiments, we use the detuning to tune the coupling rate between sites. For typical resonant coupling rates on the order of $\Omega_{\mathrm{C,res}}/(2\pi) \approx 2\,\mathrm{kHz}$ and detunings $\Delta\omega/(2\pi) \approx 100\,\mathrm{kHz}$, we find $\kappa_{\mathrm{C,det}} \approx 1/(\Delta\omega)^2 \approx 1 \times 10^{-4}$.

In our coupling experiments, we work with coherent states of motion, therefore, *excitation* will refer to these states with amplitudes given in quanta, i.e. the expectation value of the coherent state amplitude. Furthermore, as we tune motional frequencies

adiabatically, i.e. slow with respect to inverse motional frequencies, the total motional excitation given by the sum of all coherent state amplitudes

$$\bar{n}_{\mathrm{tot}}(t) = \sum_i \bar{n}_i(t),$$

is, in theory, a conserved quantity.

2.5.1 Anharmonic effects

As explained above, in our experimental realisations of the coupling between single ions in the triangle trap array using large coherent states we see that anharmonic contributions to the trapping potential lead to a significant change in motional frequencies. This complicates the system in comparison to the model of two coupled harmonic oscillators. The anharmonic trapping potential leads to an effective motional frequency at each site that varies as a function of the motional amplitude. Therefore, during the coupling, the oscillators frequency difference is constantly changing and the oscillators cannot be described as *in resonance*.

To get a qualitative overview of this effect we simulate the coupling exemplarily for selected typical anharmonic contributions and motional mode orientations of two ions at sites T_0 and T_1. In Figure 2.27, we sketch the local motional frequencies as a function of

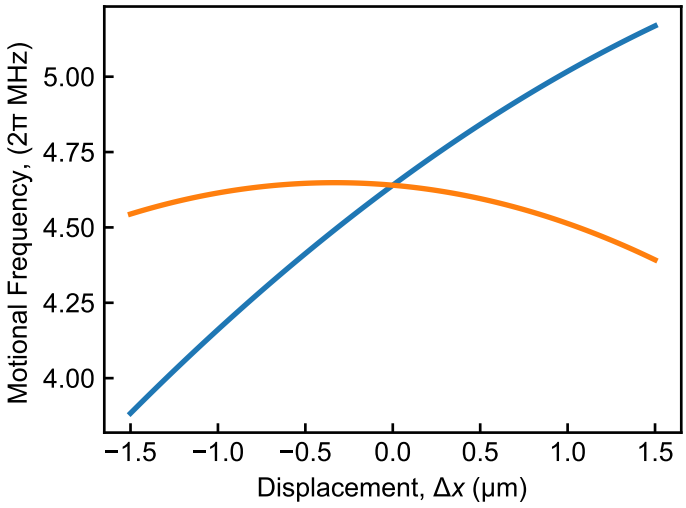

Figure 2.27: Motional frequencies as a function of the displacement along the low-frequency motional mode for site T_0 (blue line) and T_1 (orange line) as used for simulating the effect of anharmonic coupled oscillators.

the displacement along the low-frequency motional mode. For zero displacement the ion at each site oscillates with a motional frequency of $2\pi \times 4.64\,\mathrm{MHz}$. For the simulation, we initialize the ion at T_0 with an energy corresponding to about 1000 quanta calculated assuming a harmonic oscillator with motional frequency $2\pi \times 4.64\,\mathrm{MHz}$. We simulate

the coupling for variable additional detuning $\Delta\omega$ between the two sites that we introduce as an offset to the motional frequency at T_1. For comparison we perform the same simulation with two harmonic oscillators at $2\pi \times 4.64\,\mathrm{MHz}$, setting all higher-order contributions to the trapping potential to zero. In Figure 2.28 we plot the resulting

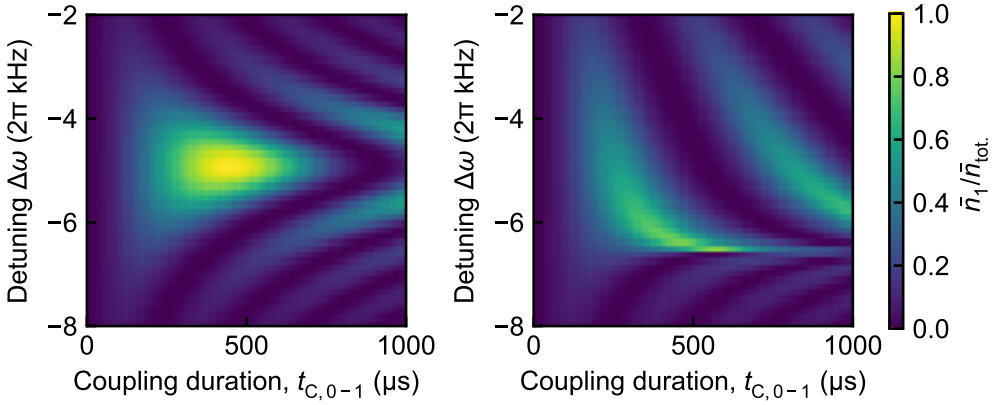

Figure 2.28: Simulated coupling experiment between two ions for variable detuning between the sites and variable coupling duration. We show the excitation at the second oscillator, initially at rest, as a function of the total excitation. On the left we simulate two harmonic oscillators, while on the right we introduce anharmonic contributions at both sites. This shifts and alters the observed resonance (see text for details).

motional excitation at T_1 normalized by the initial excitation and as a function of the detuning and the coupling duration for both the harmonic and anharmonic case. The harmonic simulation shows a resonance in agreement with the analytical function plotted in Figure 2.26, here with a coupling rate of $2\pi \times 1.2\,\mathrm{kHz}$ (as verified by Equation 2.35) and a complete transfer of motional excitation for a zero detuning. In the anharmonic case, this changes significantly. The resonance is shifted and becomes asymmetric. Additionally, the resonance features a sharp central feature of maximized coupling efficiency for a detuning of around $2\pi \times 3.5\,\mathrm{kHz}$. In our experiments due to fluctuations in motional frequencies on the order of $2\pi \times 1\,\mathrm{kHz}$, we cannot resolve this sharp feature. To simulate this, we produce an additional figure Figure 2.29 where we apply a Gaussian filter along the detuning axis with a width of $2\pi \times 1\,\mathrm{kHz}$ to emulate the effect of independent fluctuations of the motional frequencies. Compared to the harmonic coupling, this shows an increased coupling rate with a maximum coupling efficiency of in this case 45 % for a detuning of $\Delta\omega/(2\pi) = -5.3\,\mathrm{kHz}$. These simulations are in qualitative agreement with our experimental results where we see an increased coupling rate with respect to calculations for harmonic oscillators while the coupling efficiency is reduced. We, therefore, when describing our results in the context of anharmonic effects define an effective coupling rate $\Omega_{C,\mathrm{eff}}$.

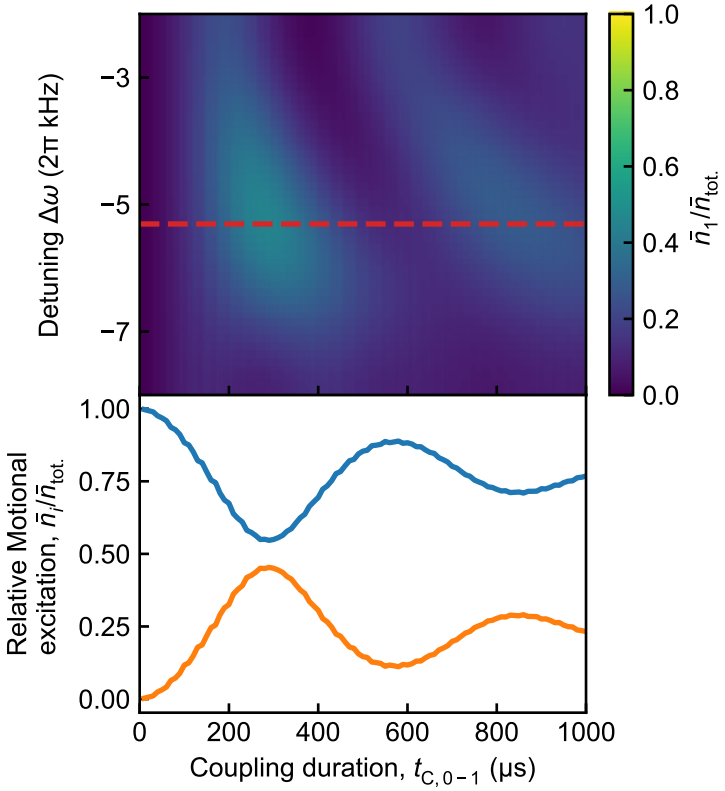

Figure 2.29: To emulate the effect of independent fluctuations of the motional frequencies we use the data of Figure 2.28 (right) and introduce a Gaussian filter with width $2\pi \times 1\,\mathrm{kHz}$ along the detuning axis (top). This smears out the sharp resonance and qualitatively resembles the data observed in the experiments. Additionally we plot the evolution of the relative motional excitation between the two sites (bottom) for a detuning of $2\pi \times -5.3\,\mathrm{kHz}$ (red dashed line in top plot). There the maximal excitation is transferred from T_0 (blue line) to T_1 (orange line).

3 Experimental Setup and Characterization

In this Chapter we give an overview of the experimental setup used for the results of this thesis. We start by a general overview of parts already described in previous publications, reference these and focus on changes and new components implemented during this work. For a general overview of experimental techniques used in our group for magnesium experiments, we refer to Friedenauer (2010). The design of the vacuum setup containing the triangle trap array trap is described in Ströhle (2011) the experimental setup further in Kalis (2017) and Mielenz (2016) and in parallel to this work in Kiefer (2019). We describe a new vacuum chamber that was designed to incorporate an argon-ion gun to implement in-situ surface cleaning of the trap chip (see Section 2.4.2). In this new apparatus, we additionally implemented a hybrid-system to realize a magnetic quantization field suitable for the field-independent qubit in magnesium (see Section 2.2.2). As a part of this, we characterized the system and published the results in Hakelberg et al. (2018). We will present these results in Section 3.4.

3.1 Experimental control system

In this Section, we describe the experimental control system. This consists of all components used to interface the trapped ions and the hardware and software to allow the user to interact with the system. The system is essentially divided into the optical setup used to interface with the electronic degrees of freedom, the electrical setup to control the motional degrees of freedom and the control electronics allowing pre-programmed real-time control of these components. In ion trap experiments typical experimental timescales and requirements on the time-resolution of the control system are given by the line widths of relevant electronic transitions ($\approx 2\pi \times 41\,\mathrm{MHz}$ for magnesium ions) and motional frequencies on the order of $2\pi\times(1\text{–}10)\,\mathrm{MHz}$. This leads to typical experimental durations on the order of (0.1–10) ms and time-resolution requirements on the order of 10 ns. These constraints cannot be easily matched by modern computer operating systems, which normally do not allow for real-time operation. Especially concurrently running processes lead to a non-reproducible jitter in code execution times. This creates the demand for designated real-time control hard- and software. Here, we will give a brief overview of the system, dependencies, and interconnections, followed by sections where we will further describe the electrical setup accessing the control electrodes of the trap, and the optical laser setup. A similar system using magnesium ions in a linear Paul trap is described in Friedenauer

(2010). Our system is described in detail in Kalis (2017) and Mielenz (2016).

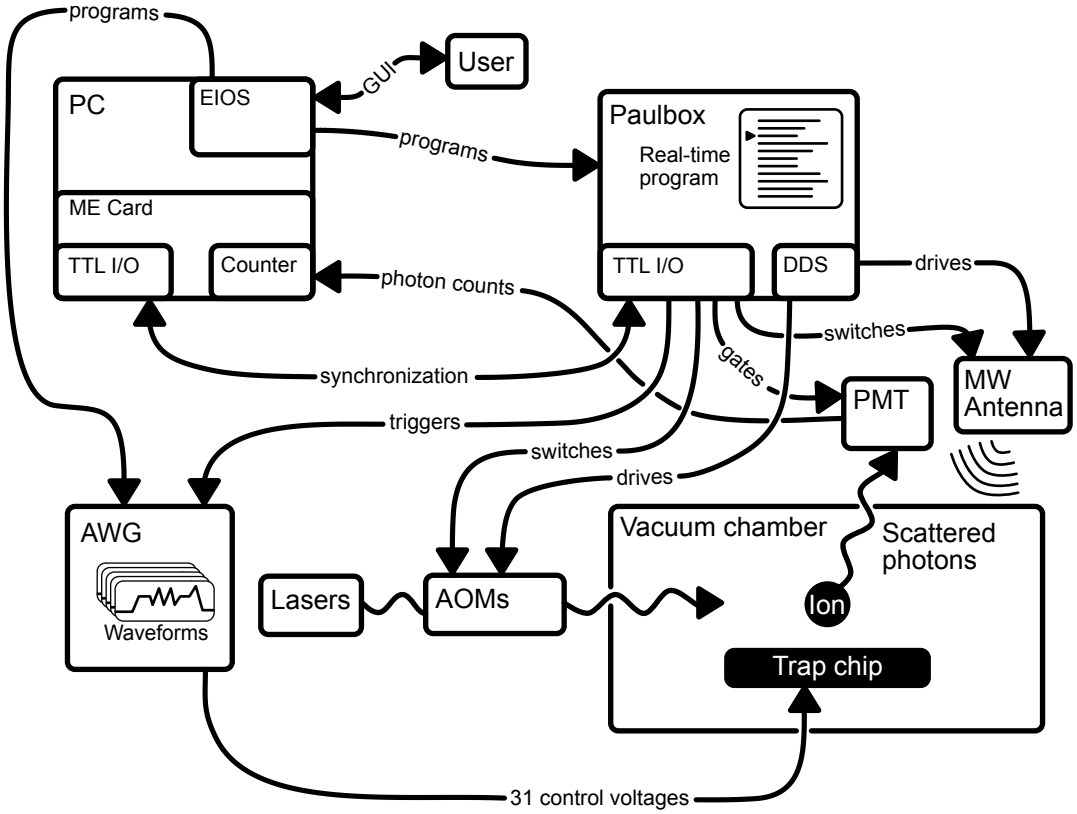

Figure 3.1: Schematic overview of the experimental control system (details see text). At the heart sits a real-time control unit *Paulbox* which is programmed by the user through a graphical user interface *EIOS*. The Paulbox controls all devices following a sequential program. The ion(s) are interfaced by lasers, microwave radiation and electronic potentials and emit photons which are detected by a photo-multiplier tube or (optionally) a camera not shown here.

In Figure 3.1 we depict the experimental control setup from the user to the trapped ion. The central control element is the *Paulbox* (Tan The Pham 2005), a pulse sequencer built around an FPGA[1] clocked at $2\pi \times 100\,\mathrm{MHz}$ running real-time programs that control digital (TTL[2]) inputs and outputs and frequency (DDS[3]) outputs. The user interacts with the system by a Graphical User Interface (GUI) *EIOS*[4] developed by Henning Kalis (Kalis 2017). The software EIOS runs on a desktop PC and allows the user to write experimental programs in a C-like dialect. The programs are compiled to a pulse sequence that is uploaded to the Paulbox. Details on the compiler architecture can be found in Mielenz (2016). The real-time program controls digital inputs and

[1]FPGA: Field Programmable Gate Array
[2]TTL: Transistor-Transistor Logic
[3]DDS: Direct Digital Synthesis
[4]EIOS: Experimental Input Output System

outputs and can set frequencies of integrated DDS devices. Digital outputs are used, e.g. to switch laser beams using acousto-optic modulators (AOMs, see Section 3.1.2), switch a microwave antenna (see Section 3.1.3), or trigger an arbitrary-waveform generator (AWG, see Section 3.1.1) controlling the voltages applied to control electrodes of the trap. Photons scattered by the trapped ions can be collected using an electron-multiplying charged-coupled device (EMCCD) camera[5] for spatially resolved imaging of the ions or for real-time detection by a photo-multiplier tube module[6] (PMT). The latter is digitally gated by the Paulbox. A data acquisition board[7] connected to the desktop PC via PCI is used as a digital counter for pulses from the PMT module and synchronizes the start and end of programs running on the Paulbox with the EIOS software.

3.1.1 Electrification

As explained in Section 2.4 we control motional degrees of freedom of the trapped ions using electrical control potentials. These potentials are generated by voltages applied to dedicated control electrodes of our traps. Typical experiments require to change these voltages individually during experimental sequences on timescales of single µs and to apply oscillating voltages with frequencies up to tens of MHz.

Arbitrary waveform generators

To match these requirements, we use arbitrary waveform generators (AWG) with individually programmable output channels for each control electrode. The AWG design was provided to us by the Ion Storage Group (NIST) and is described in Bowler et al. (2013). Details on our realisation of the AWG can be found in Mielenz (2016) and Wittemer (2015). Internally the AWG is based on an FPGA clocked at $2\pi\times50\,\mathrm{MHz}$. A software update allows to set a pre-scaler to double this clock to $2\pi\times100\,\mathrm{MHz}$. The FPGA interfaces with 16 bit digital to analog converters[8] connected to operational amplifiers[9] with a range of $\pm10\,\mathrm{V}$. Similar to the Paulbox, the AWG is pre-programmed when compiling the experimental program. During experiments, the Paulbox triggers the AWG to synchronize the waveforms with the experimental sequence. Waveforms consist of instantaneous, linear or higher-order changes of voltages, and a DDS functionality with time-dependent amplitude and frequency and variable phase relations, all individual for each control electrode. The outputs of the AWG are connected to the trap chip via a modular filter box outside the vacuum chamber to filter out noise, which could lead to motional decoherence.

[5] Andor iXon X885-UV (existing setup) / Andor iXon Ultra DU888 UCS-UVB (new setup)
[6] Hamamatsu H8259-01
[7] Meilhaus Electronics, ME-4670i
[8] Analog Devices AD9726
[9] Analog Devices AD8250

Filter box

For the experiments in the triangular trap array, the filter box consists of a 5.1 kΩ resistor, which in combination with the on-chip capacitors of 820 pF forms a low-pass filter with a time-constant of 4.2 µs and a cutoff frequency of $2\pi\times38.1$ kHz. This filter box with different resistance is described in Mielenz (2016). During this thesis, we found out that in this filter box a resistor was installed between the radio-frequency ground pin of the trap chip and the electrical ground of the experiment. This limited experiments as the trap ground, connected to the control electrodes via the filter capacitors, would vary for fast changes of control voltages (on the order of several µs). We replaced this resistor with a direct connection to the experimental ground. For the linear trap array, we designed a new filter box with circuit board based filters described in Nitzsche (2017).

Radio-frequency drive

The radio-frequency driving voltage is supplied to the trap via a helical resonator, which amplifies and filters the signal. The construction is described in Ströhle (2011) for the existing vacuum setup and in Nitzsche (2017) for the new setup. In the new setup, we additionally implement a radio-frequency mixer before the helical resonator, which we connect to one output of our AWG. This allows us to set the amplitude of the trapping voltage in real-time using our experimental control system. Additionally, in the new setup, after the helical resonator, we install a capacitive divider as used in Johnson et al. (2016) to measure the radio-frequency amplitude directly before the trap and to apply an additional radio-frequency drive near $2\pi\times55$ MHz to drive transitions between sublevels in the same hyperfine manifold (see Section 2.2.3).

3.1.2 Laser setup

To access the electronic degrees of freedom of the magnesium ions we use lasers. The optical transitions (Section 2.2.1) are all in the ultraviolet range around 280 nm. As lasers are not available directly at these wavelengths we employ fibre lasers in the infrared (1120 nm), each followed by two second-harmonic generation stages in bow-tie cavity setups (Friedenauer et al. 2006), except for the optical pumping setup where the first frequency doubling is performed in a periodically-poled lithium niobate (PPLN) waveguide (Kiefer 2013). Additionally, we realize a photo-ionization laser near 285 nm to produce magnesium ions from neutral magnesium atoms via a two-photon process. This light is generated by frequency doubling light near 570 nm generated by a dye-laser. The following is a brief summary of some aspects of the optical setup. A setup similar to ours is extensively described in Friedenauer (2010), and for our setup in Kalis (2017) and Mielenz (2016).

We stabilize our lasers to transitions ion iodine molecules (I_2) around 560 nm, after the first frequency doubling stage with a precision better than 1 MHz. As this stabilisation is bound to defined resonances we have to fine-tune the laser frequencies to reach the desired transitions of magnesium. Further, experiments require that we

can switch laser beams on the timescale of 1 µs and set frequencies with a precision down to 1 kHz. To fulfil these requirements, we employ acousto-optic modulators (AOM) (Friedenauer 2010).

An AOM consists of an optically transparent material. A radio-frequency transducer, driven by an oscillating voltage of typically $2\pi\times(100\text{–}200)$ MHz, creates sound waves in the material which create a grating of variable refractive index. The laser beam is diffracted on this grating. The diffracted light is shifted in frequency by multiples (orders) of the driving frequency. Typically, we use the first diffraction order, generating light that is shifted once in positive or negative direction by the driving frequency. The efficiency of this process can be above 80 %. Additionally to the frequency shift, the beam exits the crystal under a deflection angle proportional to the diffraction order and driving frequency. To compensate this, we operate most AOMs in *double-pass* configuration where the beam passes the AOM twice such that the deflection angles cancel each other out and the resulting beam is shifted by twice the driving frequency. Here efficiencies of above 60 % are achievable. Electronically controlling the driving frequency and amplitude allows direct control over the laser frequency in range of a few tens of MHz, and amplitudes on timescales on the order of a few 100 ns (limited by the beam waist and speed of sound in the AOM material).

In the following, we will give a brief overview of the laser setups used for Doppler cooling and Detection, and optical pumping laser setup for preparation and manipulation of the qubit. The Doppler cooling and detection setup was changed during this thesis from the one described in Kalis (2017) to allow for more efficient use of the available laser power and easier adjustment. The new setup and changes we implemented are described thoroughly in Kiefer (2019). The Raman and optical pumping setups were used as described in Kalis (2017).

Doppler cooling and detection setup

The laser system described here is used for cooling and detection on the cycling transition ($|\mathrm{S}_{1/2}, \mathrm{F}=3, \mathrm{m_F}=+3\rangle \leftrightarrow |\mathrm{P}_{3/2}, \mathrm{F}=4, \mathrm{m_F}=+4\rangle$) near 280 nm. We generate σ^+-polarized beams of three different frequencies for different purposes:

The first beam is used for resonant detection. In previous publications of our group, this beam was detuned by $-2\pi\times 5$ MHz *red* from the cycling transition. This was done as a precaution to ensure that variations in the frequency lock setup $< 2\pi\times 5$ MHz would not lead to a *blue* detuning with respect to the transition, which in turn would lead to heating. During our experiments, we realized that this detuning can lead to a cooling of motionally excited ions, resulting in incorrectly reconstructed motional states (see Section 2.4.2). The variations in frequency were due to a VCO[10] employed to generate a frequency modulated signal in the iodine locking setup. This VCO shows a drift of a few MHz around the target value (approx. $2\pi\times 80$ MHz) on the timescale of seconds, which we attribute to temperature fluctuations. We replaced this setup by a different frequency generator with a modulation input[11]. With this setup, we

[10] Voltage Controlled Oscillator
[11] Hewlett-Packard HP 8640A

observe no frequency drifts of the oscillator (measured with a precision $< 1\,\mathrm{kHz}$). This allows us to stabilize the laser to better than $2\pi\times1\,\mathrm{MHz}$ as required for our motional state reconstruction (see Section 2.4.2).

The second beam is used for Doppler cooling. It is detuned by $\Gamma/2 \approx 2\pi \times 20\,\mathrm{MHz}$ *red* from the cycling transition for Doppler cooling as described in Section 2.4.1.

The third beam is an additional Doppler cooling beam detuned by $2\pi \times 330\,\mathrm{MHz} \approx 8\Gamma$. It allows cooling of ions with motional energies too large for efficient cooling by the closer detuned beam.

We overlap all beams and focus them on the ions above the trap chip. In the triangle trap array, the beams propagate along the $(\boldsymbol{x} + \boldsymbol{y})$-direction, in the linear trap along the $(\boldsymbol{x} + \boldsymbol{z})$-direction. For the triangle trap array, we additionally place a cylindrical lens in the beam path to widen the beam in the trap-chip plane. This allows to illuminate the three ions approximately equally (in-plane beam waist larger than $100\,\mu\mathrm{m}$) while reducing reflections on the trap surface (out-of-plane beam waist on the order of $20\,\mu\mathrm{m}$). Additionally, for this trap, we employ a focused detection beam (beam waist on the order of $10\,\mu\mathrm{m}$, see also Kiefer (2019)), which we can translate via piezoelectric stages[12]. This allows us to move the beam to a selected trapping site and thereby locally detect the (motional) state of a single ion in the array.

Optical pumping setup

The optical pumping setup is constructed similar to the Doppler cooling setup (Mielenz 2016). It addresses the $\mathrm{S}_{1/2} \rightarrow \mathrm{P}_{3/2}$ via two dedicated σ^+-polarized beams coupling to the $|\mathrm{S}_{1/2}, \mathrm{F} = 3\rangle$ and $|\mathrm{S}_{1/2}, \mathrm{F} = 2\rangle$ manifolds. This allows optically pumping the ion to the $|\mathrm{S}_{1/2}, \mathrm{F} = 3, \mathrm{m_F} = 3\rangle$ state (see Section 2.2.3). We overlap these beams with the Doppler cooling and detection beams before entering the vacuum chamber.

3.1.3 Microwave setup

The microwave setup is used to drive transitions between the $\mathrm{F} = 2$ and $\mathrm{F} = 3$ manifold of the $\mathrm{S}_{1/2}$ level of $^{25}\mathrm{Mg}^+$. For the magnetic fields used here, the transitions are on the range of $2\pi\times(1500\text{–}2000)\,\mathrm{MHz}$. Our experimental setup does not allow for direct synthesis of frequencies in this range. The DDS devices installed in the Paulbox operate at a clock rate of $\omega_{\mathrm{DDSclock}}/(2\pi) = 1100\,\mathrm{MHz}$ and as such allow for synthesis of frequencies ω_{DDS} up to $\omega_{\mathrm{DDSclock}}/2/(2\pi) = 550\,\mathrm{MHz}$. The spectrum of the DDS output however also contains a *mirror* frequency located at $\omega_{\mathrm{mirror}} = \omega_{\mathrm{DDSclock}} - \omega_{\mathrm{DDS}}$, in our case in the range of $2\pi\times(1100\text{–}550)\,\mathrm{MHz}$. Additional frequency doubling of this signal allows us to reach the desired range, spanning $2\pi\times(2200\text{–}1100)\,\mathrm{MHz}$. In Table 3.1 we list all components we use to realize the frequency generation described above. Several amplifiers and attenuators are used to operate the devices within their input-power specifications, especially the frequency multiplier.

To characterize our system, we measure the power at selected frequencies before the main amplifier (see Figure 3.2). In the range relevant to the results presented

[12] Physik Instrumente Q-522.030

Device	Output Range [(2π) GHz]	Type
Paulbox DDS	0–0.55 & 0.55–1.1	
Switch	0–0.55 & 0.55–1.1	MiniCircuits ZASW-2-50DR
Bandpass	0.55–1.1	MiniCircuits VBFZ-925-S+
3× Amplifier	0.55–1.1	MiniCircuits ZX60-8008E-S+
Attenuator	0.55–1.1	MiniCircuits VAT-4+
Frequency Multiplier	0.55–1.1 & 1.1–2.2	MiniCircuits ZX90-2-11-S+
Bandpass	1.1–2.2	MiniCircuits VBFZ-1690-S+
Amplifier	1.1–2.2	MiniCircuits ZX60-4016E+
Attenuator	1.1–2.2	MiniCircuits VAT-8+
Bi-Directional Coupler	1.1–2.2	OmniSpectra 20063-20
Main amplifier	1.1–2.2	MiniCircuits ZHL-30W-252-S+
Antenna	1.1–2.2	Home built

Table 3.1: Devices used to generate the desired microwave radiation in the range of $2\pi\times(1.1\text{–}2.2)\,\mathrm{GHz}$. See full text for details.

here ($2\pi\times(1540\text{–}1760)\,\mathrm{MHz}$), the power varies by $< 3\,\mathrm{dB}$. This could be improved for instance by frequency-dependent attenuation of the signal, however, for our application, this is not needed. To apply the microwave radiation to the ion we employ a home built bi-quad antenna constructed from silver wire and optimized for $2\pi \times 1.6\,\mathrm{GHz}$ (Tec et al. 2012). For the new setup, we position the antenna to optimize the coupling rate and find an optimized position below the breadboard carrying the optics around the chamber.

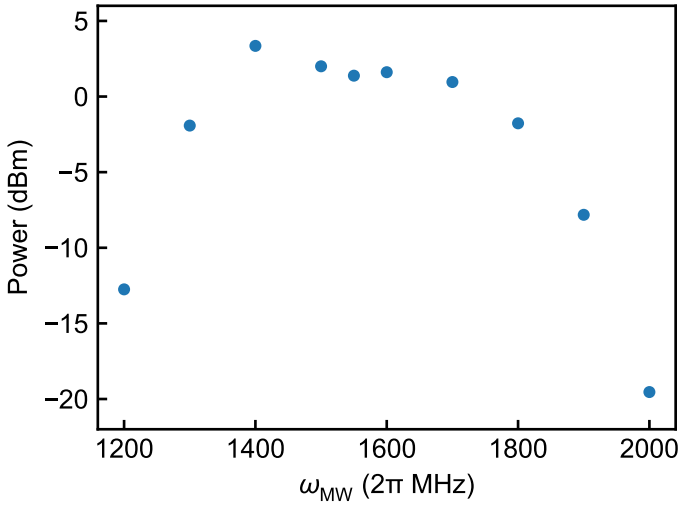

Figure 3.2: Measured microwave power before the main amplifier (see text) as a function of the desired microwave frequency. For experiments presented here we work in the range of $2\pi\times(1540\text{–}1760)\,\mathrm{MHz}$. In this range the power varies by $< 3\,\mathrm{dB}$. Error bars (SEM) are smaller than the marker size.

3.2 The established vacuum chamber

Experiments with single trapped ions require a strong isolation from the environment. In particular, traps need to be operated in the ultra-high vacuum regime $< 10^{-10}\,\mathrm{mbar}$ where collision between the ions and residual atoms are rare compared to typical experimental timescales. These collisions can lead to various effects, from altering the quantum state of the ions, to motional heating, the formation of molecules (e.g., $Mg^+ + H_2 \rightarrow MgH^+ + H$, see Mølhave and Drewsen (2000)), and especially for surface-electrode traps to a loss of ions due to transferred kinetic energy.

At the beginning of this thesis, one surface-electrode ion trap measurement setup was available in our group. The vacuum chamber was constructed by Johannes Ströhle (Ströhle 2011) in Munich and was moved to Freiburg later on. This setup is additionally described in Kalis (2017) and Mielenz (2016). During this thesis, we constructed and built a second vacuum chamber suitable for the same trap architecture but with the additional scope of implementing the possibility for in-situ surface cleaning of the chip by argon-ion bombardment (see Section 2.4.2). We will describe this setup in the following Section. As that new setup follows many general considerations already implemented in the previous setup we would like the reader to refer to the literature given above for further details on the first vacuum chamber.

3.3 The new apparatus - Setup

During this thesis, a new experimental apparatus for surface-electrode traps was designed, constructed, assembled, and used to perform first measurements. The vacuum chamber was designed to be compatible with traps used in the established setup while offering a new essential feature: As described in Section 2.4.2 motional heating is a fundamental problem in surface-electrode traps due to the close proximity of the ions to the electrodes. Therefore, the new setup was designed to implement in-situ cleaning of the trap chips using argon ion bombardment (Hite et al. 2012). For this, we constructed a specially designed top flange, supported by a design provided to us by Dustin Hite from the ion storage group (NIST). The flange is designed around an ion gun that can be used to clean the trap surface in-situ:

The ion gun The ion gun is a commercially available product distributed by rbd instruments (IG2 Ion Source Package) consisting of the gun (04-165) and an external control unit (32-165). The gun can be mounted to a vacuum chamber by a CF40 flange. Between the chamber and the gun, a flexible bellow allows to adjust the angle of the gun and thereby the position of the argon-ion beam on the trap surface. Inside a filament can be heated to ionize gases, such as argon, which has to be supplied to the chamber at a pressure of 6.67×10^{-5} mbar or lower. These ions are then accelerated by a voltage of up to 2 kV. The specifications (*IG2 ion source package Datasheet* n.d.) state that the resulting beam has a diameter of FWHM 2.5 mm at a distance of 25 mm and 3.5 mm at a distance of 50 mm. In a different setup, we performed characterization measurements, initially started by Raphaël Saint-Jalm during an internship in our group. In these measurements, not part of this thesis, we characterised the working parameters of the argon gun and confirmed the argon beam diameters given by the manufacturer.

In the following, we will describe the design of the new vacuum chamber, the imaging optics, and the implemented loading procedure using ablation loading. Additionally, we describe the implementation of a hybrid magnetic field setup to realize the field-independent qubit described in Section 2.2.2 based on a combined assembly of permanent magnets and coils.

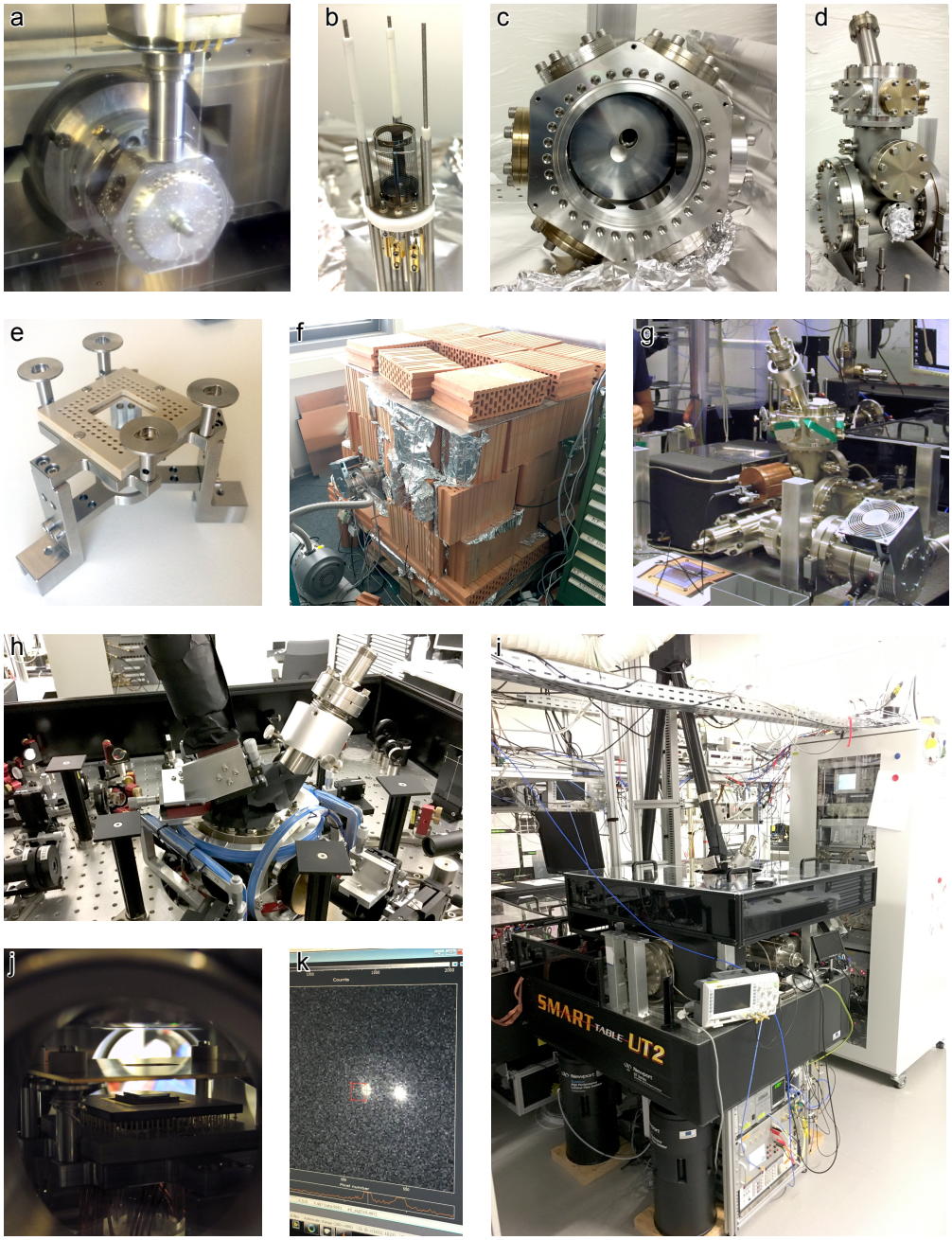

Figure 3.3: Evolution of the new experimental setup. (a) Machining of the hexagon in the mechanical workshop of the physical institute. (b) Disassembled argon-ion gun filament assembly. (c) View of the top flange mounted on the hexagon with holes for imaging and argon ions. (d) Assembled central part of the chamber. (e) Test assembly of the chip mount. (f) Brick oven to bake out the chamber with the turbo-pump and attached scroll-pump visible (g) Chamber on the optical table after bake-out. (h) Laser and detection optics and solid-state magnets and coils installed around the chamber. (i) Complete setup on the optical table including electronics below the table. (j) View of the trap chip inside the camber through a viewport with the gold covered shield above the trap. On the pillar (left, front) the magnesium wire ablation target is visible (k) First trapped ions.

3.3.1 Vacuum chamber

The main component of the new setup is the vacuum chamber. The requirement of ultra-high vacuum conditions with a pressure below 10^{-10} mbar leads to special requirements on the vacuum pumps, the design of the chamber in terms of geometry and available materials, and during assembly:

Materials Special materials with low outgassing (slow release of gas from the bulk material) are required. Additionally, the vacuum system has to be *baked-out*. This means the heating of the complete assembly to above 100 °C for several days to weeks while pumping the chamber, to release water adsorbed on the surfaces inside the chamber. Under ambient temperature this water will evaporate slowly, limiting the pressure to on the order of 10^{-6} mbar (or worse, depending on the pumping capacity). During the bake-out, this evaporation is accelerated enough such that the amount of water in the chamber will decrease significantly. Materials that satisfy these constraints include stainless-steel and copper for construction, Macor ceramic and PEEK as isolators for construction, glass for optical access, Kapton[13] as isolation for wires, but excludes plastics and porous materials. Additionally, to minimize stray magnetic fields that would have to be compensated for, we choose to produce all stainless-steel parts from a steel with low magnetic permeability[14].

Design The design should limit the surface inside the vacuum, as outgassing from surfaces limits the final vacuum pressure. Vacuum pumps should be directly connected to the chamber, as long, thin connections will limit the pumping efficiency. *Virtual* leaks should be avoided, this means holes in the chamber that are filled with air and connected to the residual volume only by a small opening, which will appear like a constant leak to the system. All interconnections should be made with metal sealed flanges We are using CF type vacuum flanges[15] with silver-coated copper gaskets. For viewports, we use additionally annealed gaskets that are softer and recommended by the manufacturer for some of the viewports. The gaskets should only be used once.

Fabrication During fabrication of metallic parts, additional care has to be taken not to produce virtual leaks. Especially welding of parts should be done on the inside of the chamber, such that the weld seam forms a smooth surface on the vacuum side.

Assembly During assembly, care has to be taken not to contaminate the chamber with materials that will lead to additional outgassing. Especially organic components and greases cannot be used. Therefore, all components are cleaned by ultrasonic cleaning using various solvents. After coarsely cleaning all parts with water we use the following sequence of solvents: First a soap and water solution[16], followed by

[13] Kapton® is a polyimide film trademarked by DuPont
[14] Type 1.4429, also known as (especially in the US) 316LN-ESU
[15] ISO 3669:2017 vacuum technology – bakeable flanges – dimensions of knife-edge flanges
[16] Tickopur R33

isopropyl alcohol and finally acetone. For all steps, we leave the parts in the ultrasonic bath for at least 10 min but typically several hours. The cleaned parts are wrapped in aluminium foil for transport and storage. All handling is done wearing latex gloves. The assembly is done in our clean laboratory environment wearing a clean-room overall. This limits contamination with grease (fingertips), other organic components (skin and hair) and dust particles.

Design considerations and overview

In comparison with the established setup (Section 3.2, Ströhle (2011)) additional restrictions are the implementation of in-situ cleaning of trap chips by argon-ion bombardment (cf. Section 2.4.2): Firstly, the argon-ion gun has to be implemented in the top flange, in addition to the viewport for imaging optics. Secondly, the vacuum setup has to allow to flood the chamber with argon at a defined pressure and allow pumping back to ultra-high vacuum conditions without breaking the vacuum. As a third point, the chip holder has to be adapted from the design by Ströhle (2011). In the following, we will describe the design of the chamber with a focus on the differences to the established setup. For further, general considerations on our vacuum chambers we refer to Ströhle (2011). In Figure 3.4 we show a rendered overview of the finished, assembled chamber. The chamber is built around a central cross. In the lower plane, it connects to the vacuum pumps and gauge and the valve allowing controlled inlet of argon. On top sits the chip-holder inside a hexagon that allows optical axes through six viewports in the horizontal plane. It is closed up on the top with the top flange incorporating the argon-ion gun and the viewport for the imaging optics.

Vacuum pumps

To pump the chamber from ambient pressure to ultra-high vacuum we employ several pumps. The first stage is a turbomolecular pump[17] pre-pumped by a scroll pump[18]. Those pumps allow to reach a pressure of low 10^{-9} mbar. We directly connect the turbomolecular pump to the system via a flange of the same diameter as the pump (CF100, 100 mm) to allow for a high as possible pumping rate. To pump the system further we employ an ion-getter pump with an integrated mount for a titan-sublimation pump[19]. These two pumps allow us to reach a final pressure of approximately 1×10^{-11} mbar. They are directly connected to the main chamber and define the size of the chamber. To measure the pressure in the ultra-high vacuum regime we use an ion gauge[20] calibrated down to 10^{-12} mbar.

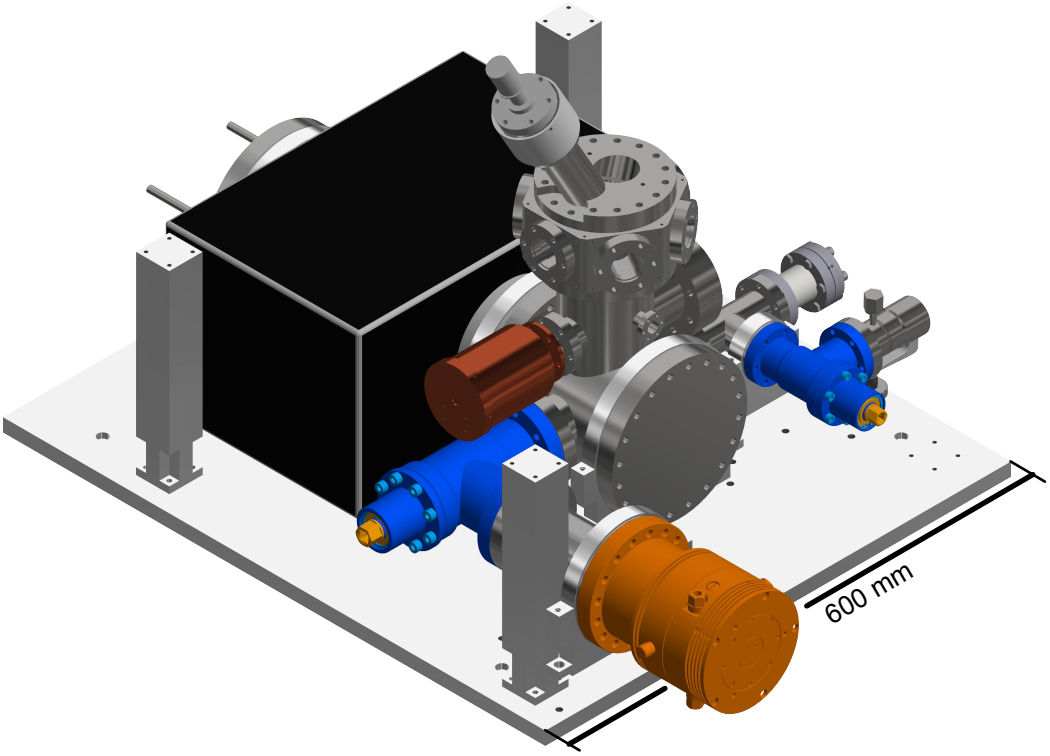

Figure 3.4: Rendered overview of the newly designed vacuum chamber. The whole chamber is assembled on an aluminium breadboard. Four pillars around the chamber (one not shown) on the outside allow to hold a breadboard to mount optics in a plane with the trap chip. The turbomolecular pump (orange) is used to pre-pump the chamber. The two angle-valves (blue) allow to close off the central chamber which is then pumped by the ion-getter pump (black). In the centre inside the hexagonal viewport assembly sits the trap chip. Radio-frequency is supplied via the spherical resonator (copper coloured). On top is the top-flange with the argon-ion gun.

Top flange

The top flange was newly designed based on considerations by Raphaël Saint-Jalm, supported by a design by Dustin Hite from the ion storage group (NIST). We changed the design in particular to minimize the angle between the detection viewport and the trap normal. Especially for imaging optics with a shallow depth of field a small angle is essential to be able to image two-dimensional structures (e.g. ion trap arrays) in focus. Additionally, the viewport should be as close to the trap chip as possible, for a fixed size of the viewport, to allow for a greater detection efficiency of the system.

[17] Agilent TwisTorr 304FS
[18] Agilent SH0112
[19] Agilent VacIon Plus 300 Starcell and integrated titan-sublimation pump
[20] Vacom Barion extended

Finally, the flange was designed such that it could be mounted on the established setup, i.e. the angled argon-ion gun and detection viewport are oriented towards a centre point of the trap that is at the same distance in that setup. In Figure 3.5 we show a cut-through render of the top flange assemble onto the chamber. On the left, the argon-ion gun is visible including the electrodes. It is mounted inside a tube that is welded into the flange at the bottom. The gun is mounted under an angle of 30° with respect to the vertical direction (trap normal). The front electrode has a distance of about 58 mm to the centre of the trap chip. The viewport for optical detection is installed under an angle of 16° and with a distance of 31 mm to the trap chip (measured from the bottom centre of the viewports flange). The angle for optical detection is limited by the viewport's diameter of 16 mm to 14.5° (centre to edge of the viewport). This amounts to 1.6 % of the total angle from the ion. For comparison, this in the established setup the value is 6.8 % (Ströhle 2011).

Chip holder

In Figure 3.6 we show a rendered image of the chip-holder assembly. Three feet are used to mount the chip holder to the chamber walls. Below the chip, a Macor disk is installed with holes carrying two magnesium ovens (not shown). The oven design follows the one described in Ströhle (2011): A piece of magnesium wire (diameter 1 mm is enclosed in a Tantal tube. Tantal wires point welded to the tube allow the application of a current (on the order of (1–5) A), resistively heating the tube and magnesium. By this, a beam of atomic magnesium vapour can be created. The oven assembly is surrounded by a cylindrical tube of fused silica glass. This shields atomic vapour not directed at the trap chip. Both Macor and fused-silica are chosen for their temperature resistance as, when in use, the oven heats to around 300° (Schaetz 2001). Shortly before assembly, the magnesium wires oxide layer is removed by formic acid. In previous publications, citric acid was used where the formation of a citric layer was proposed that would shield the magnesium from further oxidation and reduce sudden evaporation of large blobs of magnesium (Schaetz 2001). In our experiments, we did not observe such behaviour but did not perform an analysis of formic acid versus citric acid, as we quickly resorted to ablation loading (see Section 3.3.3).

The chip socket is made from two PEEK pieces, which fix 50 pin receptacles[21]. The trap chip carriers' pins are fixed inside these receptacles that are, on the bottom, crimped to copper wires with Kapton isolation. The wires (not shown in the picture) are connected to two ultra-high vacuum compatible D-SUB-25 plugs[22] that are connected to the outside of the chamber via two D-SUB-25 feedthroughs[23]. The pin used to apply the radio-frequency voltage to the trap is connected to the outside of the chamber via a high-power feedthrough. In the existing vacuum chamber, a hollow feedthrough was used that had to be closed to be vacuum compatible following a special procedure

[21] Mill-Max, 0672-4-15-15-30-27-10-0
[22] Allectra 211-FS25-UHV
[23] Allectra 210-D25-C63-2

(Ströhle 2011). As this presents a fragile point in the setup potentially breaking the vacuum we choose a solid feedthrough[24].

Four pillars around the trap chip carry a metallic shield (made from oxygen-free copper and coated with a 4 µm layer of gold) above the trap and isolated from the pillars by PEEK spacers. In the existing setup, these spacers were fabricated from Macor ceramic that is fragile such that the spacers could break during assembly, e.g. when exchanging the trap chips. The use of PEEK material removes this risk. The overhangs on the top of the pillars ensure that there is no direct line-of-sight between the trap and the isolating spacers on which electrical charges could accumulate. The shield has a cut-out space for the detection optics and the argon-ion beam. In the existing setup, an optically high-transmissive metallic mesh was used instead of the shield. This is not an option here as it would interfere with the argon-ion beam. In Figure 3.7 we show a top view of the chip mount installed the vacuum chamber here additionally the solid-state magnet assembly installed in front of two viewports is sketched (see Section 3.3.4).

[24] Pfeiffer Vacuum 420XST040121501

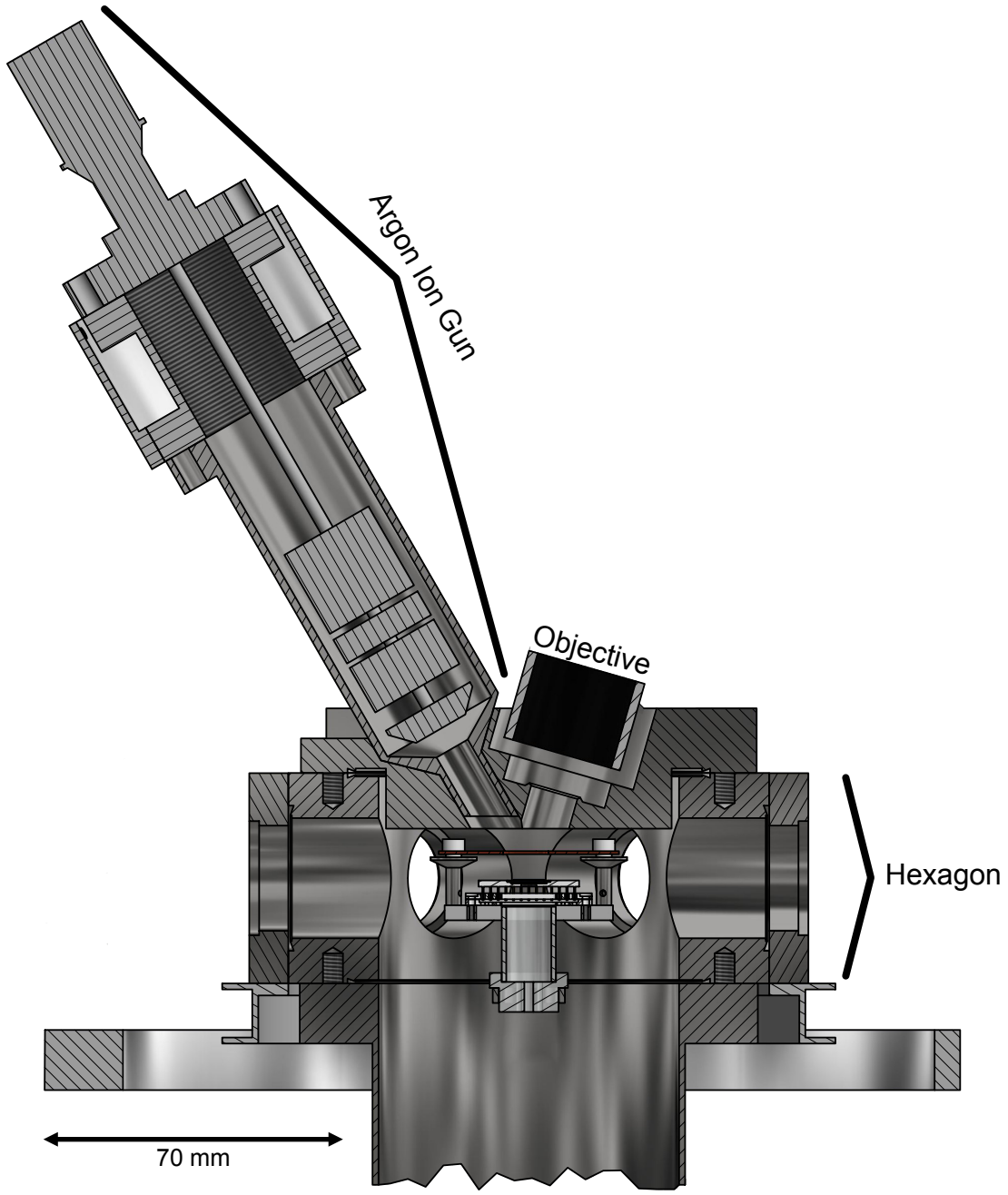

Figure 3.5: Cut-through render of the top flange, mounted on the vacuum chamber including the chip carrier. The argon ion gun mounted on the left will allow in-situ cleaning of the trap surface. Mounted under an angle of 30° with respect to the trap normal it leaves room for the imaging optics to the right under an angle of 16° where we show the objective in black. Both aim the centre of the trap mounted below.

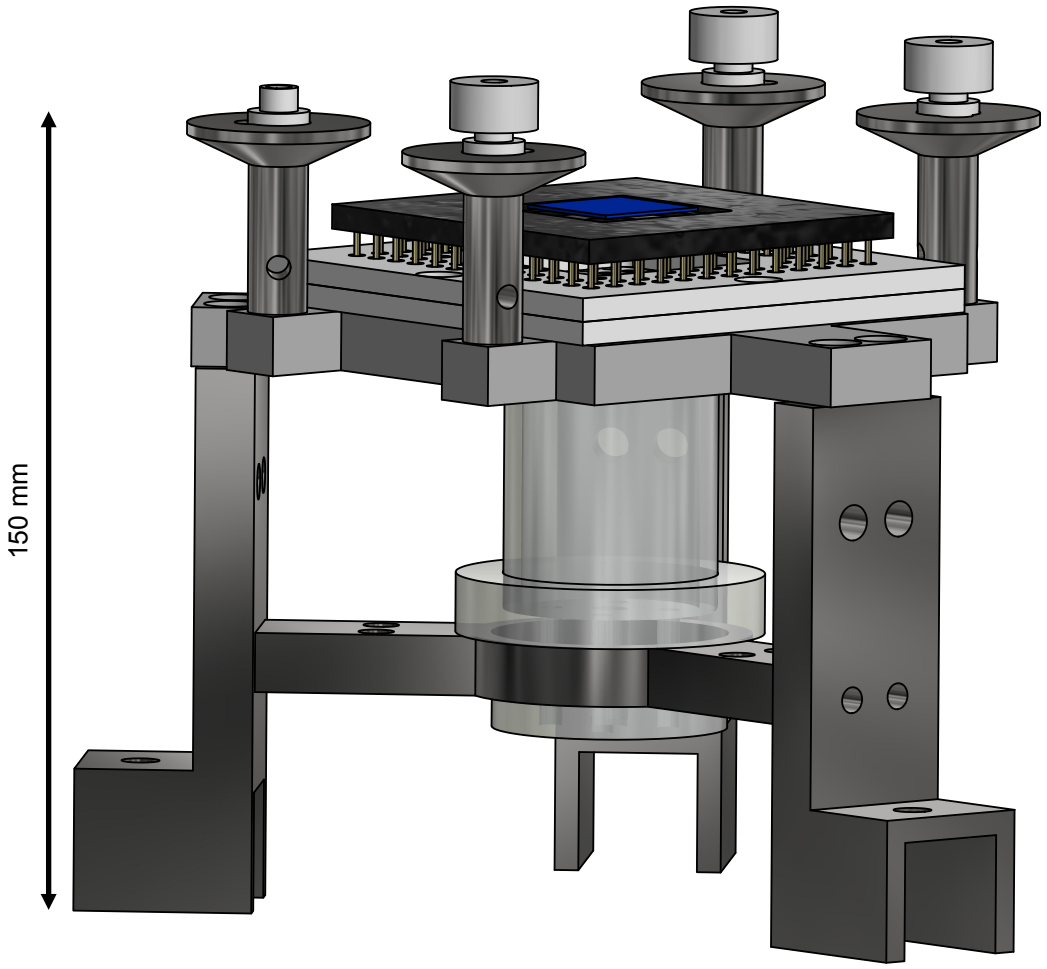

Figure 3.6: Chip carrier assembly which is mounted inside the vacuum chamber. Inside the glass tube (transparent cylinder in the centre) an oven assembly is mounted which allows back-side loading of the chip. The chip itself (blue) is fixed inside the chip carrier (black with golden pins) which is mounted in the socket. Four pillars carry a metal shield (not shown) above the chip, isolated by two ceramic washers per pillar (white, one not shown on the left). The overhanging architecture of the pillars blocks any line-of-sight between the trap chip centre and the isolating material.

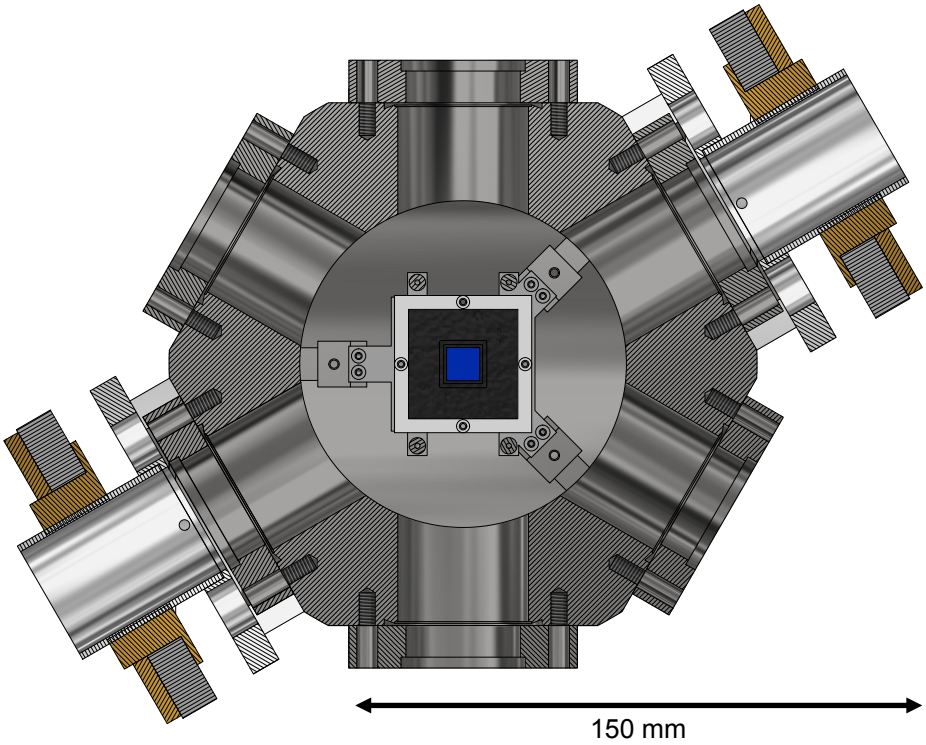

Figure 3.7: Cut-through view of the chamber in the chip plane. Six viewports allow optical access of the central chip (blue). On two opposing sides a solid-state magnet assembly is fixed where the magnets (darker grey) are mounted on brass assemblies (brass coloured).

3.3.2 Imaging optics

The imaging setup consists of all parts that allow us to image the ions to either a camera or a photo-multiplier tube. The setup was designed and assembled by Valentin Vierhub-Lorenz during his bachelors thesis and is described in Vierhub-Lorenz (2016). In Figure 3.8 we show an overview of the assembly. The imaging optics has to account

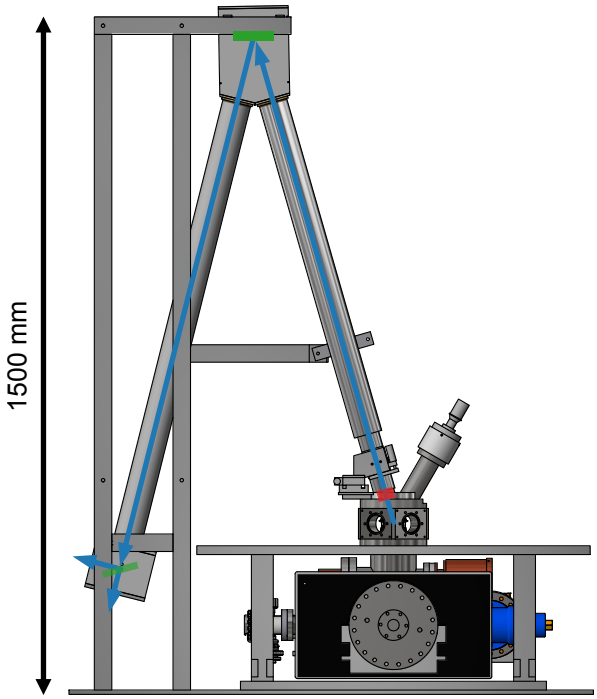

Figure 3.8: Sketch of the imaging optics and optical path (blue line). The ions fluorescence is collected by a three-lens objective (red). The light is reflected on a mirror on top (green, top) to the camera (bottom, not shown) or variably on a second flip-mirror (green, bottom left) and from there into the photo-multiplier tube (left).

for the angle of the viewport inside the top flange, leading to a symmetric v-shaped setup. Fluorescence light from trapped ions is collected by a three-lens objective[25] with an effective focal length of 57.3 mm at a design wavelength of 266 nm. The light is focused either on a camera or PMT, selected by an electronically controlled flip mirror. An optical band-pass filter[26] assembled before the flip-mirror reduces residual stray light from entering the camera or photo-multiplier tube. The setup offers a magnification by a factor of 41.1(2) as verified by imaging the trap surface onto the camera. All optics are coated with a high-reflective or anti-reflective coating (mirrors

[25] Sill Optics S6ASS2060/199
[26] Schott UG5

and objective respectively) suitable for wavelengths near 280 nm. Both the camera and the photo-multiplier tube are selected for their sensitivity at this wavelength.

3.3.3 Ablation loading

In the previously existing setup, we load ions by heating a magnesium wire in a custom oven design, followed by photo-ionisation in a two-photon process using a laser near 285 nm (Ströhle 2011). The oven is resistively heated using a current on the order of 2.7 A to a temperature on the order of 300 °C (Schaetz 2001).

An alternative to the oven is the evaporation of atoms by laser ablation. This method has been used in the context of ion traps for several decades (Hendricks et al. 2007; Knight 1981; Kwong et al. 1990; Leibrandt et al. 2007; Zimmermann et al. 2012). The idea is to use short, intense pulses generated by a pulsed laser to evaporate material from the surface of (in our case) a magnesium wire. The cloud of spattered atoms can be ionized at the trapping zone, the same way a ions stemming from an oven, to generate ions. Depending on the atom species and beam parameters (wavelength, intensity) the pulsed laser can also directly ionize the atoms.

The implementation and characterization of loading by laser ablation in our new setup was mainly performed by Leonard Nitzsche and is described in his masters thesis (Nitzsche 2017). We use a pulsed laser[27] with a wavelength of 532 nm producing pulses of (1.1–1.5) ns length with pulse-energies >50 µJ at a pulse rate of up to 1 kHz. We focus the beam onto a magnesium wire twisted around one of the four posts used to mount the shield above the trap chip. The use of a visible (532 nm) laser helps with adjusting the laser on the target where we choose a high pulse rate at low pulse energy and image the target using a camera. Note, this should also work with a laser in the infrared (1064 nm) as most cameras are sensitive in the infrared, after removing a potential infrared filter if needed. By integrating the laser control into our experimental setup, we are able to control (and automate) the whole loading process. During the calibration of the setup, we noted rises in the vacuum pressure when ablating that were not explained by the ablation process itself (which also causes a rise in pressure for larger intensities). We found a dependence of this effect on the amplitude of the radio-frequency trapping voltage. For typical amplitudes, we observed pressure rises, while for an amplitude reduced by about −3 dB there were no rises in pressure. This might be explained by arching between the radio-frequency electrode and close-by electrodes enabled by ionized magnesium atoms. To prevent this, we implemented a control circuit to reduce the trapping voltage while loading.

Our setup, and loading by laser ablation in general, offers several advantages over loading from an oven: Firstly, pulse lasers offer high repetition rates. With appropriately set intensity, loading durations can be *very* short, on the order of 1 ms (Bruzewicz et al. 2016). In our case loading times are essentially limited by the detection duration, e.g. the time needed to verify that one (or more as chosen) ion is loaded, given by the exposure and read-out time of the camera. The fast loading means

[27] Crylas FDSS 532-150-1k, (*Crylas FDSS532-150 Datasheet* 2013)

that the photo-ionization laser has to enter the chamber only for durations on the timescale of seconds, a time that could be reduced even further by a pulsed operation where the pulsed laser is operated synchronized with the photo-ionization laser. This means that potential electric charges produced by the photo-ionization laser near 285 nm can be reduced significantly compared to loading from the oven where our typical loading durations are on the order of (10–300) s, not accounting for the oven warm-up time of about 1 min. The short time-scales will also increase the duty-cycle for experiments running in larger arrays of trapped ions by faster reloading of single lost ions. Secondly, loading with the oven means a higher thermal load close to the trap. This can be crucial in cryogenic setups, but also at room temperature heating of the trap chip can lead to changes especially of electronic properties (capacitances, resistance), for instance of the radio-frequency circuit. Additionally, the current in the oven could lead to unwanted magnetic fields. A potential drawback for loading by laser ablation is that the mean energy of the atoms is larger compared to those released by an oven. This could limit the usability in traps with shallow trap depths but could be countervailed by adding designated loading-zones with larger trap-depths. Our setup could be improved by shielding the atom cloud to block atoms not flying towards the trap centre, as is done in similar setups (Hendricks et al. 2007).

3.3.4 Hybrid magnetic field assembly

In Section 2.2.2 we describe the concept and benefits of a magnetic-field-independent qubit. To realize this qubit for $^{25}Mg^{+}$ requires a magnetic quantization field of about 10.9 mT. In most ion-trap setups, but also in atom traps, magnetic fields are generated by solenoids. There, high currents are needed to reach strong magnetic fields resulting in large thermal loads. Therefore, the solenoids often need to be water-cooled. An advantage of coils is the ability to control the magnetic field over a large range or turn it off completely. This is used in atom traps, but in ion-traps the quantization field is almost always kept constant, except for fine-tuning to compensate for varying stray fields. Permanent magnets, on the other hand, offer the ability to generate a static quantization field without requiring any energy. Especially rare-earth magnets allow to reach strong magnetic fields.

In our setup, sketched in Figure 3.9, we use a hybrid approach to the magnetic field setup, combining strong rare-earth magnets with solenoids offering tunability of the magnetic field. To generate the quantization field at $|\boldsymbol{B}_0| \approx 10.9\,\mathrm{mT}$ along $\hat{\boldsymbol{z}}$, we employ commercially available neodymium ring magnets, magnetized in axial direction. Each ring has a thickness of 4 mm, 58 mm inner and 102 mm outer diameter. The distributor rates the magnetisation as N35 corresponding to a remanence of $B_\mathrm{r} \approx 1.17\,\mathrm{T}$ and a temperature coefficient of $(\partial B/\partial T)/B \approx -1.2 \times 10^{-3}\,\mathrm{K}^{-1}$. We use three rings each to form two sets of magnets. We mount each set (red in Figure 3.9 on opposing sites of the hexagon on a threaded mount that allows to manually translate the magnets along the magnetic field axis to tune the magnetic field strength at the trapping site. The two sets generate the quantization of approximately 10.9 mT. To

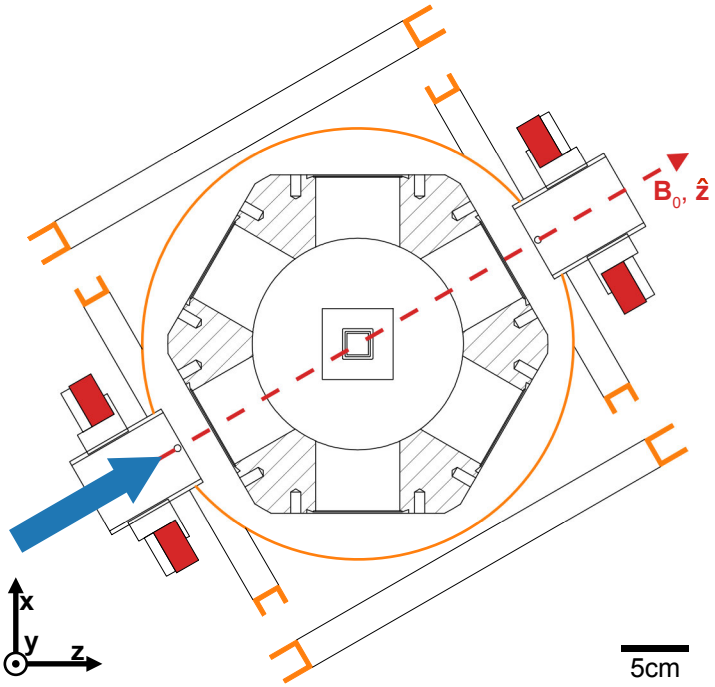

Figure 3.9: Sketch of the hybrid system setup around the vacuum chamber generating the magnetic field. The quantization field $\boldsymbol{B}_0$ along $\hat{\boldsymbol{z}}$ is generated by two sold-state magnet assemblies (red). Three coil pairs (orange) allow fine tuning of the quantization field and the compensation of external magnetic fields. The preparation and detection lasers propagate along $\hat{\boldsymbol{z}}$ (blue arrow). Figure adapted from Hakelberg et al. (2018).

calculate the magnetic field strength, we use the formula for the magnetic field of one ring (Peng et al. 2004):

$$B_{\mathrm{ring}}(\hat{z}) = \frac{B_r}{2}\left[\left(\frac{\hat{z}}{\sqrt{R_{\mathrm{o}}^2+\hat{z}^2}} - \frac{\hat{z}-D}{\sqrt{R_{\mathrm{o}}^2+(\hat{z}-D)^2}}\right) - \left(\frac{\hat{z}}{\sqrt{R_{\mathrm{i}}^2+\hat{z}^2}} - \frac{\hat{z}-D}{\sqrt{R_{\mathrm{i}}^2+(\hat{z}-D)^2}}\right)\right] \tag{3.1}$$

with inner R_{i} and outer R_{o} radius, and thickness D. In Figure 3.10 we plot the calculated magnetic field strength along $\hat{\boldsymbol{z}}$ for both stacks, using a superposition of Equation 3.1. On the left-hand side of Figure 3.10 we show a broad range, including the magnets in red. As the distance between the magnets of approximately 223 mm is large compared to the diameter, we do not have a classical Helmholtz type configuration, but a minimum of magnetic field strength in the centre. Along the central region (right in Figure 3.10) the magnetic field reaches the target value of approximately 10.9 mT. Using the Radia software package (Chubar et al. 1998; Elleaume et al. 1998) we simulate the magnetic field of the solid-state magnets. In a spherical volume with

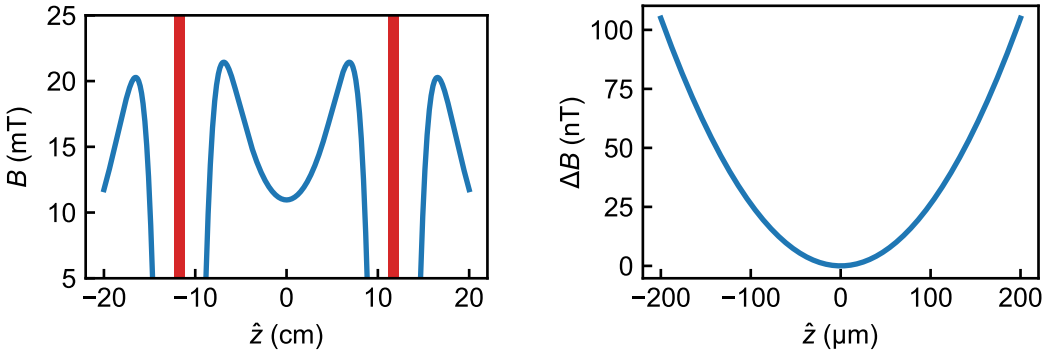

Figure 3.10: Calculated magnetic field strength generated by the permanent magnets. Left: Overview of the magnetic field strength along the quantization axis generated by the permanent magnets (positions indicated in red). At the trap centre at $\hat{\boldsymbol{z}} = 0$ the magnetic field strength is $B \approx 10.9\,\mathrm{mT}$. Right: deviations of the magnetic field strength around the calculated trap centre on the scale of a few 100 nm. Figure adapted from Hakelberg et al. (2018).

diameter $d_{\mathrm{dsv}} = 150\,\mu\mathrm{m}$, the calculated relative magnetic field strength varies by less than 1×10^{-6}. Rotating the magnet sets on the threaded mounts displaces them by 1 mm per rotation and allows to tune the magnetic field by $0.11\,\mathrm{mT\,mm^{-1}}$. We use this to coarsely tune the magnetic field strength.

To allow fine-tuning of the magnetic field, as well as compensation of fields perpendicular to the quantization axis, we employ three pairs of perpendicular coils (orange outlines in Figure 3.9). We use copper wire with a diameter of 1 mm with a polyurethane coating for isolation [28]. The first pair consists of two circular coils with 60 turns each generating a magnetic field of $0.26\,\mathrm{mT\,A^{-1}}$ along $\hat{\boldsymbol{z}}$. They allow fine-tuning of the quantization magnetic field. The second pair, also in the $\boldsymbol{x}$-$\boldsymbol{z}$-plane, but perpendicular to $\hat{\boldsymbol{z}}$ consists of two rectangular coils with 100 turns each. They generate a magnetic field of $0.24\,\mathrm{mT\,A^{-1}}$. The third pair, consisting of two circular coils with 120 turns each, allows to tune the magnetic field along $\boldsymbol{y}$ with $1.3\,\mathrm{mT\,A^{-1}}$. The latter two pairs, both creating magnetic fields perpendicular to $\hat{\boldsymbol{z}}$ allow to compensate for stray magnetic fields to ensure $\boldsymbol{B}_0 \parallel \hat{\boldsymbol{z}}$, i.e. that the magnetic field is oriented along the desired quantization axis $\hat{\boldsymbol{z}}$. To drive the coils, we use current-stabilized low-power supplies[29] specified with a stability of $0.2 \times 10^{-6}\,\mathrm{A}$ and a maximum current of 0.1 A. As we generate the main magnetic field using the permanent magnets, we can use power-supplies for low current which, for a given relative stability, leads to a higher absolute stability.

[28] Sauter Transformatoren: Kupferlackdraht 1,000 mm V180 Grad 1
[29] Thorlabs LDC 201 CU

3.4 The new apparatus - Characterization

In the new chamber we reached a vacuum pressure of 1.3×10^{-11} mbar. We trapped ions with storage times of typically 8 h and up to 20 h (while Doppler cooling). Furthermore, we performed first ground-state cooling experiments and heating rate measurements, which are not part of this thesis. We used this to measure the motional heating rate in the trap, which we found to be 2(1) quanta/ms on the axial motional mode at $2\pi \times 1.979(5)$ MHz.

In this Section, we present first measurements using the hybrid magnetic field setup in the new apparatus. We first describe the calibration procedure of the magnetic field, followed by coherence measurements to characterize the field-independent qubit. As a first application, we measure an oscillating magnetic field of small amplitude originating from stray currents in the radio-frequency electrodes. We published these results in Hakelberg et al. (2018). For all measurements described below, we prepare the ion in state $|3,3\rangle$ ($= |\mathrm{S}_{1/2}, \mathrm{F}=3, \mathrm{m_F}=3\rangle$) using optical pumping. We drive transitions using resonant microwave radiation. In particular, we use microwave transitions to prepare initial states of a selected transition, for example, $|3,3\rangle \rightarrow |2,2\rangle \rightarrow |3,1\rangle$ to prepare the initial state of the field-insensitive MW_2 transition (transition labels follow Figure 2.3 and Table 3.2). For detection, we reverse the preparation sequence of the initial state followed by detection of $|3,3\rangle$ using resonant fluorescence (see Section 2.2.3).

3.4.1 Magnetic field tuning and stabilization

During the initial setup we adjust the position of the permanent magnets to coarsely set the magnetic field strength, followed by fine-tuning using the electric coils. We utilize the magnetic field-sensitive transition, MW_0, to measure the magnetic field strength at the location of the ion. From numerical calculations (Kalis 2017), we derive the desired magnetic field strength at the field-independent point of the MW_2 transition, $|\boldsymbol{B}_0| \approx 10.9\,\mathrm{mT}$ (cf. Section 2.2.2). We then calculate the corresponding transition frequency of the field-sensitive transition MW_0, $\omega_{\mathrm{MW}_0}/(2\pi) \approx 1541\,\mathrm{MHz}$. This allows us to use frequency measurements of MW_0 as a reference to set $|\boldsymbol{B}_0|$ to the desired strength.

In a first measurement, we vary the position of the permanent magnets by rotating their threaded mounts, tuning the distance between the two magnets. For several settings, we measure ω_{MW_0} and ω_{MW_2} using Rabi experiments (see Section 2.1.1). From ω_{MW_0}, we calculate the magnetic field strength $|\boldsymbol{B}_0|$. In Figure 3.11 we plot deviations $\Delta\omega_{\mathrm{MW}_2}$ from the calculated magnetic-field insensitive transition frequency as a function of deviations from the corresponding magnetic field strength $\Delta\mathrm{B}_0$. The data follows the quadratic dependence $\Delta\omega_{\mathrm{MW}_2} \propto (\Delta\mathrm{B}_0)^2$. In the experiment, a rotating one permanent magnet holder by 360° moves the magnet by 1 mm and leads to a change of the magnetic field strength of about 0.11 mT.

To fine tune the magnetic field, we employ the electrical coils. We use the parallel coil pair (with respect to the quantization axis of the permanent magnets) to fine tune the magnetic field strength to the desired value and the two orthogonal coil pairs

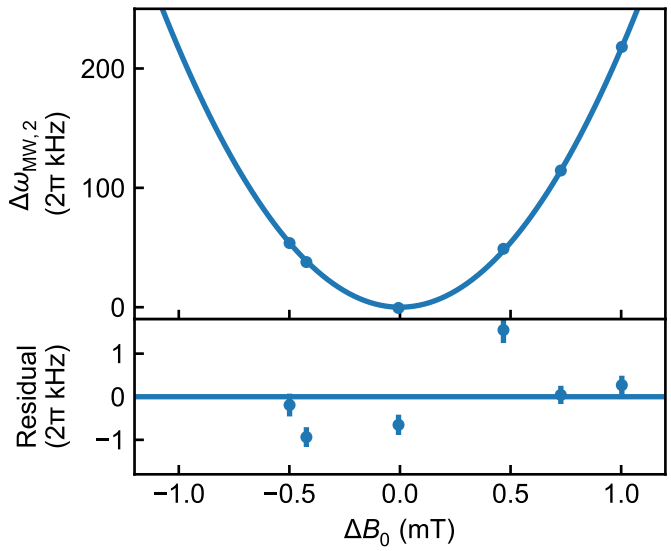

Figure 3.11: To coarsely tune the magnetic field strength, we displace the magnets along the quantization axis. For each position we measure the magnetic-field sensitive transition $|3,3\rangle \leftrightarrow |2,2\rangle$ and from this calculate the magnetic field strength. We measure the frequency of the field-insensitive transition $|3,1\rangle \leftrightarrow |2,0\rangle$ and plot deviations from the calculated field-insensitive point at $B_0 = 10.9\,\mathrm{mT}$. Error bars (SEM) are partially smaller than the marker size. Figure adapted from Hakelberg et al. (2018).

to compensate for external magnetic fields. For the later we measure the absolute magnetic field strength $|\boldsymbol{B}_0|$ as a function of the current in the coils using Rabi experiments on the MW_0 transition. For both coils, we choose the current where $|\boldsymbol{B}_0|$ is minimal. This corresponds to the point where the magnetic field component along this (orthogonal) direction is minimal. During our measurements, this corresponded to an electric current in agreement with zero. We, therefore, disconnect the orthogonal coil pairs from the power supplies and shorted them to minimize noise from current amplitude fluctuations. We then tune the parallel coil pare to set $|\boldsymbol{B}_0|$ to the desired value. To estimate the passive stability of the magnetic field we perform long-term measurements of $|\boldsymbol{B}_0|$ for the course of several hours. Maximal relative variations are below 0.3×10^{-4} within five minutes and 1×10^{-4} within one hour. We attribute this to slow drifts in the temperature in our laboratory space on the order of $\pm 0.1\,^{\circ}\mathrm{C}$, which is in agreement with the relative temperature stability of the solid-state magnets of $(\partial B/\partial T)/B \approx -1.2 \times 10^{-3}\,\mathrm{K}^{-1}$. During experiments, we recalibrate the current through the parallel coil pair regularly to keep track of these changes, typically on the order of every five to 20 minutes.

3.4.2 Coherence timescales

An important property of the system is the short-term coherence as a limiting factor to envisioned experiments. To characterize the system performance on typical experimental timescales we perform Ramsey experiments on the relevant transitions (see Section 2.2.4. We repeat the measurement several 100 times for fixed settings and repeat measurements for variable phase relation $\Delta\phi$ between the two pulses. In Figure 3.12 we show exemplary results of measurements of the MW_0, $|3,3\rangle \leftrightarrow |2,2\rangle$ transition for two settings $T_{\mathrm{Ramsey}} = 50\,\mu\mathrm{s}$ (blue data points) and $T_{\mathrm{Ramsey}} = 400\,\mu\mathrm{s}$ (orange data points). In the first case, the data is described by a sine function with an amplitude (contrast) of $92(2)\,\%$ only limited by preparation and detection, meaning that the system evolves coherently. In the second case, the contrast is $49(3)\,\%$. The shift in the phase of the two sine functions does not limit experiments. It is a result of a residual detuning of the two pulses compared to the transition frequency and could be compensated by calibration experiments. To determine the coherence timescale,

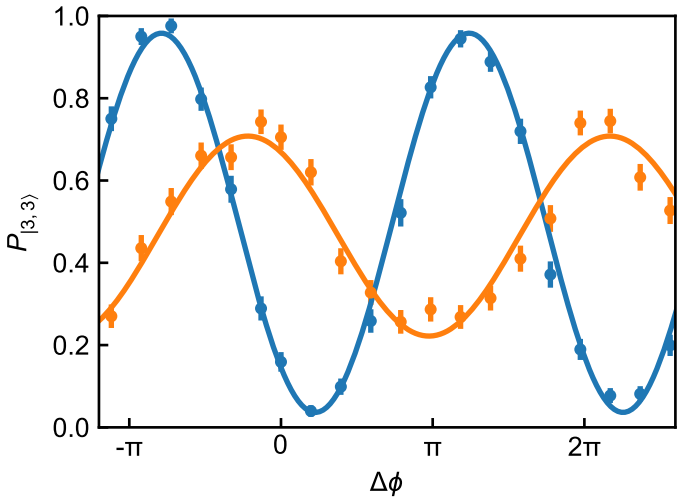

Figure 3.12: Exemplary Ramsey phase scans used to determine the coherence timescale of the $|3,3\rangle \leftrightarrow |2,2\rangle$ transition for variable free-evolution durations $T_{\mathrm{Ramsey}} = 50\,\mu\mathrm{s}$ (blue data points) and $400\,\mu\mathrm{s}$ (orange data points). We fit the data with a sine function with variable phase, amplitude and offset (solid lines). The amplitudes as a function of the T_{Ramsey} are then used to derive the coherence timescale. Error bars indicate the SEM.

we repeat these experiments for several T_{Ramsey} and determine the contrast. For each dataset, we normalize the contrast to the initial value at $T_{\mathrm{Ramsey}} = 0$ to get the normalized contrast C_{norm}. In Figure 3.13 we plot the resulting data for selected transitions. We fit each dataset with an exponential decay model:

$$C_{\mathrm{norm}}\left(T_{\mathrm{Ramsey}}\right) = \exp\left[-\left(\frac{T_{\mathrm{Ramsey}}}{\tau}\right)^2\right]$$

Here τ is the coherence timescale. We summarize the results in Table 3.2. As

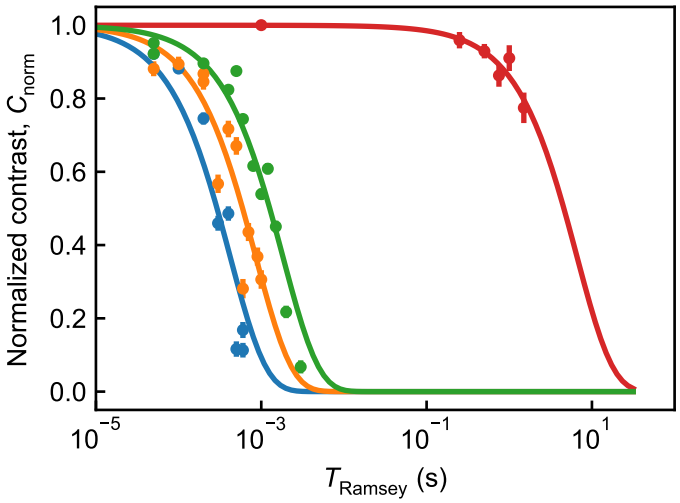

Figure 3.13: Measured normalized Ramsey phase scan contrast for four transitions. For four transitions we perform Ramsey experiments with variable phase for several waiting durations T_{Ramsey}. We fit the normalized contrast as a function of T_{Ramsey} with an exponential decay and extract coherence times, e.g. the time for which the normalized contrast drops to $1/e$. We find $\tau_{\mathrm{MW},0} = 0.42(6)\,\mathrm{ms}$ (blue, $|3,3\rangle \leftrightarrow |2,2\rangle$), $\tau_{\mathrm{MW},1} = 0.9(1)\,\mathrm{ms}$ (orange, $|2,2\rangle \leftrightarrow |3,1\rangle$), $\tau_{\mathrm{RF},0} = 1.8(2)\,\mathrm{ms}$ (green, $|2,2\rangle \leftrightarrow |2,1\rangle$), and for the field-insensitive transition $\tau_{\mathrm{MW},2} = 6600(9)\,\mathrm{ms}$ (red, $|3,1\rangle \leftrightarrow |2,0\rangle$). Error bars indicate the SEM. Figure adapted from Hakelberg et al. (2018).

expected the field-sensitive transition MW_0 exhibits the shortest coherence timescale of $\tau_0 = 0.42(6)\,\mathrm{ms}$. For the field-independent transition MW_2, we measure a coherence timescale of $6.6(9)\,\mathrm{s}$.

Label	Transition	Trans. frequency ω (2π MHz)	Field sensitivity $\partial\omega/\partial B$ (2π MHz mT^{-1})	Cpl. Str. Ω_{Coupl} (2π kHz)	Coherence time τ (ms)
MW_0	$\lvert 3,3\rangle \leftrightarrow \lvert 2,2\rangle$	1541.066(4)	-21.764	161(3)	0.42(6)
MW_1	$\lvert 2,2\rangle \leftrightarrow \lvert 3,1\rangle$	1655.815(2)	-10.116	38.3(8)	0.9(1)
MW_2	$\lvert 3,1\rangle \leftrightarrow \lvert 2,0\rangle$	1762.973 811 60(1)	$\pm 0(1) \times 10^{-4} (+0.434\,\mathrm{mT}^{-1})$	28.5(6)	6600(900)
RF_0	$\lvert 2,2\rangle \leftrightarrow \lvert 2,1\rangle$	55.260(1)	$+5.381$	0.28(6)	1.8(2)

Table 3.2: Summary of the results of the achieved coherence time scales for the transitions investigated in our system (see text). We give the labels used in this work and the relevant states of the transitions. For the magnetic field corresponding to the field-independent transition we numerically calculate the transition frequencies and field sensitivities, i.e. the derivative of the transition frequency with respect to the magnetic field amplitude. We show coupling strengths Ω_{Coupl} achieved with our setup and the measured coherence times τ. Table adapted from Hakelberg et al. (2018).

3.4.3 Sensing of oscillating magnetic fields

As a first application of our system, we use the field-independent transition as a highly stable quantum sensor for oscillating magnetic fields. Stray currents in the radio-frequency electrodes of the trap generate a magnetic field B_{osc} at the ions position oscillating at $\Omega_{\mathrm{RF}}/(2\pi) \approx 57.3\,\mathrm{MHz}$ and proportional to the radio-frequency voltage U_{RF}. Due to the long radio-frequency electrodes along the $\boldsymbol{z}$ direction we assume that the magnetic field vectors lie in the $\boldsymbol{x}$-$\boldsymbol{y}$-plane. From this orientation and the frequency of the oscillating field, we calculate a sensitivity $4.783\,\mathrm{Hz}\,\mu\mathrm{T}^{-2}$ of the field-independent transition due to the a.c. Zeeman shift (Warring et al. 2013a). As we assume that the magnetic field is generated by stray currents inside the radio-frequency rails we expect a linear scaling of the magnetic field amplitude with the radio frequency voltage. To characterize this magnetic field, we want to perform two measurements: Firstly the dependence on U_{RF} to allow estimations of the magnitude of B_{osc} and secondly the spatial variation along the $\boldsymbol{y}$ direction. In our setup, we cannot directly measure the radio-frequency voltage at the electrodes. We instead use simulations of the trapping potential Φ_{RF} (cf. Section 2.3.2) to calculate U_{RF}. As described in Section 2.3.1 the sum of the squared motional frequencies is independent of all static control potentials and given by Φ_{RF}. This allows us to calculate U_{RF} from measurements of all three motional frequencies. An essential parameter here is the ions position in the trapping field. We, therefore, compensate the ion for excess micromotion in the $\boldsymbol{x}$-$\boldsymbol{y}$-plane, and use this position in the simulation. For typical trapping conditions, we estimate $U_{\mathrm{RF}} \approx 79.5\,\mathrm{V}$. As a calibration measurement, we track the motional frequencies and thereby U_{RF} for variable driving power of the radio-frequency setup.

In the second experiment, we want to investigate the spatial dependence of the magnetic field, more precisely along the $\boldsymbol{y}$ direction. For this, we displace the ion along $\boldsymbol{y}$ using a control potential. Again, we use measurements of the motional

frequencies to, in combination with the trap simulations, infer the position of the ion in the trapping potential. Here we utilize the fact that in our trap the sum of squared eigenfrequencies varies with the distance to the trap electrodes, the $\boldsymbol{y}$ position[30]. We estimate the uncertainty of the relative ion-position change along $\boldsymbol{y}$ to be within $\pm 0.2\,\mu\text{m}$ and by tracking the position of the ion with the camera ensure that displacements perpendicular to $\boldsymbol{y}$ are smaller than $\pm 1\,\mu\text{m}$.

For both measurements, we employ a spin-echo sequence (see Section 2.2.4) on the field-insensitive transition MW_2 ($|3,1\rangle \leftrightarrow |2,0\rangle$). After preparation of the $|3,1\rangle$ state, we prepare a superposition of $|3,1\rangle$ and $|2,0\rangle$ using a $\pi/2$-pulse. After a first free-evolution period with duration T_{FE}, we employ a π-pulse, in phase with the first pulse, followed by a second free-evolution period and a final $\pi/2$ pulse. During the second T_{FE} we vary the parameter of interest, meaning U_{RF} or the ions position. We perform the spin-echo experiment for variable free-evolution durations T_{FE}. Deviations and a residual detuning of the pulses that are present during both free-evolution periods are cancelled out by the central π pulse, while effects from the varied parameter are only present in the second period. This means that a frequency difference $\Delta\omega_{\text{MW},2}$ is accumulated during the second T_{FE}. Therefore, the data exhibits oscillations as a function of T_{FE} with this frequency $\Delta\omega_{\text{MW},2}$.

Radio-frequency voltage dependence

To estimate the amplitude of B_{osc}, in a first measurement, we measure the dependence on U_{RF}. For this, we perform a spin-echo experiment on the field-insensitive transition where during the second free-evolution period we vary U_{RF} by ΔU_{RF} (see Figure 3.14, top). After the central π-pulse we ramp U_{RF} by ΔU_{RF} within $80\,\mu\text{s}$, and back before the last $\pi/2$-pulse. We repeat this measurement for variable ΔU_{RF} scanning T_{FE} up to $1.2\,\text{s}$ and extract the frequency differences. The resulting data is plotted in Figure 3.14 (bottom). From the sensitivity on the oscillating magnetic field given above and the assumed linear dependence of the magnetic field amplitude on the radio-frequency voltage, we expect a $\Delta\omega_{\text{MW},2} \propto {U_{\text{RF}}}^2$ dependence. From a squared model fit we find a slope of $2\pi \times 20.77(7)\,\text{mHz}\,\text{V}^{-2}$. In Figure 3.14 we plot the measured deviations from the transition frequency at $U_{\text{RF}} = 79.5\,\text{V}$. By extrapolating to $U_{\text{RF}} = 0\,\text{V}$ ($\Delta U_{\text{RF}} = -U_{\text{RF}}$) and from the sensitivity of the transition stated above, assuming that B_{osc} originates purely from the radio-frequency electrode, i.e $B_{\text{osc}}|_{U_{\text{RF}}=0} = 0$, we calculate $B_{\text{osc}}|_{U_{\text{RF}}=79.5\,\text{V}} = 5.239(8)\,\mu\text{T}$.

[30] This is the case for *most* surface-electrode traps where the density of field lines increases closer to the electrodes and vanishes for large distances.

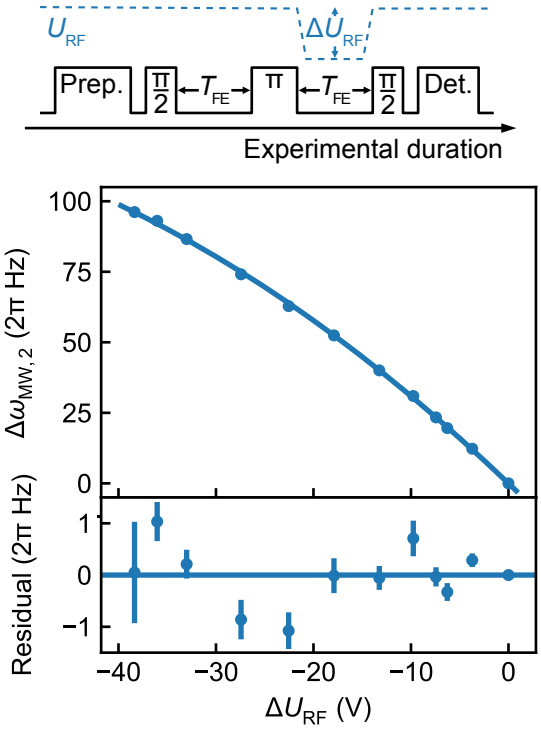

Figure 3.14: Sensing of the dependence of the magnetic field on the radio-frequency voltage. The sequence is based on spin-echo experiments with two free-evolution periods of variable duration T_{FE} framed by $\pi/2$-pulses and separated by a π-pulse (top). In the first experiment (left) during the second free-evolution time we vary the radio-frequency voltage amplitude U_{RF}. From oscillations in the spin-echo experiments we fit the frequency shift of the field insensitive transition $\Delta\omega_{MW,2}$ (blue data points, left). We fit the data with a squared model and find a slope of $2\pi \times 20.77(7)\,\mathrm{mHz\,V^{-2}}$ (fit residuals below). Here, we plot the measured deviations from the transition frequency at $U_{RF} = 79.5\,\mathrm{V}$. From this we calculate an oscillating magnetic field strength of $B_{osc} = 5.239(8)\,\mu\mathrm{T}$ for the default setting ($\Delta U_{RF} = 79.5\,\mathrm{V}$). Error bars (SEM) are plotted, partially smaller than the marker size. We attribute residual deviations from the model to uncertainties in the measurement of ΔU_{RF}. Figure adapted from Hakelberg et al. (2018).

Spatial dependence

In the second experiment, we measure the spatial variation dependence of B_{osc} along the $\boldsymbol{y}$ direction, perpendicular to the trap chip. As for the U_{RF} dependence, we employ a spin-echo sequence and during the second T_{FE} we displace the ion by Δy along $\boldsymbol{y}$ up to approximately 10 µm (see Figure 3.15, top). We ramp between the configurations within 400 µs and implement a corresponding additional waiting duration in the first half of the sequence. This ramping duration is short compared to T_{FE} of up to 1.2 s. The resulting data follows a linear function $\Delta\omega_{\mathrm{MW},2} \propto \Delta y$ with a slope of $2\pi \times 327(7)\,\mathrm{mHz\,\mu m^{-1}}$. From $\Delta\omega_{\mathrm{MW},2}$ and the sensitivity of the transition on B_{osc}, we calculate the variation ΔB_{osc} and plot this as a function of Δy (see Figure 3.15, bottom). We model the data using a square-root dependence $\Delta B_{\mathrm{osc}} \propto \sqrt{|\Delta y|}$ and find a non-linear slope of $\Delta B_{\mathrm{osc}} = 0.261(3)\,\mathrm{\mu T\,\mu m^{-1/2}}$.

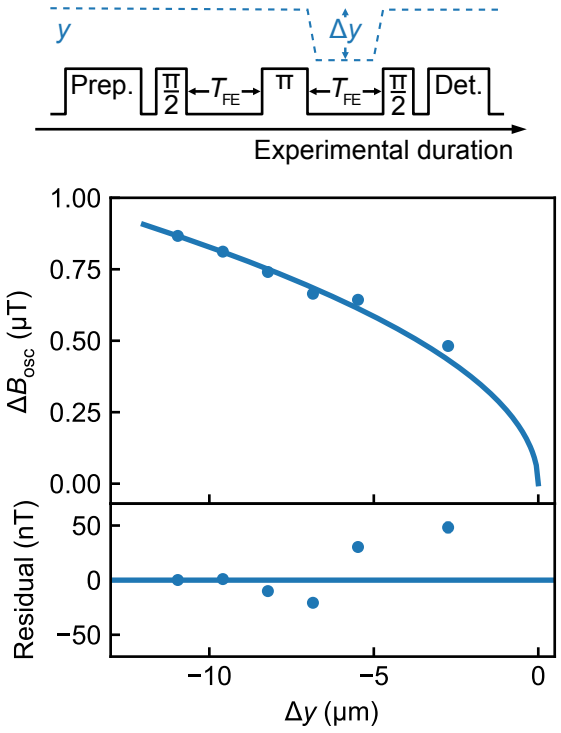

Figure 3.15: Sensing of the spatial dependence of the oscillating magnetic field. During the second free-evolution period, we vary the position of the ion orthogonal to the trap chip to measure the spatial dependence of the oscillating magnetic field. From the data, analog to the previous experiment, we derive changes in the magnetic field strength ΔB_{osc} (blue data points, right). We fit the data using a square-root function and find $\Delta B_{\mathrm{osc}}/\sqrt{|\Delta y|} = 0.262(3)\,\mathrm{\mu T\,\mu m^{-1/2}}$ (fit residuals below). Error bars (SEM) are smaller than the marker size. We attribute residual deviations from the model to uncertainties in the calculation of Δy. Figure adapted from Hakelberg et al. (2018).

3.4.4 Discussion

We realize a hybrid system to generate a magnetic quantization field that allows us to realize a first-order magnetic-field independent qubit in $^{25}Mg^{+}$. Using electrical coils for residual compensations we can stabilize the magnetic field to a field-sensitive reference transition by which we realize a relative stability of better than 2×10^{-5}. We characterize the decoherence rate of the field-independent qubit and find a coherence time of 6.6(9) s. We attribute the limitations to residual fluctuations of the magnetic field and decoherence induced by scattering of leaked laser light where a single absorbed photon destroys the superposition state (Clos et al. 2014). Stable qubits will be an essential ingredient in future quantum simulation and quantum computing applications.

We use this stable qubit as a probe of oscillating magnetic fields induced by stray currents in the radio-frequency electrodes of the trap. This is a first step towards future quantum-sensing applications. Additionally, the approach using solid-state magnets significantly reduces the power requirements compared to electrical coils, which in turn removes the thermal load produced by such a system. This could open up operation in environments with rigorous constraints such as in space-borne applications. In the following, we summarize potential future improvements of the system based on our experience.

Future improvements

On *long* timescales of several minutes to hours the stability of our system is currently limited by drifts of the magnetic field that we attribute to thermal fluctuations. While the use of permanent magnets, compared to solenoids, helps to reduce the thermal load significantly, fluctuations in the surrounding temperature still affect the system. Those temperature fluctuations impact two-fold: Firstly, the negative reversal temperature coefficient of neodymium leads to a lower magnetic field for higher temperatures. Secondly, thermal expansion of the setup itself leads to an increased distance between the two permanent magnet assemblies, lowering the magnetic field at the position of the ion. The first could be compensated for by using temperature-compensated magnet alloys or assemblies combining different materials (Danieli et al. 2013). Basing the support structure of the magnet assembly on a material with a low coefficient of thermal expansion can reduce the latter effect. Additionally, one could combine both effects in a way that thermal expansion and magnetic temperature coefficient would cancel out each other. These changes would improve the passive stability of the system.

An additional possibility is to actively stabilize the system. One option is to measure the magnetic field using a dedicated sensor close to the trap and use the signal as a feedback for the coils. Here the stability of the sensor and the distance to the trap are limiting factors. Another option would be to directly use the ion as a sensor, as we routinely do for our calibration measurements (see Section 3.4.1). This could also be done using an additional ion, optionally of a different isotope or species, to allow sensing of the magnetic field in parallel to other experiments. Additionally to simply

increasing the rate of calibration measurements, one could implement a feed-forward control loop: By extrapolating from past measurements one can anticipate the time evolution of the magnetic field changes and apply corresponding, time-dependent, corrections. As a countermeasure to external magnetic fields, one could employ a shielding from nu-metal (Ruster et al. 2016).

On *short* time-scales, the field-insensitive transition already offers coherence times of more than 6 s. Filtering and stabilizing of the electronics supplying the coils, but also others in proximity to the trap, could be employed. Another decoherence mechanism is the scattering of laser radiation, destroying superposition states, already on the single-photon level (Clos et al. 2014). This can be influenced best by controlling the acousto-optic modulator (AOM) setup used to switch the beams. Firstly, the radio-frequency signal driving the AOM should be sufficiently suppressed when turned off by the experimental control. Secondly, leakage of light from different diffraction orders (typically the 0th order) in the AOM to the selected order (typically the 1st order) has to be suppressed. Here it is important that both beams are well separated. Double-pass configurations help to improve this as they can effectively square the isolation. Additionally, optical shutters could be employed, at a significant trade-off regarding switching times.

4 Results

In this Chapter, we present results achieved with the triangle trap array (see Section 2.3.3). All presented results concern the inter-site coupling in our array and were published in parts in Hakelberg et al. (2019). We demonstrate the first realization of Coulomb coupling between two ions trapped in distinct trapping sites in a two-dimensional array. We investigate the coherent exchange of *large* coherent states of motion between two sites including the effect of anharmonic contributions to the trapping potential, followed by the demonstration of real-time control of the exchange between multiple sites, and the global coupling of all three sites.

First, we explain the basic procedure to establish coherent inter-site coupling between two sites, including necessary calibration measurements. To investigate the effect of anharmonic contributions to the trapping potential on the coupling we perform measurements with variable initial excitation amplitudes. We use the real-time control of the coupling to demonstrate sequential, coherent coupling between multiple sites of the array. Finally, we couple all three sites of our array simultaneously to show the evolution of a single excitation and the interference of coherent states excited at two sites of the array.

For all presented experiments, we select at each site the motional mode with the lowest motional frequency as a coupling mode with frequency ω_{cpl}. We prepare coherent states of motion (see Section 2.1.2) and give their amplitudes ($\bar{n}$) in units of quanta, a quantity invariant under adiabatic changes of the motional frequencies.

4.1 Two-site coupling basics

The main result of this work is the realization of coherent inter-site coupling in our triangular ion array. In this Section, we will describe step by step the necessary experimental procedures to realize this coupling. For this, we will discuss the basic case of the coupling of two single ions, each trapped at one site of our array.

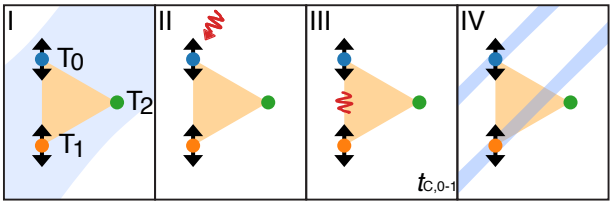

Figure 4.1: Experimental sequence to couple two sites, here T_0 and T_1. Throughout the experiment the coupling modes at T_0 and T_1 are oriented towards each other. After global preparation (I) using a global laser beam (blue shaded area), a coherent state is excited (red wiggly arrow) at site T_0 (II). The sites are then coupled (red wiggle) for a variable duration $t_{C,0-1}$ by tuning the motional modes into resonance (III), followed by local detection of sites T_0 and T_1 (IV) using a focused laser beam (blue shaded areas). Figure adapted from Hakelberg et al. (2019).

In Figure 4.1 we depict the complete experimental sequence used therefor, consisting of 4 essential steps:

I Preparation. All corresponding sites are cooled, here by Doppler cooling to low motional amplitude using a global beam addressing all sites simultaneously.

II Excitation. At one site, here T_0 a coherent state of motion is excited.

III Coupling. The two sites, here T_0 and T_1 are tuned to resonance to enable resonant coupling for a variable duration $t_{C,0-1}$.

IV Detection. At both sites, the motional state amplitude is detected. We use a laser beam focused to a single site and repeat the sequence for each measured site.

For a first proof-of-principle experiment of inter-site coupling, here between T_0 and T_1, we require control over several experimental parameters of the trapping sites, following the theoretical considerations in Section 2.5. At both sites, the mode orientations need to allow sufficient overlap with the cooling lasers to ensure efficient Doppler cooling (Section 2.4.1). At the same time, the coupling modes should be oriented collinear to ensure a maximized coupling rate (cf. Equation 2.37). We then need to prepare a defined motional state at one site while not affecting the second site (Section 2.4.2). To switch on the coupling, we control the frequency detuning between the two sites, tuning them into resonance for a defined duration. When changing the motional frequencies, e.g. to tune two sites into resonance, we ensure that we ramp

between frequencies on a timescale $t_{\mathrm{ramp}} > 2\pi/\omega_{\mathrm{cpl}}$, typically on the order of 20 µs for motional frequencies of $2\pi\times(3\text{–}5)$ MHz and fast compared to inverse coupling rates on the order of (250–1000) µs. For the whole experimental sequence, we choose a control potential where ideally the coupling modes are oriented along the connecting axis and an angle of 45° to the cooling and detection lasers. We analyse the motional-mode orientation following Section 2.4.4. For T_0 we find an in-plane rotation angle of $-2(2)°$ and an out-of-plane angle of $28(15)°$. For T_1 we find $2.0(2)°$ and $-25(15)°$ respectively. Additionally, we extract an inter-ion distance of 40.7(5) µm. In the harmonic approximation, this would alter the on-resonance coupling rate compared to a collinear mode orientation by a factor of 0.84(9). To control the frequency detuning between the two sites we employ a control potential calculated to tune the coupling mode at T_0, oriented along $\boldsymbol{x}$, while keeping T_1 constant. More precisely, at site T_0 the potential increases the curvature along $\boldsymbol{x}$ while decreasing the curvature along $\boldsymbol{y}$. In the following, we describe how we calibrate this control potential coarsely, for each site separately, and fine-tune it by directly observing the inter-site coupling.

4.1.1 Frequency calibration

In a first calibration measurement, we characterize the effect of the control potential separate for each site. For this, we employ coherent excitation frequency scans as described in Section 2.4.2. We load one ion at a selected site and measure the coupling-mode frequency for variable values of the control potential. We then repeat this measurement for an ion at the second site. In Figure 4.2, we exemplarily show the

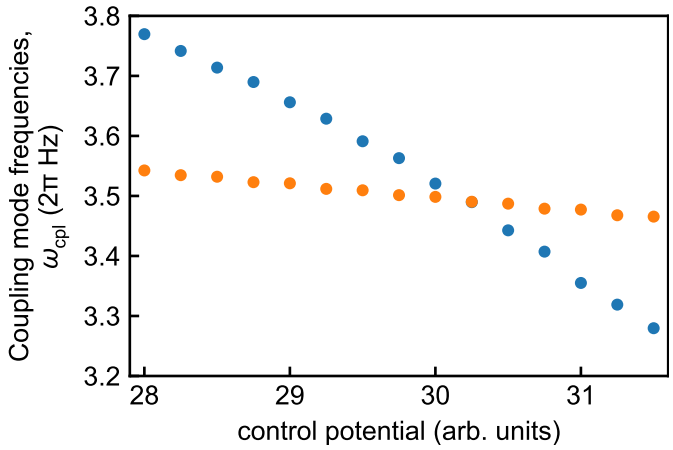

Figure 4.2: Exemplary calibration measurement of a frequency-tuning control potential. We measure the frequency of the coupling modes at sites T_0 and T_1 (blue and orange data points) as a function of a control potential calculated to tune the eigenfrequency at T_0. The control potential allows to tune the two sites into resonance, enabling the inter-site coupling. From linear fits we extract a crosstalk of 11.5(1) %. Error bars (SEM) are smaller than the marker size.

data of such a calibration measurement. Here we select a control potential tuning the

coupling mode at T_0 while, ideally, keeping the coupling mode at T_1 constant. From the data, we see that the control potential allows tuning along the coupling mode at T_0 while the crosstalk to T_1 is 11.5(1) %. We note that a residual crosstalk does not directly limit the experimental usability as long as the inter-site detuning can be tuned efficiently. However, bearing in mind the scaling to larger arrays, it is favourable to work with control potentials with low crosstalk, for instance, to not affect the coupling to other sites. By further optimizing control potentials for crosstalk we achieve values of better than 5 %.

We perform this calibration experiment each time we have to coarsely find the resonance condition, for instance after changing control potentials to tune the motional mode orientation. The experiment has the advantage that it is independent from the actual inter-site coupling and can be performed using only one ion.

4.1.2 Finding the resonance

Theoretically, the above frequency calibration should allow to directly set the resonance condition $\omega_0 = \omega_1$. However, as motional frequencies are not fixed, but drift on the order of several kHz, for example, when loading ions and due to the additional motional amplitude dependence of the motional frequencies in the anharmonic trapping potential, this is not feasible for actual experiments. We rather rely on the calibration as a coarse setting and the fine-tune by directly observing the coupling strength between the two sites. For this we perform a coupling experiment as described in Figure 4.1, for fixed coupling duration and variable settings of the control potential setting the inter-site detuning.

In Figure 4.3 we show exemplarily the results of such an experiment. Here, for control potential values around 29.85, during the coupling duration, motional excitation is exchanged from T_0 to T_1 leading to a measurable excitation at T_1. We then use this value for further coupling experiments. To keep track of residual drifts we repeat this calibration experiment interleaved with other measurements, typically every 2 to 5 minutes. For some control potentials, we found that the resolution when scanning for the resonance condition was limited by the finite step size of our DAC (0.3 mV). In this case, we use the control potential to set the frequencies close to resonance within a few $2\pi \times 1\,\mathrm{kHz}$ and then tune the voltage on a single electrode to fine-tune the frequency difference to resonance. Here we choose an electrode with a small impact on the motional frequencies when changing the voltage on the order of the finite step size.

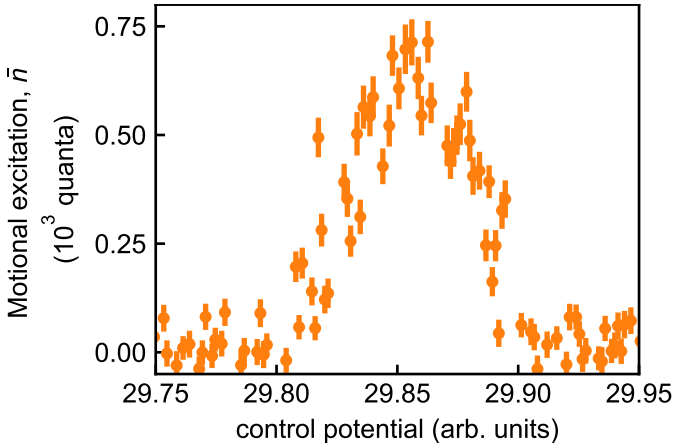

Figure 4.3: Exemplary scan used to find the resonance condition during coupling experiments. We initialize two ions, at sites T_0 and T_1 and excite a coherent state at T_0. Then, for a fixed duration $t_{C,0-1}$, we tune the motional frequency at T_1, using a dedicated control potential, to a value around the expected resonance condition. Finally, we detect motional excitation at T_1. The resulting data for variable values of the control potential (orange data points) show the resonance around 29.85 where motional excitation is transferred from T_0 to T_1. We then use this value for further coupling experiments. Error bars indicate the SEM.

4.1.3 Coherent coupling

To further investigate the coupling, we want to track the time evolution of the excitation between the two sites. In particular, this allows to ensure that we are coherently coupling the ions, where the initial excitation is exchanged back and forth between the sites. For this, after finding the resonance condition we employ the sequence depicted in Figure 4.1 and vary the coupling duration $t_{C,0-1}$. We repeat experiments for detection at both sites to track the evolution of the initial excitation in the system, see Figure 4.4. There we additionally plot deviations from the sum of total coherent excitation:

$$\Delta\bar{n}_{\mathrm{tot}}(t) = \bar{n}_{\mathrm{tot}}(t) - \langle\bar{n}_{\mathrm{tot}}\rangle$$

with

$$\bar{n}_{\mathrm{tot}}(t) = \sum_i \bar{n}_i(t),$$

the sum over the excitation in all relevant trapping sites, here $i \in \{0, 1\}$. This sum should be conserved, assuming there are no heating or cooling processes and all changes to motional frequencies are adiabatic. Here, the intrinsic motional heating rate of our trap, on the order of 10 quanta/ms is negligible compared to typical excitation amplitudes and experimental timescales. We model the time evolution by a sinusoidal model including a Gaussian decoherence term:

$$\bar{n}_{(0/1)}(t) = \bar{n}_{(0/1)}(0) \mp \frac{\mathrm{A}}{2}\left(1 - \cos\left(\Omega_{\mathrm{C,eff}} \cdot t\right) e^{-(t/\tau_{\mathrm{C,dec}})^2}\right) \tag{4.1}$$

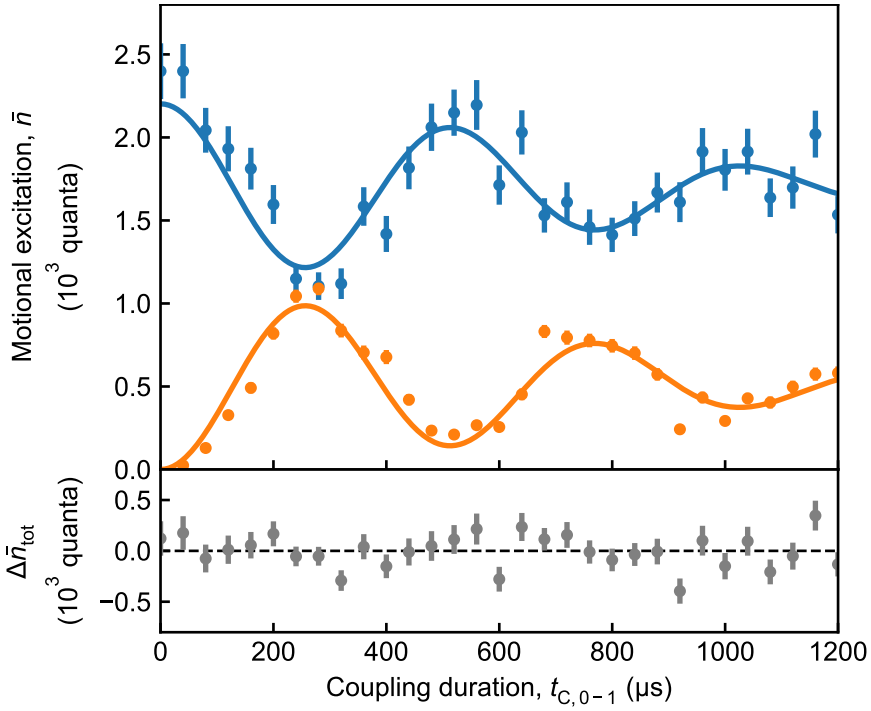

Figure 4.4: Experimental results of an inter-site coupling between T_0 and T_1. Initially a coherent state with approximately 2200 quanta is prepared at T_0 (blue data points). During $t_{C,0-1}$, approx. 1000 quanta are coherently transferred between T_0 and T_1 (orange data points) with a rate of $2\pi \times 2\,\mathrm{kHz}$. We plot deviations from the average total motional excitation at T_0 and T_1, $\Delta\bar{n}_{\mathrm{tot}}$ (grey data points) to emphasize the conservation of motional excitation in the system. Error bars (partially smaller than the marker size) indicate the SEM. Figure adapted from Hakelberg et al. (2019).

with the exchange amplitude A, the coupling rate $\Omega_{\mathrm{C,eff}}$, and decoherence timescale $\tau_{\mathrm{C,dec}}$. We fit the model to the data for T_0 and T_1 simultaneously, assuming constant total motional excitation, $\bar{n}_0(t) + \bar{n}_1(t) = \mathrm{const}$. Initially, we excite a coherent state with amplitude $\bar{n}_0 \approx 2202(57)$ quanta at T_0. During $t_{C,0-1}$ the excitation is coherently exchanged between the two sites with a rate of $\Omega_{\mathrm{C,eff}} = 1.92(2)\,\mathrm{kHz}$ and an efficiency of $\kappa = 46(2)\,\%$. The latter denotes the fraction of initial excitation that is transferred from T_0 to T_1. The oscillations are damped by a decoherence timescale of $\tau_{\mathrm{C,dec}} = 800(60)\,\mu\mathrm{s}$. For each site, we plot statistical uncertainties (SEM) calculated from 400 realisations per data point. The different relative uncertainties from T_0 and T_1 are caused by the individual motional state reconstruction. We observe residual scattering of the data points, compared to the fitted model, not explained by the plotted uncertainties, in particular visible for T_1. We attribute this to experimental variations, for example, of local motional eigenfrequencies, between data points. Within experimental uncertainties, the sum of excitations stays constant throughout the experiment, $\Delta\bar{n}_{\mathrm{tot}} \approx 0$ quanta. From the measured motional-mode orientations and

the on-resonance eigenfrequency of $2\pi\times3.56\,\mathrm{MHz}$ we calculate a theoretical exchange rate of $\Omega_{\mathrm{C,harm}} = 1.03(13)\,\mathrm{kHz}$, assuming coupled harmonic oscillators (see Section 2.5). Furthermore, in the picture of resonantly coupled harmonic oscillators, the exchange efficiency is 100 %. We see this effect of an increased coupling rate and decreased efficiency compared to the calculations for harmonic coupled oscillators in all coupling experiments in this trap. We attribute this to higher-order anharmonic contributions to the trapping potential, which lead to an amplitude dependence of the motional frequencies (see Section 2.4.4). In Section 2.5.1 we simulate this effect for a model system and find a qualitative agreement. In theory, a similar effect could be explained by a detuning between the two oscillators. We rule this out due to the reproducibility of the effect. In the following, Section we investigate this effect of the anharmonic contributions by measuring the coupling parameters for variable initial excitation.

4.2 Coupling with variable excitation amplitude - Anharmonic effects

In this Section, we investigate the effect of anharmonic contributions to the trapping potential on the inter-site coupling. In principle, we could use control potentials to partially tune the anharmonic contributions (limited by the number of control electrodes) and observe changes to the coupling parameters. However, we observe that tuning the anharmonic contributions also changes the eigenfrequencies, mode orientations and inter-site distance, which we attribute to discrepancies between the simulated and actual electrical potential and ion positions therein. To minimize the effect of these changes on the coupling we do not change the anharmonic contributions, but rather vary the excitation amplitude to change the sensitivity of the coupling to the anharmonic contributions. We again follow the coupling sequence depicted in Figure 4.1, coupling sites T_0 and T_1.

Calibration of the excitation strength

As a first measurement, we calibrate the initial excitation at T_0 (cf. Section 2.4.2). We excite the ion at T_0 with variable control amplitude, $U_{\mathrm{exc,ctrl}}$ and reconstruct the coherent state amplitude. Here, $U_{\mathrm{exc,ctrl}}$ is the amplitude of the sinusoidal excitation voltage we program for a single electrode. Due to filter effects, the actual amplitude at the electrode is attenuated as a function of the excitation frequency. We perform the excitation at resonance (approx. $2\pi \times 3.76\,\mathrm{MHz}$) and expect a linear relationship between $U_{\mathrm{exc,ctrl}}$ and the actual amplitude at the electrode and, therefore, the electric field amplitude at the ions position. The resulting data plotted in Figure 4.5, shows a quadratic dependence of the excited state on $U_{\mathrm{exc,ctrl}}$, as is expected from theory (see Section 2.4.2). From the motional frequency and excitation amplitude, we calculate the amplitude of the electric field exciting the motion $22.863(1)\,\mathrm{V/m/V_{exc,ctrl}}$. This is the component of the oscillating electric field parallel to the motional mode orientation, as a function of the control voltage amplitude. We here vary the initial excitation in the range of (200–7000) quanta.

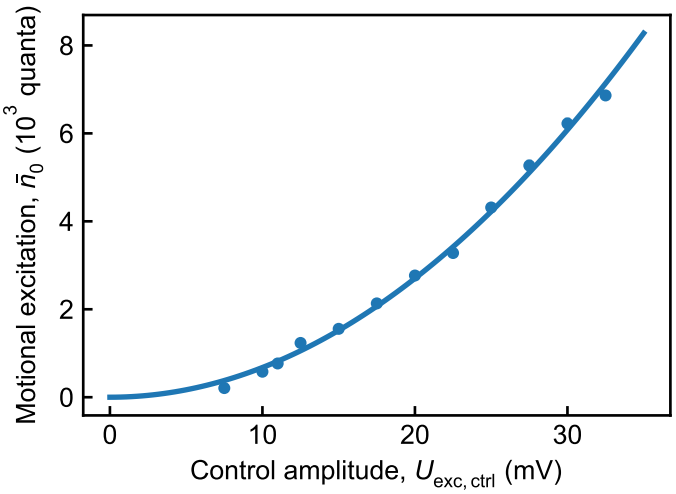

Figure 4.5: To calibrate the preparation of coherent states we excite at site T_0 with variable control amplitude $U_{\mathrm{exc,ctrl}}$ for constant duration $t_{\mathrm{exc}} = 20\,\mu\mathrm{s}$. We fit the detected motional state amplitudes (blue data points) by a squared function $\bar{n}_0 \propto U^2_{\mathrm{exc,ctrl}}$. We extract an effective electrical field amplitude of $22.863(1)\,\mathrm{V/m/V_{exc,ctrl}}$. Error bars (SEM) are smaller than the marker size.

Coupling experiments

To investigate the effect of variable initial excitation on the coupling we perform the following experiments: For a given excitation at T_0 we find the resonance condition as described in Section 4.1.2 followed by a coupling sequence where we track the excitation at T_1 for variable coupling durations. We fit the results of the latter experiment using a sine function with decoherence term (Equation 4.1) and extract oscillation amplitudes and frequencies.

First, we investigate the maximal excitation $\bar{n}_{1,\mathrm{max}}$ at T_1 that is reached during the coupling as a function of the initial excitation $\bar{n}_{0,\mathrm{i}}$ at T_0. The results are shown in Figure 4.6. For (theoretic) resonantly coupled harmonic oscillators all of the initial excitation is transferred to the second oscillator (red dashed line in Figure 4.6). For high excitation amplitudes of about 7000 quanta, only around 2000 quanta are transferred, while for smaller initial excitations the data approaches the theoretical complete transfer. This can be seen more clearly looking at the coupling efficiency $\kappa = \bar{n}_{1,\mathrm{max}}/\bar{n}_{0,\mathrm{i}}$ (Figure 4.7): For larger initial excitations the efficiency is on the order of $\kappa = 30\,\%$ while for smaller initial excitations it converges to the idealized case of $\kappa = 100\,\%$. This behaviour fits our interpretation of the coupling results as a feature of anharmonic contributions. For larger initial excitation amplitudes, the anharmonic contributions to the trapping potential become more prevalent as the ions motion spans a larger part of the potential.

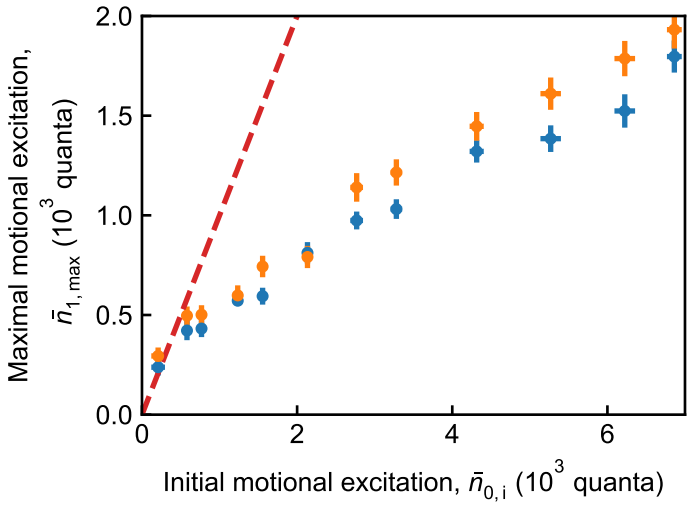

Figure 4.6: For variable initial excitation amplitude at T_0 we measure the maximal excitation transferred to T_1 (blue data points). In an idealized harmonic case one would expect a complete transfer of the excitation (red dashed line). For lower initial excitation the data converges towards this. Error bars indicate the SEM.

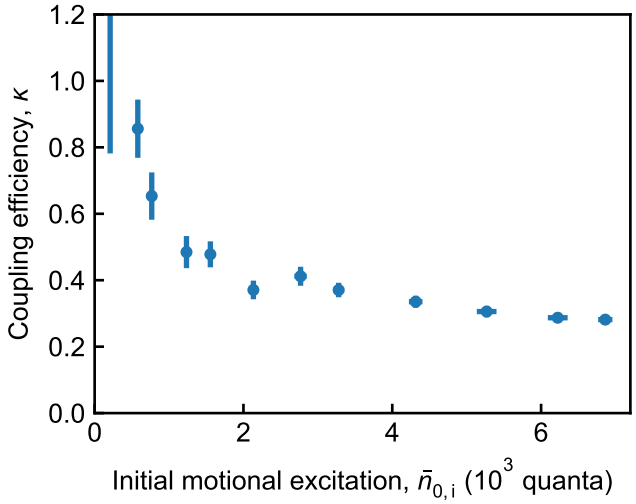

Figure 4.7: For variable initial excitation amplitude at T_0 we measure the maximal excitation transferred to T_1 and calculate the coupling efficiency $\kappa = \bar{n}_{1,\mathrm{max}}/\bar{n}_{0,\mathrm{i}}$. For lower initial excitation the data converges towards the idealized case of $\kappa = 1$ (within uncertainties), while for larger excitations $\kappa \approx 30\,\%$. Error bars indicate the SEM.

The second parameter characterizing the coupling is the coupling rate $\Omega_{\mathrm{C,eff}}$. In Figure 4.8 we plot the reconstructed $\Omega_{\mathrm{C,eff}}$ as a function of the initial excitation $\bar{n}_{0,\mathrm{i}}$. There, we additionally indicate the coupling rate $\Omega_{\mathrm{C,harm}}/(2\pi) = 1.0(1)\,\mathrm{kHz}$ calculated

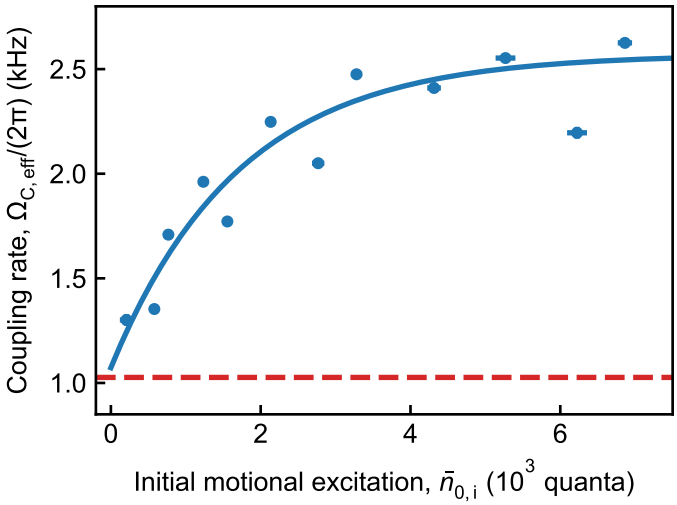

Figure 4.8: For variable initial excitation amplitude at T_0 we measure the coupling rate $\Omega_{\mathrm{C,eff}}$ (blue data points). From independent calibration measurements, of the inter-site distance and motional mode orientations we calculate an idealized coupling rate $\Omega_{\mathrm{C}}/(2\pi) \approx 1\,\mathrm{kHz}$ for harmonic traps (red dashed line). For lower initial excitation the data converges towards this rate, while for larger excitation the rate increases up to $\Omega_{\mathrm{C,eff,lim}}/(2\pi) \approx 2.5\,\mathrm{kHz}$. As a guide to the eye we plot a bounded growth model fit. While the fit uncertainties of the coupling rates are small the values scatter significantly around the fitted systematic trend. We attribute this to variations when setting the resonance between the two sites. Error bars indicate the SEM.

from independent measurements of the inter-site distance and the motional-mode orientations (red-dashed line). As a guide to the eye, we fit the data with a bounded growth model

$$\Omega_{\mathrm{C,eff}}(\bar{n}_0) = \Omega_{\mathrm{C,eff,lim}} - (\Omega_{\mathrm{C,eff,lim}} - \Omega_{\mathrm{C,eff},0})e^{-k\,\bar{n}_{0,\mathrm{i}}} \tag{4.2}$$

model with a coupling for the low-amplitude limit $\Omega_{\mathrm{C,eff},0}/(2\pi) = 1.1(2)\,\mathrm{kHz}$, high-amplitude limit $\Omega_{\mathrm{C,eff,lim}}/(2\pi) = 2.6(1)\,\mathrm{kHz}$ and scaling factor $k = 600(200)\,/\mathrm{quanta}$. The data scatter significantly around this trend, we explain these deviations with experimental variations and drifts between measurements not accounted for by statistical uncertainties of individual measurements. Especially a detuning out of the resonance condition will always lead to a systematically higher coupling rate (see Section 2.5). In our measurement, these variations affect the coupling rate stronger than the exchange amplitudes described before. For large initial excitations, the coupling rate is on the order of $2\pi \times 2.6(1)\,\mathrm{kHz}$. Towards smaller initial excitations the rate approaches

the calculated coupling rate of $2\pi \times 1.0(1)\,\mathrm{kHz}$. This again matches the effect of anharmonic contributions to the trapping potential that become more pronounced for larger oscillation amplitudes.

In a last analysis (Figure 4.9) we compare the coupling efficiency with the relative coupling rate $\Omega_{\mathrm{C,harm}}/\Omega_{\mathrm{C,eff}}$. This is interesting as in the theoretical case of coupled

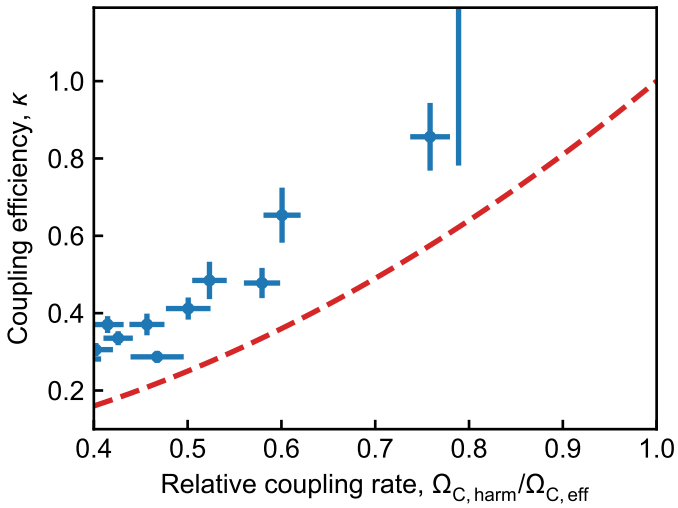

Figure 4.9: To investigate similarities between the effect of anharmonic contributions we plot the reconstructed coupling efficiency as a function of the relative coupling rate $\Omega_{\mathrm{C,harm}}/\Omega_{\mathrm{C,eff}}$. For the idealized harmonic case a detuning between the sites leads to an increased coupling rate, while the coupling efficiency is reduced $\kappa_{\mathrm{C,det}} = (\Omega_{\mathrm{C,harm}}/\Omega_{\mathrm{C,det}})^2$ (red dashed line). The data follows a trend similar to this but shows a systematically higher coupling efficiency. Here, we cannot exclude a systematic error of the reconstructed motional excitation leading to systematically shifted coupling efficiencies. Error bars indicate the SEM.

harmonic oscillators a detuning of the oscillators leads to an increased coupling rate $\Omega_{\mathrm{C,det}}$ and a decreased coupling efficiency $\kappa_{\mathrm{C,det}} = (\Omega_{\mathrm{C,harm}}/\Omega_{\mathrm{C,det}})^2$ (red dashed line in Figure 4.9). Our data suggests a systematically higher coupling efficiency compared to the effect caused by detuned oscillators, while following a similar trend. However, in the experiment, we reach a coupling efficiency compatible with 100 % already for a relative coupling rate of around 0.8. We assume that at this initial amplitude of 210(90) quanta the amplitude-dependent change in motional frequencies due to the anharmonic contributions is small enough to not affect the coupling.

Summary

Our results support our theory that anharmonic contributions to the trapping potential contribute significantly to our coupling results. We see that the effects, an increased coupling rate and a decreased coupling efficiency, approach the theoretical values of harmonic, coupled oscillators if we perform the experiments at reduced amplitude.

This is explained by the anharmonic contributions, which result in amplitude dependent motional frequencies of the oscillating ions. During the coupling, this leads to a dephasing of the oscillators reversing the coupling. A possible experiment to analyse this further would be changing the motional frequency during the coupling to compensate for these changes. This could then, limited by dephasing effects, allow to increase the coupling efficiency. Additionally, one could work on tuning the anharmonic contributions using designated control potentials. Here the number of control electrodes will ultimately limit the number of tunable degrees of freedom. However, in a long-term picture, it is envisioned to operate the trap in the regime of motional states of single quanta. In this regime we expect the present anharmonic contributions to be negligible. Already for lower amplitudes of around 100 quanta, we approach close to the calculated coupling rate and 100 % coupling efficiency. Due to the present heating rates on the order of 10 quanta/ms and decoherence timescales on the order of (60–600) µs we currently favour to work at larger amplitudes and, by this, increased coupling rates. This allows us to establish and improve control of the coupling with no fundamental limitations to using these techniques in the single-quanta regime, which should be reachable using established methods (see Section 2.4.2).

4.3 Real-time multi-site coupling

In the previous Section, we demonstrated the coupling between two sites of our array. In this Section, we extend this control to a sequential coupling between three sites. This is a key requirement for real-time controllable interactions for quantum simulations.

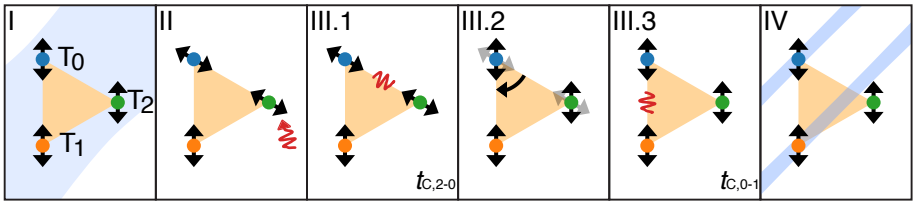

Figure 4.10: Experimental protocol to demonstrate real-time control over the coupling between multiple sites. After global preparation (I), the coupling modes at T_0 and T_2 are rotated towards each other and a coherent state is excited at site T_2 (II). These sites are then coupled for a fixed duration $t_{C,2-0}$ (III.1). Subsequently the coupling mode at T_0 is rotated towards T_1 in 100 µs (III.2). Then T_0 and T_1 are coupled for variable duration $t_{C,0-1}$ (III.3), followed by local detection of sites T_0 and T_1 (IV). Figure adapted from Hakelberg et al. (2019).

The experimental sequence (Figure 4.10) consists of two separate inter-site couplings: After Doppler cooling, we tune the control potential to align the motional modes at sites T_2 and T_0. We then prepare a coherent state at T_2 and couple the two sites for a fixed duration $t_{C,2-0}$ ensuring maximum excitation transfer. In the next step, we adiabatically rotate the motional mode at T_0 towards T_1. This rotation, just like changes to motional frequencies, has to be adiabatic with respect to the motional frequencies. For the data presented here, we use a ramping duration of 100 µs and a duration of 10 µs when tuning in and out of resonance. However, in independent calibration measurements, we found that with our current setup changes on timescales of 20 µs were possible without additional decoherence (see Section 2.4.5). We then, like in the previous Section, couple sites T_0 and T_1 for variable duration $t_{C,0-1}$. To track the evolution of the motional excitation we detect at sites T_0 and T_1. We plot the reconstructed excitation amplitudes in Figure 4.11. To model the data, we again fit Equation 4.1, for the first coupling only to the data for site T_0 and for the second coupling as a combined fit to the data of sites T_0 and T_1. Initially, we excite a motional state of 6800(170) quanta at site T_2. During $t_{C,2-0} = 200$ µs from this 1060(25) quanta are transferred to T_0. The rotation does not change this amplitude at T_0 and creates no measurable additional excitation at T_1. The second coupling is qualitatively comparable to the previous two-site coupling. Motional excitation is exchanged with a rate of $\Omega_{C,\mathrm{eff}}/(2\pi) = 3.09(6)$ kHz and an exchange efficiency of $\kappa = 33(3)$ %. Here we find a decoherence timescale of $\tau_{C,\mathrm{dec}} = 380(35)$ µs. Like for the two-site coupling, we additionally investigate the sum of excitations at sites T_0 and T_1. The deviations of the mean total excitation (grey data points in Figure 4.11)

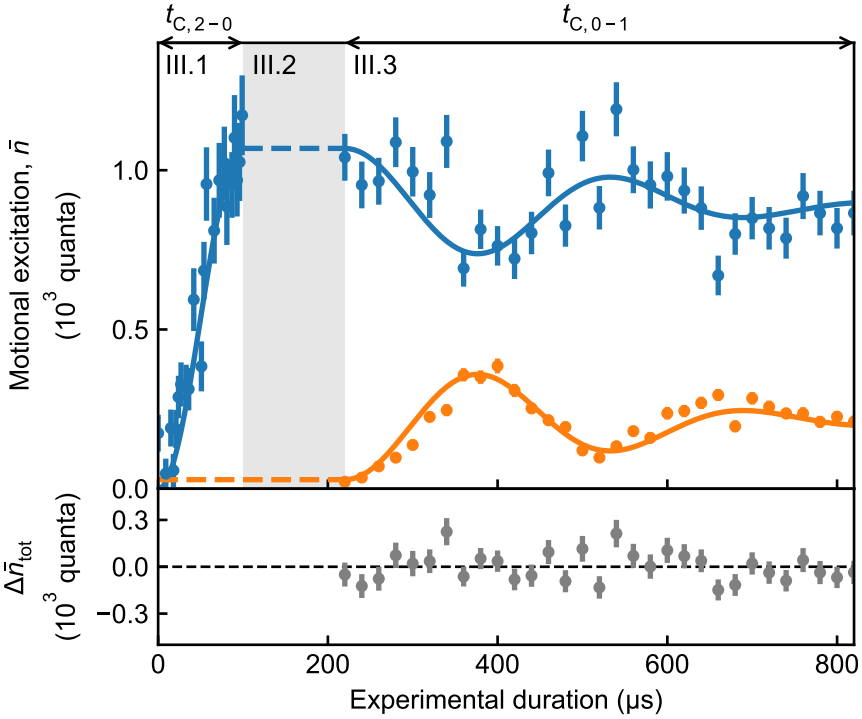

Figure 4.11: Experimental results of real-time control over the coupling between multiple sites. During $t_{C,2-0}$ approximately 1000 quanta are transferred from T_2 to T_0 (blue data points). The rotation of the motional mode at T_0 does not change this excitation (dashed lines). During $t_{C,0-1}$ T_0 and T_1 are coherently coupled and exchange motional excitation with a rate of $2\pi \times 3.09(6)$ kHz. We plot deviations from the average total motional excitation at T_0 and T_1, $\Delta\bar{n}_{tot}$ (grey data points) to emphasize the conservation of motional excitation in the system. Error bars (partially smaller than the marker size) indicate the SEM. Figure adapted from Hakelberg et al. (2019).

show no residual trend. This shows in particular that sites T_0 and T_1 are sufficiently isolated from T_2, which is still excited to an amplitude of around 5820(170) quanta.

These results show that by employing the real-time control of the control potentials in the trap we are able to concatenate coupling protocols to allow sequential inter-site coupling. This does not affect the coupling parameters and is only limited by the present effects due to large amplitudes in combination with the anharmonic contributions to the trapping potential. As described in the previous Sections, this is not a general limit, as established techniques should allow us to work in the single-quanta regime, where anharmonic contributions become negligible. These results are essential in view of scaling up our approach. As the trap design and the experimental techniques are inherently scalable, the sequential coupling will be possible in the same way in larger arrays.

4.4 Global coupling and interference

In the previous Section, we described the sequential coupling between multiple sites in our array. In this Section, we cover the simultaneous coupling of more-than-two sites, here all three sites of our array. In future applications, this will allow to create fully connected two-dimensional lattices with (real-time) tunable inter-site coupling strength.

Here we perform two experiments coupling all three sites of our array simultaneously: In the first experiment, we excite one site and track the evolution of this excitation in the array. In the second experiment, we excite at two sites. The fixed initial phase relation of the two excitations then leads to interference effects of the excitation propagating between the sites.

4.4.1 Single site excitation

In the first experiment, we investigate global coupling with a single excitation.

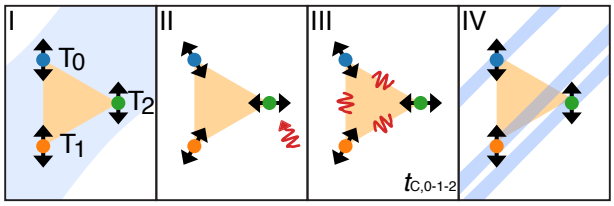

Figure 4.12: Experimental protocol to demonstrate global coupling between three sites. After global preparation (I), all coupling modes are rotated towards the centre of the array and a coherent state is excited at site T_2 (II). The sites are then coupled for variable duration $t_{C,0-1-2}$ (III), followed by local detection of all sites (IV). Figure adapted from Hakelberg et al. (2019).

The experimental sequence (Figure 4.12) begins with Doppler cooling of single ions at all three sites. We then ramp to a control potential where the coupling modes at all three sites are oriented towards the centre of the triangle but detuned in frequency. At site T_2 we prepare a coherent state of motion using resonant excitation, while not exciting at T_0 and T_1. We then couple the three sites, followed by motional state detection for all three sites. To set the resonance conditions in the array, we first scan the motional frequency at site T_2 while observing the coupling to T_1. By this, we can tune these two sites into resonance. Consecutively we scan the motional frequency at site T_0 while observing the coupling to T_0, setting the second resonance condition. Here, compared to the two-site coupling, the crosstalk of the frequency tuning control profiles should be minimized, to not detune the first coupling while setting the second. We verify that all frequencies are set correctly by iterating the protocol.

In Figure 4.13 we show the resulting data of the coupling reconstructed at all three sites. We fit the trace of each site individually using Equation 4.1. Initially, we excite T_2 to 5370(130) quanta. This excitation is then simultaneously transferred to T_0 and T_1 with approximately equal efficiency and coupling rate. We extract a maximal transfer

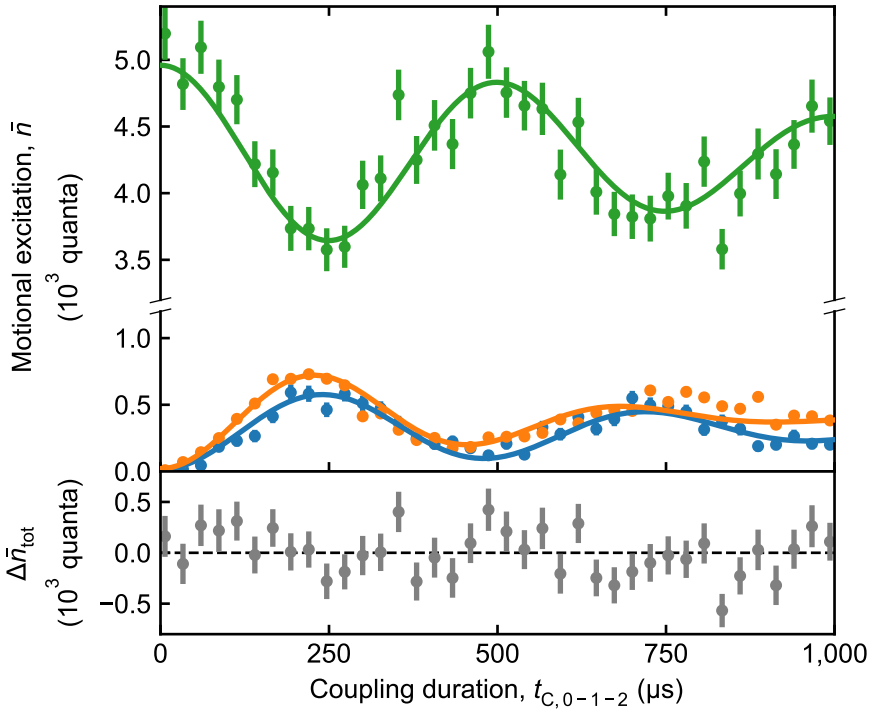

Figure 4.13: Experimental results of global coupling between three sites exciting at one site. The ion at T_2 is initially excited to approximately 5000 quanta (green data points). Around 1300 quanta are transferred, approximately equally distributed to T_0 and T_1 and back with a rate of $2\pi \times 2.0(1)$ kHz (blue and orange data points). We plot deviations from the average total motional excitation $\Delta\bar{n}_{\mathrm{tot}}$ (grey data points) to emphasize the conservation of motional excitation in the system Error bars (partially smaller than the marker size) indicate the SEM. Figure adapted from Hakelberg et al. (2019).

to T_0 of $\bar{n}_0 = 580(30)$ quanta and to T_1 of $\bar{n}_1 = 760(40)$ quanta. The individually fitted oscillation rates are $\Omega_{\mathrm{C,eff},0}/(2\pi) = 2.05(3)$ kHz, $\Omega_{\mathrm{C,eff},1}/(2\pi) = 2.13(4)$ kHz, and $\Omega_{\mathrm{C,eff},2}/(2\pi) = 1.98(3)$ kHz. We attribute the deviations between the individual frequencies to the sequential measurement procedure where drifts in the motional frequencies during the measurements alter the coupling rates. The data is described by the expected behaviour where T_0 and T_1 are driven by the common source (T_2) with similar coupling strength and to similar amplitude. They, therefore, oscillate in-phase and do not exchange excitation with each other. The same results would be expected if there were no direct coupling between T_1 and T_2, i.e. a linear chain of oscillators.

4.4.2 Multi-site excitation and interference

In a second experiment, we investigate the evolution of multiple excitations in our coupled three-site system. We employ an experimental sequence (Figure 4.14), similar to the previous one, with an additional excitation at T_0, before the excitation at T_2.

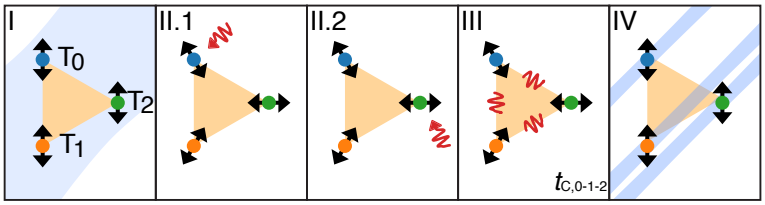

Figure 4.14: Experimental protocol to demonstrate motional interference between three sites. After global preparation (I), all coupling modes are rotated towards the centre of the array and coherent states are excited at sites T_0 and T_2 successively (II.1 & II.2). The sites are then coupled for variable duration $t_{C,0-1-2}$ (III), followed by local detection of all sites (IV). Figure adapted from Hakelberg et al. (2019).

Our experimental control system allows us to choose a fixed phase relation between the excitation pulses. This phase relation is transferred to the oscillation of the ions. It is important to note that due to the different frequencies of the uncoupled sites the phase difference is not constant in time. It is, however, the same for successive realizations of the experiment.

To configure the resonance condition, we employ a two-step process: First, we tune the frequency at T_2 maximizing the coupling to site T_1. Then we tune the frequency at T_0 again observing the coupling to T_1. We couple all three sites for variable $t_{C,0-1-2}$ followed by detection at all sites in consecutive experiments. The resulting data (Figure 4.15) shows oscillations of the motional excitations at all three sites. We model these using sine functions with variable phase, amplitude, and frequency. We find peak to peak oscillation amplitudes of (470(60), 390(30), 450(59)) quanta, frequencies of $2\pi\times(2.09(7),\ 1.80(6),\ 2.02(7))$ kHz, and phases $2\pi\times(-0.05(5),\ -0.16(3),\ 0.38(4))$ (at sites T_0, T_1, and T_2).

Compared to the previous experiment, using a single excitation, the resulting signal is considerably more complex. The additional excitation, in combination with the phase relation that is fixed for all realisations, leads to interference effects of the coherent states propagating in the triangle. Here all three direct inter-site couplings become relevant as the excitation is transferred alternately from and to all sites. This is in distinct difference to a linear chain with nearest-neighbour interactions. It is interesting to note that for this realization of the experiment we see no effect of decoherence during the 1000 µs coupling duration. This could be explained in the theory of networks of coupled oscillators where a stabilizing effect can be achieved for specific phase conditions between oscillators (Dörfler and Bullo 2014). Here further investigation will be needed.

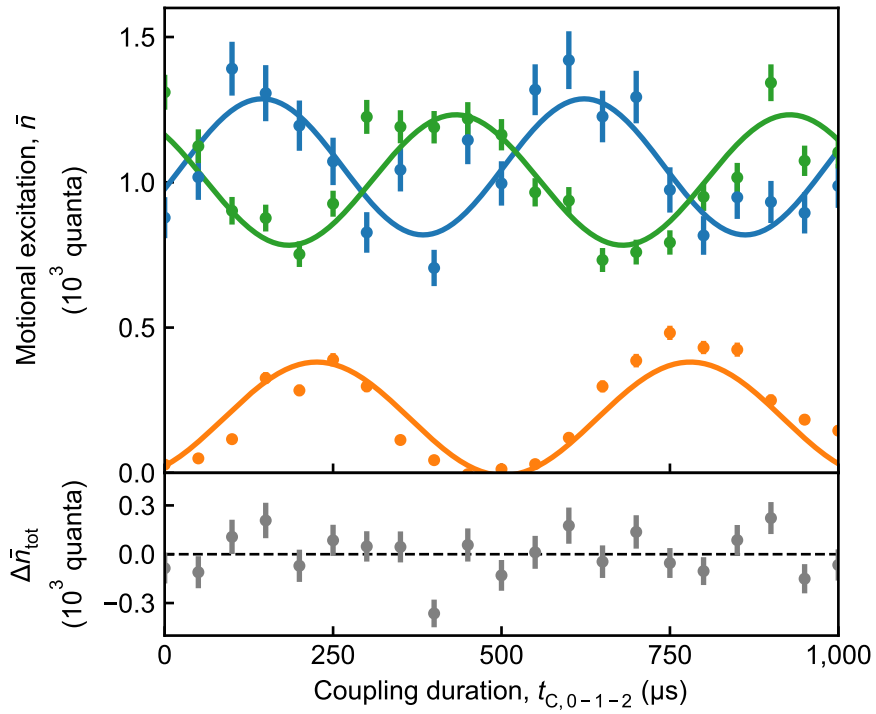

Figure 4.15: Experimental results demonstrating interference between all three sites of the array. Both ions at T_0 and T_2 are initially excited to approximately 1000 quanta (blue and green data points) with a phase relation fixed between experimental realisations. The excitation is coherently transferred between the three sites due to this phase relation, allowing to observe interference of the coherent states of motion. We fit the local excitation at each site with a sine function with individual frequency of approx. $2\pi \times 2\,\mathrm{kHz}$, amplitude and phase. We plot deviations from the average total motional excitation $\Delta\bar{n}_{\mathrm{tot}}$ (grey data points) to emphasize the conservation of motional excitation in the system Error bars (partially smaller than the marker size) indicate the SEM. Figure adapted from Hakelberg et al. (2019).

4.5 Discussion

The results presented here are part of the course towards a fully-configurable two-dimensional quantum simulator based on individually trapped ions. There, the inter-site coupling presents an essential building block that was missing so far. The demonstrated coupling between two sites is the key ingredient towards fully connected lattices of trapped ions. It is the first realization of inter-site coupling in a two-dimensional ion trap array approach and the techniques we developed. Due to the motional heating rates, it is currently still advantageous to work with large coherent states of motion, where the interaction could in principle be fully described by classical mechanics. The large motional amplitudes of these states lead to a significant influence of the anharmonic potentials in the trap, as expected from a qualitative simulation presented in Section 2.5.1. We investigate this by varying the motional amplitudes during the coupling, which allows us to extrapolate to the coupling in the quantum regime, i.e. the tunnelling of single quanta. These extrapolations are in agreement with the expected model of coupled harmonic oscillators. This confirms our assumptions that our results can be extended to the regime of single quanta once the motional heating rates have been reduced.

Furthermore, motional decoherence rates with typical timescales on the order of several 100 µs limit the current length of coherent coupling experiments in our trap. We perform additional Ramsey-like coherence measurements similar to the ones described in Section 2.4.2: We excite at a motional state at one site, followed by a coupling experiment transferring the excitation to a second site. We then perform a second excitation pulse with variable phase at the second site to measure the loss of coherence during the coupling. The measured coherence timescales of these experiments are compatible with the decoherence observed for a waiting duration equal to the coupling duration. We conclude that the coupling itself does not induce any additional significant decoherence.

The following experiments investigate the scalability of the coupling. To demonstrate the real-time control, we concatenate the two-site coupling using real-time shaping of control potentials. In future applications, this will open up the ability to tackle not only statically configured problems but also such where coupling strengths are tuned or switched on/off during the evolution of the system. Already in Kiefer et al. (2019), we employed this control to implement a phonon-assisted coupling between detuned sites by a local modulation of the trapping potential (Bermudez et al. 2011).

In the last two experiments, we investigate the simultaneous coupling of all three sites. This substantially increases the requirement on the control of the system since all three sites have to be tuned to resonance during the coupling. The results show that we are able to use control profiles of low cross-talk to couple multiple sites in our array. These results are essential demonstrations as they show the scalability of our techniques in the inherently scalable trapping architecture.

In future experiments, several improvements, some of which we started implementing, will allow to progress further towards the envisioned quantum simulators. We replaced our PMT by a spatially resolving individual sites and similar detection efficiencies,

which is described in detail in Guth (2019). This allows us to detect the motional state at all three sites simultaneously, thereby reducing the impact of systematic drifts and allowing to resolve correlations between sites. The implementation of argon-ion cleaning, as already planned and set up with the new apparatus, promises to reduce the motional heating rates to a level where coherent tunnelling dominates in the regime of single-quanta.

5 Conclusion and Outlook

In this thesis, we demonstrate key elements in the toolbox of two-dimensional quantum simulations based on individually trapped ions. Additionally, we describe the design, construction, and characterization of a new experimental setup. Our results presented in Chapter 4 and published in Hakelberg et al. (2019) build strongly on our individual control of trapping sites in our triangular arrays (Kalis et al. 2016; Mielenz et al. 2016). There, we especially investigated the inherent scalability of our trapping architecture regarding the trap depth calculated up to infinitely sized arrays and individual controllability of the electrical potential at each trapping site using control electrodes embedded into the trap chip.

Here, we realize for the first time in a two-dimensional ion trap array resonant inter-site coupling of the motional degrees of freedom of single trapped ions via the common Coulomb interaction. This coupling, previously only realized in one-dimensional arrangements (Brown et al. 2011; Harlander et al. 2011), is a long-sought key ingredient of the envisioned quantum simulator approach. For our experiments, we use coherent motional states of large amplitude [(200–7000) quanta] due to the large motional heating rate of 10 quanta/ms in the trap. We investigate the effects of this with regards to anharmonic contributions of the trapping potential and find, in extrapolation to motional states of low amplitude, agreement with the model of coupled harmonic oscillators. We conclude that our findings will be relevant also in the quantum regime where single quanta of motional excitation are transferred between sites. We measure coupling rates on the order of $\Omega_{\mathrm{C,eff}}/(2\pi) \approx (2\text{–}3)\,\mathrm{kHz}$ with extrapolations to $\Omega_{\mathrm{C,harm}}/(2\pi) \approx (1\text{–}2)\,\mathrm{kHz}$ in the single-quanta regime, suitable for first quantum simulation experiments. Our measurements also require a new more involved reconstruction of the motional states incorporating the site-specific effects of anharmonic trapping potential and micromotion. While we find that the coupling does not induce additional motional decoherence, the observed wide range of coherence timescales of (60–600) µs depending, for instance, on experimental control potential configurations, requires further investigation. We further extend our experimental protocols to investigate the scalability of this coupling: First, we concatenate the two-site coupling in real-time showing consecutive transfer of motional excitation in the trap. Then we demonstrate the global coupling of all three sites of our array. This increases the requirement on the control as all three sites have to be tuned to resonance simultaneously. Using this global coupling we show the evolution of a single excitation in the triangle and, by using two excitations with fixed phase relation, the interference of coherent states of motion oscillating between the coupled sites.

The new experimental setup is compatible with the triangle trap array and will allow for in-situ cleaning of the traps by argon-ion bombardment to reduce motional

heating rates. In this apparatus, we successfully trapped single ions in a linear surface-electrode trap. Additionally, in the new setup, we realize a hybrid system to generate a magnetic quantization field at approximately 10.9 mT. This allows the realization of a first-order magnetic field insensitive qubit in the hyperfine levels of $^{25}Mg^{+}$. We characterize this qubit and find a coherence timescale of 6.6(9) s, far above envisioned experimental durations of up to several 10 ms. We additionally use the qubit for a first quantum sensing experiment of an oscillating magnetic field originating from stray currents in the radio-frequency electrode. The stable qubit is of interest not only for quantum simulations but also as a long-lived memory. While the realization of first-order field-independent transitions is not new, previous realizations depend on electric coils for generating the necessary magnetic field strengths. This comes with a significant power consumption and thermal load were often the coils have to be water-cooled. In our approach, only currents on the order of several 10 mA are needed to compensate for residual drifts in the magnetic field strength. This will allow for new applications with significantly reduced power and cooling requirements.

In future experiments building on our architecture, the effects of scaling the approach can be investigated while additionally, first quantum simulation experiments become in reach (see below). Subsequently to the results presented here we realized the coupling of detuned sites via local modulation of the motional frequencies at the difference frequency, phonon-assisted coupling proposed in Bermudez et al. (2011, 2012), which we published in Kiefer et al. (2019) and, which is described in detail in Philip Kiefer's dissertation (Kiefer 2019). The next major improvement, still working with the same trap of three sites, will be reducing the motional heating rate by argon-ion bombardment in the new experimental apparatus described in this work. This technique has proven to allow reductions in the motional heating rate by two orders of magnitude, in our case to below 10 % of the inter-site coupling rate, (Hite et al. 2012). Reducing the current heating rates (on the order of 10 quanta/ms) to about 0.1 quanta/ms will allow coupling experiments in the single-quanta regime. Here less than 0.1 quanta of additional heating are expected for typical coupling timescales of $2\pi/\Omega_C = (0.5\text{–}1)$ ms. Working in this regime will allow us to fully exploit the unique ability to couple internal and motional degrees of freedom established for trapped ions, which we already used to demonstrate cooling to the motional ground state in the triangle trap array (Kalis et al. 2016). Additionally, actively stabilizing the radio-frequency voltage might reduce the observed motional decoherence rates further (Johnson et al. 2016). Coupling close to the ground-state of motion will allow the implementation of an effective spin-spin interaction mediated via the motional Coulomb coupling (Porras and Cirac 2004), realized previously for two sites in a linear trap (Wilson et al. 2014). This, in turn, can be used to simulate quantum-spin models (Schmitz et al. 2009a) for instance, spin-frustration of the three sites of our array. Here results in the field of superconducting qubits in a similar triangular architecture (Roushan et al. 2017) might allow a comparison of different architectures. Future trap arrays designed following the considerations in Section 2.3.4 could include, for example, a *ladder* array of concatenated square plaquettes, i.e. $(2 \times N)$ sites, possibly further shrinking the inter-site spacing to increase coupling strengths. Therein by successively

filling up sites the system size can be increased ion by ion. Along these plaquettes, the phonon-assisted coupling is envisioned to allow the simulation of synthetic gauge fields Bermudez et al. (2011, 2012). The modulation techniques we use for this could also be applied to implement a local squeezing operation (Burd et al. 2019; Wittemer et al. 2019), which could be used to amplify effective spin-spin interactions (Ge et al. 2019). Loading more-than-one ion per site, as used here to measure motional-mode orientations, can further boost the coupling strengths (Harlander et al. 2011) and, by using different isotopes or atomic species, will allow sympathetic cooling during experiments as proposed, for example, by Bermudez et al. (2013). Future arrays are not bound to be periodic but can be designed at will to more closely model a desired system, also extending in the third dimension, for example, in a two-layer configuration (Schmied et al. 2009). Further experiments could be performed investigating the effects of thermalisation (Clos et al. 2016) or transport processes (Bermudez and Schaetz 2016).

Danksagung

Als erstes danke ich *Tobias Schätz*, der mir diese Arbeit ermöglicht hat, mir die Freiheit und das Vertrauen gab, ein eigenes Experiment und Vakuumkammer aufzubauen, und nie daran gezweifelt hat, dass diese Wechselwirkung im Dreieck zu zeigen sein muss. Vielen Dank auch an *Ulrich Warring*, der mir vom ersten Tag meiner Masterarbeit an mit Rat, Tat und konstruktiver Kritik zur Verfügung stand und damit einen großen Einfluss auf all meine Arbeit hatte. Außerdem danke ich meinen Vorgängern am Dreickesfallen (Bermuda) Experiment: Vielen Dank meinem ersten Büronachbarn *Manuel Mielenz* für seine Arbeiten an Bermuda und die Erklärungen dazu. Einen speziellen Dank an *Henning Kalis*, der mir das Experiment einschließlich Physik, Software (GUI), Elektronik und Optik von Grund auf geduldig beigebracht hat. Vielen Dank *Raphaël Saint-Jalm* für die Vorarbeiten zur Argonkanone. Ganz besonders danke ich *Philip Kiefer*, mit dem ich die fast schon aufgegebene (nicht von Tobias) Wechselwirkung im Dreieck zeigen konnte, und praktisch alle Daten dieser Arbeit aufnehmen konnte. Vielen Dank an *Matthias Wittemer* für das gemeinsame Arbeiten an den Magnesium Experimenten. Danke auch an Philip und Matthias zusammen für die (nicht immer zu 110% effiziente) Zeit im gemeinsamen Büro, vor allem beim parallelen Zusammenschreiben. *Jan-Philip Schröder*, vielen Dank für interessante Software & Machine-Learning Diskussionen. Vielen Dank *Prasath Palani*, für das Weiterführen der Oberflächenfallen- und insbesondere der Argonreinigungsexperimente. Ich danke den Bachelor & Master Studenten am Dreiecks Experiment, *Leonard Nitzsche*, *Valentin Vierhub-Lorenz*, *Sebastian Schnell*, *Lennart Guth* und *Yannick Minet*. Insbesondere Leonard für seine große Motivation und seinen Einsatz, ohne den die neue Kammer sicher nicht so schnell und gut Ionen gefangen hätte. Vielen Dank an *Helga Müller*, für die Unterstützung bei allen Verwaltungsakten, insbesondere unzähliger Bestellungen trotz erschwerter Bedingungen (SAP). Ebenfalls vielen Dank an *Jörn Denter*, unter anderem, für stets gewartete Dye Laser und die Hilfe bei Beschaffung und Handling großer Mengen explosiver Chemikalien. Ein großer Dank geht auch an die Mechanische Werkstatt des Physikalischen Instituts, vertreten durch *Herrn Großmann*, ohne die der Bau der neuen Vakuumkammer so nicht möglich gewesen wäre. Ich danke allen weiteren momentanen und ehemaligen (*) Doktoranden und PostDocs der AG Schätz, einschließlich *Jonathan Brox**, *Govinda Clos**, *Julian Schmidt**, *Alexander Lambrecht**, *Pascal Weckesser*, *Fabian Thielemann*, *Daniel Hönig*, *Markus Debatin** und *Leon Karpa*.

Abschließend möchte ich meinen Freunden und meiner Familie danken. Insbesondere meinen Eltern, *Iris* und *Harald*, und meiner Schwester *Liz*, vielen Dank, dass ihr mich immer unterstützt habt. Und natürlich *Julia*, für alles.

Frederick Hakelberg

Bibliography

Agrawal, A., Verschueren, R., Diamond, S. and Boyd, S., 'A Rewriting System for Convex Optimization Problems', Journal of Control and Decision **5**, 42–60 (2018).

Allcock, D. T. C., Guidoni, L., Harty, T. P., Ballance, C. J., Blain, M. G., Steane, A. M. and Lucas, D. M., 'Reduction of heating rate in a microfabricated ion trap by pulsed-laser cleaning', New Journal of Physics **13**, 123023 (2011) 10.1088/1367-2630/13/12/123023.

Allcock, D. T. C., Harty, T. P., Janacek, H. A., Linke, N. M., Ballance, C. J., Steane, A. M., Lucas, D. M., Jarecki, R. L., Habermehl, S. D., Blain, M. G., Stick, D. and Moehring, D. L., 'Heating rate and electrode charging measurements in a scalable, microfabricated, surface-electrode ion trap', Applied Physics B **107**, 913–919 (2012) 10.1007/s00340-011-4788-5.

Aspuru-Guzik, A. and Walther, P., 'Photonic quantum simulators', Nature Physics **8**, 285–291 (2012) 10.1038/nphys2253.

Barredo, D., Lienhard, V., de Léséleuc, S., Lahaye, T. and Browaeys, A., 'Synthetic three-dimensional atomic structures assembled atom by atom', Nature **561**, 79–82 (2018) 10.1038/s41586-018-0450-2.

Berkeland, D. J., Miller, J. D., Bergquist, J. C., Itano, W. M. and Wineland, D. J., 'Minimization of ion micromotion in a Paul trap', Journal of Applied Physics **83**, 5025 (1998) 10.1063/1.367318.

Bermudez, A., Schaetz, T. and Plenio, M. B., 'Dissipation-Assisted Quantum Information Processing with Trapped Ions', Physical Review Letters **110** (2013) 10.1103/PhysRevLett.110.110502.

Bermudez, A. and Schaetz, T., 'Quantum transport of energy in controlled synthetic quantum magnets', New Journal of Physics **18**, 083006 (2016) 10.1088/1367-2630/18/8/083006.

Bermudez, A., Schaetz, T. and Porras, D., 'Synthetic Gauge Fields for Vibrational Excitations of Trapped Ions', Physical Review Letters **107**, 150501 (2011) 10.1103/PhysRevLett.107.150501.

Bermudez, A., Schaetz, T. and Porras, D., 'Photon-assisted-tunneling toolbox for quantum simulations in ion traps', New Journal of Physics **14**, 053049 (2012) 10.1088/1367-2630/14/5/053049.

Bernien, H., Schwartz, S., Keesling, A., Levine, H., Omran, A., Pichler, H., Choi, S., Zibrov, A. S., Endres, M., Greiner, M., Vuletić, V. and Lukin, M. D., 'Probing many-body dynamics on a 51-atom quantum simulator', Nature **551**, 579–584 (2017) 10.1038/nature24622.

Blatt, R. and Roos, C. F., 'Quantum simulations with trapped ions', Nature Physics **8**, 277–284 (2012) 10.1038/nphys2252.

Bollinger, J., Heizen, D., Itano, W., Gilbert, S. and Wineland, D., 'A 303-MHz frequency standard based on trapped Be+ ions', IEEE Transactions on Instrumentation and Measurement **40**, 126–128 (1991) 10.1109/TIM.1990.1032897.

Bowler, R., Warring, U., Britton, J. W., Sawyer, B. C. and Amini, J., 'Arbitrary waveform generator for quantum information processing with trapped ions', Review of Scientific Instruments **84**, 033108 (2013) 10.1063/1.4795552.

Brady, G. R., Ellis, A. R., Moehring, D. L., Stick, D., Highstrete, C., Fortier, K. M., Blain, M. G., Haltli, R. A., Cruz-Cabrera, A. A., Briggs, R. D., Wendt, J. R., Carter, T. R., Samora, S. and Kemme, S. A., 'Integration of fluorescence collection optics with a microfabricated surface electrode ion trap', Applied Physics B **103**, 801–808 (2011) 10.1007/s00340-011-4453-z.

Brewer, S. M., Chen, J.-S., Hankin, A. M., Clements, E. R., Chou, C. W., Wineland, D. J., Hume, D. B. and Leibrandt, D. R., '$^{27}Al^{+}$ Quantum-Logic Clock with a Systematic Uncertainty below 10^{-18}', Physical Review Letters **123** (2019) 10.1103/PhysRevLett.123.033201.

Britton, J. W., Sawyer, B. C., Keith, A. C., Wang, C.-C. J., Freericks, J. K., Uys, H., Biercuk, M. J. and Bollinger, J. J., 'Engineered two-dimensional Ising interactions in a trapped-ion quantum simulator with hundreds of spins', Nature **484**, 489–492 (2012) 10.1038/nature10981.

Brown, K. R., Ospelkaus, C., Colombe, Y., Wilson, A. C., Leibfried, D. and Wineland, D. J., 'Coupled quantized mechanical oscillators', Nature **471**, 196–199 (2011) 10.1038/nature09721.

Bruzewicz, C. D., McConnell, R., Chiaverini, J. and Sage, J. M., 'Scalable loading of a two-dimensional trapped-ion array', Nature Communications **7** (2016) 10.1038/ncomms13005.

Buluta, I. and Nori, F., 'Quantum Simulators', Science **326**, 108–111 (2009) 10.1126/science.1177838.

Burd, S. C., Srinivas, R., Bollinger, J. J., Wilson, A. C., Wineland, D. J., Leibfried, D., Slichter, D. H. and Allcock, D. T. C., 'Quantum amplification of mechanical oscillator motion', Science **364**, 1163–1165 (2019) 10.1126/science.aaw2884.

Carruthers, P., 'Coherent States and the Forced Quantum Oscillator', American Journal of Physics **33**, 537 (1965) 10.1119/1.1971895.

Chiaverini, J., Blakestad, R. B., Britton, J., Jost, J. D., Langer, C., Leibfried, D., Ozeri, R. and Wineland, D. J., 'Surface-electrode Architecture for Ion-trap Quantum Information Processing', Quantum Info. Comput. **5**, 419–439 (2005).

Chiaverini, J. and Lybarger, W. E., 'Laserless trapped-ion quantum simulations without spontaneous scattering using microtrap arrays', Physical Review A **77** (2008) 10.1103/PhysRevA.77.022324.

Chubar, O., Elleaume, P. and Chavanne, J., 'A three-dimensional magnetostatics computer code for insertion devices', Journal of Synchrotron Radiation **5**, 481–484 (1998) 10.1107/S0909049597013502.

Cirac, J. I. and Zoller, P., 'Quantum Computations with Cold Trapped Ions', Physical Review Letters **74**, 4091–4094 (1995) 10.1103/PhysRevLett.74.4091.

Cirac, J. I. and Zoller, P., 'A scalable quantum computer with ions in an array of microtraps', Nature **404**, 579–581 (2000) 10.1038/35007021.

Cirac, J. I. and Zoller, P., 'Goals and opportunities in quantum simulation', Nature Physics **8**, 264 (2012).

Clark, R. J., Lin, T., Brown, K. R. and Chuang, I. L., 'A two-dimensional lattice ion trap for quantum simulation', Journal of Applied Physics **105**, 013114 (2009) 10.1063/1.3056227.

Clos, G., 'Trapped Atomic Ions for Fundamental Studies of Closed and Open Quantum Systems', PhD thesis (Albert-Ludwigs-Universität, 2017), 10.6094/UNIFR/12400.

Clos, G., Enderlein, M., Warring, U., Schaetz, T. and Leibfried, D., 'Decoherence-Assisted Spectroscopy of a Single Mg^+ Ion', Physical Review Letters **112** (2014) 10.1103/PhysRevLett.112.113003.

Clos, G., Porras, D., Warring, U. and Schaetz, T., 'Time-Resolved Observation of Thermalization in an Isolated Quantum System', Physical Review Letters **117** (2016) 10.1103/PhysRevLett.117.170401.

Crylas FDSS532-150 Datasheet, http://crylas-inc.com/wp-content/uploads/2017/02/FDSS_532-150.pdf, Apr. 2013.

Danieli, E., Perlo, J., Blümich, B. and Casanova, F., 'Highly Stable and Finely Tuned Magnetic Fields Generated by Permanent Magnet Assemblies', Physical Review Letters **110** (2013) 10.1103/PhysRevLett.110.180801.

Daniilidis, N., Gerber, S., Bolloten, G., Ramm, M., Ransford, A., Ulin-Avila, E., Talukdar, I. and Häffner, H., 'Surface noise analysis using a single-ion sensor', Physical Review B **89** (2014) 10.1103/PhysRevB.89.245435.

Dekker, N. H., Lee, C. S., Lorent, V., Thywissen, J. H., Smith, S. P., Drndić, M., Westervelt, R. M. and Prentiss, M., 'Guiding Neutral Atoms on a Chip', Physical Review Letters **84**, 1124–1127 (2000) 10.1103/PhysRevLett.84.1124.

DeVoe, R. G., Hoffnagle, J. and Brewer, R. G., 'Role of laser damping in trapped ion crystals', Physical Review A **39**, 4362 (1989).

DeVoe, R. G., 'Elliptical ion traps and trap arrays for quantum computation', Physical Review A **58**, 910–914 (1998) 10.1103/PhysRevA.58.910.

Diamond, S. and Boyd, S., 'CVXPY: A Python-Embedded Modeling Language for Convex Optimization', Journal of Machine Learning Research **17**, 1–5 (2016).

DiVincenzo, D. P., 'The Physical Implementation of Quantum Computation', Fortschritte der Physik **48**, 771–783 (2000) 10.1002/1521-3978(200009)48:9/11<771::AID-PROP771>3.0.CO;2-E.

Dörfler, F. and Bullo, F., 'Synchronization in complex networks of phase oscillators: A survey', Automatica **50**, 1539–1564 (2014) 10.1016/j.automatica.2014.04.012.

Earnshaw, S., 'On the nature of the molecular forces which regulate the constitution of the luminferous ether', Trans. Camb. Phil. Soc. **7**, 97–112 (1842).

Elleaume, P., Chubar, O. and Chavanne, J., 'Computing 3D magnetic fields from insertion devices', Proceedings of the 1997 Particle Accelerator Conference (Cat. No.97CH36167), Vol. 3 (1998), pp. 3509–3511, 10.1109/PAC.1997.753258.

Engheta, N., Murphy, W. D., Rokhlin, V. and Vassiliou, M. S., 'The fast multipole method (FMM) for electromagnetic scattering problems', IEEE Transactions on Antennas and Propagation **40**, 634–641 (1992) 10.1109/8.144597.

Eschner, J., Morigi, G., Schmidt-Kaler, F. and Blatt, R., 'Laser cooling of trapped ions', Journal of the Optical Society of America B **20**, 1003 (2003) 10.1364/JOSAB.20.001003.

Feynman, R. P., 'Simulating physics with computers', International Journal of Theoretical Physics **21**, 467–488 (1982) 10.1007/BF02650179.

Folman, R., Krüger, P., Cassettari, D., Hessmo, B., Maier, T. and Schmiedmayer, J., 'Controlling Cold Atoms using Nanofabricated Surfaces: Atom Chips', Physical Review Letters **84**, 4749–4752 (2000) 10.1103/PhysRevLett.84.4749.

Friedenauer, A., Markert, F., Schmitz, H., Petersen, L., Kahra, S., Herrmann, M., Udem, T., Hänsch, T. and Schätz, T., 'High power all solid state laser system near 280 nm', Applied Physics B **84**, 371–373 (2006) 10.1007/s00340-006-2274-2.

Friedenauer, A., Schmitz, H., Glueckert, J. T., Porras, D. and Schaetz, T., 'Simulating a quantum magnet with trapped ions', Nature Physics **4**, 757–761 (2008) 10.1038/nphys1032.

Friedenauer, A., 'Simulation of the Quantum Ising Model in an Ion Trap', PhD thesis (Ludwig-Maximilans-Universität, München, 2010).

Ge, W., Sawyer, B. C., Britton, J. W., Jacobs, K., Bollinger, J. J. and Foss-Feig, M., 'Trapped Ion Quantum Information Processing with Squeezed Phonons', Physical Review Letters **122** (2019) 10.1103/PhysRevLett.122.030501.

Georgescu, I. M., Ashhab, S. and Nori, F., 'Quantum simulation', Reviews of Modern Physics **86**, 153–185 (2014) 10.1103/RevModPhys.86.153.

Grant, M. and Boyd, S., 'Graph implementations for nonsmooth convex programs', *Recent advances in learning and control*, edited by V. Blondel, S. Boyd and H. Kimura, Lecture notes in control and information sciences (Springer-Verlag Limited, 2008), pp. 95–110.

Grant, M. and Boyd, S., 'CVX: matlab software for disciplined convex programming, version 2.1', (2014).

Gulde, S., Riebe, M., Lancaster, G. P. T., Becher, C., Eschner, J., Häffner, H., Schmidt-Kaler, F., Chuang, I. L. and Blatt, R., 'Implementation of the Deutsch–Jozsa algorithm on an ion-trap quantum computer', Nature **421**, 48–50 (2003) 10.1038/nature01336.

Guth, L., '2D-Quantensysteme in Oberflächenfallen Aufbau und Charakterisierung eines Vier-Quadranten-Photonendetektionssystems zur parallelen Zustandsanalyse von Magnesiumionen', Masters thesis (Albert-Ludwigs-Universität, Freiburg, Feb. 2019).

Hahn, E. L., 'Spin Echoes', Physical Review **80**, 580–594 (1950) 10.1103/PhysRev.80.580.

Hakelberg, F., Kiefer, P., Wittemer, M., Schaetz, T. and Warring, U., 'Hybrid setup for stable magnetic fields enabling robust quantum control', Scientific Reports **8** (2018) 10.1038/s41598-018-22671-5.

Hakelberg, F., Kiefer, P., Wittemer, M., Warring, U. and Schaetz, T., 'Interference in a Prototype of a Two-Dimensional Ion Trap Array Quantum Simulator', Physical Review Letters **123** (2019) 10.1103/PhysRevLett.123.100504.

Hänsch, T. W. and Schawlow, A. L., 'Cooling of gases by laser radiation', Optics Communications **13**, 68–69 (1975).

Harlander, M., Lechner, R., Brownnutt, M., Blatt, R. and Hänsel, W., 'Trapped-ion antennae for the transmission of quantum information', Nature **471**, 200–203 (2011) 10.1038/nature09800.

Hauke, P., Cucchietti, F. M., Tagliacozzo, L., Deutsch, I. and Lewenstein, M., 'Can one trust quantum simulators?', Reports on Progress in Physics **75**, 082401 (2012) 10.1088/0034-4885/75/8/082401.

Helmer, F., Mariantoni, M., Fowler, A. G., von Delft, J., Solano, E. and Marquardt, F., 'Cavity grid for scalable quantum computation with superconducting circuits', EPL (Europhysics Letters) **85**, 50007 (2009) 10.1209/0295-5075/85/50007.

Hendricks, R., Grant, D., Herskind, P., Dantan, A. and Drewsen, M., 'An all-optical ion-loading technique for scalable microtrap architectures', Applied Physics B **88**, 507–513 (2007) 10.1007/s00340-007-2698-3.

Hite, D. A., Colombe, Y., Wilson, A. C., Allcock, D. T. C., Leibfried, D., Wineland, D. J. and Pappas, D. P., 'Surface science for improved ion traps', MRS Bulletin **38**, 826–833 (2013) 10.1557/mrs.2013.207.

Hite, D. A., Colombe, Y., Wilson, A. C., Brown, K. R., Warring, U., Jördens, R., Jost, J. D., McKay, K. S., Pappas, D. P., Leibfried, D. and Wineland, D. J., '100-Fold Reduction of Electric-Field Noise in an Ion Trap Cleaned with In Situ Argon-Ion-Beam Bombardment', Physical Review Letters **109** (2012) 10.1103/PhysRevLett.109.103001.

Hucul, D., Yeo, M., Olmschenk, S., Monroe, C., Hensinger, W. K. and Rabchuk, J., 'On the Transport of Atomic Ions in Linear and Multidimensional Ion Trap Arrays', Quantum Info. Comput. **8**, 501–578 (2008).

Huntemann, N., Sanner, C., Lipphardt, B., Tamm, C. and Peik, E., 'Single-Ion Atomic Clock with 3×10^{-18} Systematic Uncertainty', Physical Review Letters **116** (2016) 10.1103/PhysRevLett.116.063001.

Hut, P. and Makino, J., 'The Art of Computational Science The Maya Open Lab School Series Volume 1 Moving Stars Around', (2007).

IG2 ion source package Datasheet, https://rbdinstruments.com/products/ files/ig2.pdf.

Jain, S., Alonso, J., Grau, M. and Home, J. P., 'Quantum simulation with ions in micro-fabricated Penning traps', arXiv:1812.06755 [physics, physics:quant-ph] (2018).

James, D., 'Quantum dynamics of cold trapped ions with application to quantum computation', Applied Physics B: Lasers and Optics **66**, 181–190 (1998) 10.1007/s003400050373.

Johnson, K. G., Wong-Campos, J. D., Restelli, A., Landsman, K. A., Neyenhuis, B., Mizrahi, J. and Monroe, C., 'Active stabilization of ion trap radiofrequency potentials', Review of Scientific Instruments **87**, 053110 (2016) 10.1063/1.4948734.

Kalis, H., 'Initialization of quantum states in a two-dimensional ion-trap array', PhD thesis (Albert-Ludwigs-Universität, 2017), 10.6094/UNIFR/12723.

Kalis, H., Hakelberg, F., Wittemer, M., Mielenz, M., Warring, U. and Schaetz, T., 'Motional-mode analysis of trapped ions', Physical Review A **94** (2016) 10.1103/PhysRevA.94.023401.

Kelleher, D. E. and Podobedova, L. I., 'Atomic Transition Probabilities of Sodium and Magnesium. A Critical Compilation', Journal of Physical and Chemical Reference Data **37**, 267–706 (2008) 10.1063/1.2735328.

Kiefer, P., 'Aufbau und Charakterisierung eines PPLN-basierten Lasersystems zur Kühlung von Mg-Ionen', Bachelor Thesis (Albert-Ludwigs-Universität, Freiburg, Aug. 2013).

Kiefer, P., 'Floquet Dynamics in a two-dimensional Ion Trap Array', PhD Thesis in preparation (Albert-Ludwigs-Universität, Freiburg, 2019).

Kiefer, P., Hakelberg, F., Wittemer, M., Bermúdez, A., Porras, D., Warring, U. and Schaetz, T., 'Floquet-Engineered Vibrational Dynamics in a Two-Dimensional Array of Trapped Ions', Physical Review Letters **123** (2019) 10.1103/PhysRevLett.123.213605.

Kielpinski, D., Monroe, C. and Wineland, D. J., 'Architecture for a large-scale ion-trap quantum computer', Nature **417**, 709–711 (2002) 10.1038/nature00784.

Kim, K., Chang, M.-S., Korenblit, S., Islam, R., Edwards, E. E., Freericks, J. K., Lin, G.-D., Duan, L.-M. and Monroe, C., 'Quantum simulation of frustrated Ising spins with trapped ions', Nature **465**, 590–593 (2010) 10.1038/nature09071.

Knight, R. D., 'Storage of ions from laser-produced plasmas', Applied Physics Letters **38**, 221–223 (1981) 10.1063/1.92315.

Kumph, M., Holz, P., Langer, K., Meraner, M., Niedermayr, M., Brownnutt, M. and Blatt, R., 'Operation of a planar-electrode ion-trap array with adjustable RF electrodes', New Journal of Physics **18**, 023047 (2016) 10.1088/1367-2630/18/2/023047.

Kumph, M., Brownnutt, M. and Blatt, R., 'Two-dimensional arrays of radio-frequency ion traps with addressable interactions', New Journal of Physics **13**, 073043 (2011) 10.1088/1367-2630/13/7/073043.

Kwong, V. H. S., Gibbons, T. T., Fang, Z., Jiang, J., Knocke, H., Jiang, Y., Ruger, B., Huang, S., Braganza, E., Clark, W. and Gardner, L. D., 'Experimental apparatus for production, cooling, and storing multiply charged ions for charge-transfer measurements', Review of Scientific Instruments **61**, 1931–1939 (1990) 10.1063/1.1141118.

Labaziewicz, J., Ge, Y., Antohi, P., Leibrandt, D., Brown, K. R. and Chuang, I. L., 'Suppression of Heating Rates in Cryogenic Surface-Electrode Ion Traps', Physical Review Letters **100** (2008) 10.1103/PhysRevLett.100.013001.

Langer, C., Ozeri, R., Jost, J., Chiaverini, J., DeMarco, B., Ben-Kish, A., Blakestad, R., Britton, J., Hume, D., Itano, W., Leibfried, D., Reichle, R., Rosenband, T., Schaetz, T., Schmidt, P. and Wineland, D., 'Long-Lived Qubit Memory Using Atomic Ions', Physical Review Letters **95** (2005) 10.1103/PhysRevLett.95.060502.

Langer, C. E., 'High fidelity quantum information processing with trapped ions', PhD thesis (University of Colorado, 2006).

Leibfried, D., Blatt, R., Monroe, C. and Wineland, D., 'Quantum dynamics of single trapped ions', Reviews of Modern Physics **75**, 281–324 (2003) 10.1103/RevModPhys.75.281.

Leibrandt, D. R., Clark, R. J., Labaziewicz, J., Antohi, P., Bakr, W., Brown, K. R. and Chuang, I. L., 'Laser ablation loading of a surface-electrode ion trap', Physical Review A **76** (2007) 10.1103/PhysRevA.76.055403.

Lloyd, S., 'Universal Quantum Simulators', Science **273**, 1073–1078 (1996) 10.1126/science.273.5278.1073.

MacKay, D. J. C., *Information theory, inference, and learning algorithms* (Cambridge University Press, Cambridge, UK ; New York, 2003).

Maunz, P. and Blain, M. G., *(Personal communication)*, 2013.

Maunz, P. and Blain, M. G., *(Personal communication)*, Apr. 2016.

Mehta, K. K., Bruzewicz, C. D., McConnell, R., Ram, R. J., Sage, J. M. and Chiaverini, J., 'Integrated optical addressing of an ion qubit', Nature Nanotechnology **11**, 1066–1070 (2016) 10.1038/nnano.2016.139.

Mielenz, M., 'Two-dimensional arrays of individually controlled ions', PhD thesis (Albert-Ludwigs-Universität, Freiburg, 2016).

Mielenz, M., Kalis, H., Wittemer, M., Hakelberg, F., Warring, U., Schmied, R., Blain, M., Maunz, P., Moehring, D. L., Leibfried, D. and Schaetz, T., 'Arrays of individually controlled ions suitable for two-dimensional quantum simulations', Nature Communications **7**, 11839 (2016) 10.1038/ncomms11839.

Moehring, D. L., Highstrete, C., Stick, D., Fortier, K. M., Haltli, R., Tigges, C. and Blain, M. G., 'Design, fabrication and experimental demonstration of junction surface ion traps', New Journal of Physics **13**, 075018 (2011) 10.1088/1367-2630/13/7/075018.

Mølhave, K. and Drewsen, M., 'Formation of translationally cold MgH^+ and MgD^+ molecules in an ion trap', Physical Review A **62** (2000) 10.1103/PhysRevA.62.011401.

Mount, E., Baek, S.-Y., Blain, M., Stick, D., Gaultney, D., Crain, S., Noek, R., Kim, T., Maunz, P. and Kim, J., 'Single qubit manipulation in a microfabricated surface electrode ion trap', New Journal of Physics **15**, 093018 (2013) 10.1088/1367-2630/15/9/093018.

Müller, D., Anderson, D. Z., Grow, R. J., Schwindt, P. D. D. and Cornell, E. A., 'Guiding Neutral Atoms Around Curves with Lithographically Patterned Current-Carrying Wires', Physical Review Letters **83**, 5194–5197 (1999) 10.1103/PhysRevLett.83.5194.

Neuhauser, W., Hohenstatt, M., Toschek, P. and Dehmelt, H., 'Optical-sideband cooling of visible atom cloud confined in parabolic well', Physical Review Letters **41**, 233 (1978).

Nicolet, A., 'An Introduction To The Boundary Element Method In Electromagnetism: Physical Basis And Applications', WIT Transactions on Modelling and Simulation **9**, 99–108 (1995).

Nielsen, M. A. and Chuang, I. L., *Quantum computation and quantum information*, 10th anniversary ed (Cambridge University Press, Cambridge ; New York, 2010).

Nitzsche, L., 'Ablation Loading of Mg^+ in a surface-electrode trap', Masters thesis (Albert-Ludwigs-Universität, Freiburg, May 2017).

Oliveira, M. H. and Miranda, J. A., 'Biot-Savart-like law in electrostatics', European Journal of Physics **22**, 31–38 (2001) 10.1088/0143-0807/22/1/304.

Ospelkaus, C., Warring, U., Colombe, Y., Brown, K. R., Amini, J. M., Leibfried, D. and Wineland, D. J., 'Microwave quantum logic gates for trapped ions', Nature **476**, 181–184 (2011) 10.1038/nature10290.

Pearson, C. E., Leibrandt, D. R., Bakr, W. S., Mallard, W. J., Brown, K. R. and Chuang, I. L., 'Experimental investigation of planar ion traps', Physical Review A **73** (2006) 10.1103/PhysRevA.73.032307.

Peng, Q., McMurry, S. and Coey, J., 'Axial magnetic field produced by axially and radially magnetized permanent rings', Journal of Magnetism and Magnetic Materials **268**, 165–169 (2004) 10.1016/S0304-8853(03)00494-3.

Porras, D. and Cirac, J. I., 'Effective Quantum Spin Systems with Trapped Ions', Physical Review Letters **92** (2004) 10.1103/PhysRevLett.92.207901.

Porras, D., Marquardt, F., von Delft, J. and Cirac, J. I., 'Mesoscopic spin-boson models of trapped ions', Physical Review A **78** (2008) 10.1103/PhysRevA.78.010101.

Ramsey, N. F., 'A Molecular Beam Resonance Method with Separated Oscillating Fields', Physical Review **78**, 695–699 (1950) 10.1103/PhysRev.78.695.

Rasmussen, C. E. and Williams, C. K. I., *Gaussian processes for machine learning*, Adaptive computation and machine learning, OCLC: ocm61285753 (MIT Press, Cambridge, Mass, 2006).

Rattanasonti, H., Srinivasan, P., Kraft, M., Sterling, R. C., Weidt, S., Lake, K., Webster, S. C. and Hensinger, W. K., 'Microfabricated two-dimensional (2D) hexagonal lattice trap', SENSORS, 2013 IEEE (2013), pp. 1–4.

Rokhlin, V., 'Rapid solution of integral equations of classical potential theory', Journal of Computational Physics **60**, 187–207 (1985) 10.1016/0021-9991(85)90002-6.

Roushan, P., Neill, C., Megrant, A., Chen, Y., Babbush, R., Barends, R., Campbell, B., Chen, Z., Chiaro, B., Dunsworth, A., Fowler, A., Jeffrey, E., Kelly, J., Lucero, E.,

Mutus, J., O'Malley, P. J. J., Neeley, M., Quintana, C., Sank, D., Vainsencher, A., Wenner, J., White, T., Kapit, E., Neven, H. and Martinis, J., 'Chiral ground-state currents of interacting photons in a synthetic magnetic field', Nature Physics **13**, 146–151 (2017) 10.1038/nphys3930.

Ruster, T., Schmiegelow, C. T., Kaufmann, H., Warschburger, C., Schmidt-Kaler, F. and Poschinger, U. G., 'A long-lived Zeeman trapped-ion qubit', Applied Physics B **122**, 254 (2016) 10.1007/s00340-016-6527-4.

Sakurai, J. J., *Modern quantum mechanics*, edited by S. F. Tuan, Rev. ed (Addison-Wesley Pub. Co, Reading, Mass, 1994).

Schaetz, T., Friedenauer, A., Schmitz, H., Petersen, L. and Kahra, S., 'Towards (scalable) quantum simulations in ion traps', Journal of Modern Optics **54**, 2317–2325 (2007) 10.1080/09500340701639631.

Schaetz, T., Leibfried, D., Chiaverini, J., Barrett, M., Britton, J., DeMarco, B., Itano, W., Jost, J., Langer, C. and Wineland, D., 'Towards a scalable quantum computer/simulator based on trapped ions', Applied Physics B **79**, 979–986 (2004) 10.1007/s00340-004-1652-x.

Schaetz, T., Monroe, C. R. and Esslinger, T., 'Focus on quantum simulation', New Journal of Physics **15**, 085009 (2013) 10.1088/1367-2630/15/8/085009.

Schaetz, T., 'Kristalline Ionenstrahlen', PhD thesis (Ludwig-Maximilans-Universität, München, June 2001).

Schmied, R., 'Electrostatics of gapped and finite surface electrodes', New Journal of Physics **12**, 023038 (2010) 10.1088/1367-2630/12/2/023038.

Schmied, R., Wesenberg, J. H. and Leibfried, D., 'Optimal Surface-Electrode Trap Lattices for Quantum Simulation with Trapped Ions', Physical Review Letters **102** (2009) 10.1103/PhysRevLett.102.233002.

Schmied, R., Wesenberg, J. H. and Leibfried, D., 'Quantum simulation of the hexagonal Kitaev model with trapped ions', New Journal of Physics **13**, 115011 (2011) 10.1088/1367-2630/13/11/115011.

Schmitz, H., Friedenauer, A., Schneider, C., Matjeschk, R., Enderlein, M., Huber, T., Glueckert, J., Porras, D. and Schaetz, T., 'The "arch" of simulating quantum spin systems with trapped ions', Applied Physics B **95**, 195–203 (2009) 10.1007/s00340-009-3455-6.

Schmitz, H., Matjeschk, R., Schneider, C., Glueckert, J., Enderlein, M., Huber, T. and Schaetz, T., 'Quantum Walk of a Trapped Ion in Phase Space', Physical Review Letters **103** (2009) 10.1103/PhysRevLett.103.090504.

Schneider, C., Porras, D. and Schaetz, T., 'Experimental quantum simulations of many-body physics with trapped ions', Reports on Progress in Physics **75**, 024401 (2012) 10.1088/0034-4885/75/2/024401.

Schnell, S., 'Motional coherence of a single trapped ion in the classical regime', Masters thesis (Albert-Ludwigs-Universität, Freiburg, Aug. 2018).

Sedlacek, J. A., Greene, A., Stuart, J., McConnell, R., Bruzewicz, C. D., Sage, J. M. and Chiaverini, J., 'Distance scaling of electric-field noise in a surface-electrode ion trap', Physical Review A **97** (2018) 10.1103/PhysRevA.97.020302.

Seidelin, S., Chiaverini, J., Reichle, R., Bollinger, J., Leibfried, D., Britton, J., Wesenberg, J., Blakestad, R., Epstein, R., Hume, D., Itano, W., Jost, J., Langer, C., Ozeri, R., Shiga, N. and Wineland, D., 'Microfabricated Surface-Electrode Ion Trap for Scalable Quantum Information Processing', Physical Review Letters **96** (2006) 10.1103/PhysRevLett.96.253003.

Shin, Y., Sanner, C., Jo, G.-B., Pasquini, T. A., Saba, M., Ketterle, W., Pritchard, D. E., Vengalattore, M. and Prentiss, M., 'Interference of Bose-Einstein condensates split with an atom chip', Physical Review A **72** (2005) 10.1103/PhysRevA.72.021604.

Slichter, D. H., Verma, V. B., Leibfried, D., Mirin, R. P., Nam, S. W. and Wineland, D. J., 'UV-sensitive superconducting nanowire single photon detectors for integration in an ion trap', Optics Express **25**, 8705 (2017) 10.1364/OE.25.008705.

Sterling, R. C., Rattanasonti, H., Weidt, S., Lake, K., Srinivasan, P., Webster, S. C., Kraft, M. and Hensinger, W. K., 'Fabrication and operation of a two-dimensional ion-trap lattice on a high-voltage microchip', Nature Communications **5**, 4637 (2014) 10.1038/ncomms4637.

Stick, D., Fortier, K. M., Haltli, R., Highstrete, C., Moehring, D. L., Tigges, C. and Blain, M. G., 'Demonstration of a microfabricated surface electrode ion trap', arXiv:1008.0990 [physics, physics:quant-ph] (2010).

Stick, D., Hensinger, W. K., Olmschenk, S., Madsen, M. J., Schwab, K. and Monroe, C., 'Ion trap in a semiconductor chip', Nature Physics **2**, 36–39 (2006) 10.1038/nphys171.

Ströhle, J., 'Speicherung von Coulomb Kristallen in einer Oberflächen Paul-Falle', Diploma thesis (Ludwig-Maximilans-Universität, München, 2011).

Tabakov, B., Benito, F., Blain, M., Clark, C. R., Clark, S., Haltli, R. A., Maunz, P., Sterk, J. D., Tigges, C. and Stick, D., 'Assembling a Ring-Shaped Crystal in a Microfabricated Surface Ion Trap', Physical Review Applied **4** (2015) 10.1103/PhysRevApplied.4.031001.

Talukdar, I., Gorman, D. J., Daniilidis, N., Schindler, P., Ebadi, S., Kaufmann, H., Zhang, T. and Häffner, H., 'Implications of surface noise for the motional coherence of trapped ions', Physical Review A **93** (2016) 10.1103/PhysRevA.93.043415.

Tan The Pham, P., 'A general-purpose pulse sequencer for quantum computing', Masters thesis (Massachusetts Institute of Technology, Cambridge, Feb. 2005).

Tec, J., González, C., García, M., Narváez, L. and Canché, M., 'Homemade Antennas Implementation: A Comparative Analysis of the Quality of Service', **9**, 8 (2012).

Vierhub-Lorenz, V., '2D-Quantensysteme in Oberflächenfallen Aufbau und charakterisierung einer Abbildungsoptik für Magnesium Ionen', Bachelor thesis (Albert-Ludwigs-Universität, Freiburg, May 2016).

Warring, U., Ospelkaus, C., Colombe, Y., Brown, K. R., Amini, J. M., Carsjens, M., Leibfried, D. and Wineland, D. J., 'Techniques for microwave near-field quantum control of trapped ions', Physical Review A **87** (2013) 10.1103/PhysRevA.87.013437.

Warring, U., Ospelkaus, C., Colombe, Y., Jördens, R., Leibfried, D. and Wineland, D. J., 'Individual-Ion Addressing with Microwave Field Gradients', Physical Review Letters **110** (2013) 10.1103/PhysRevLett.110.173002.

Wesenberg, J. H., 'Electrostatics of surface-electrode ion traps', Physical Review A **78** (2008) 10.1103/PhysRevA.78.063410.

Wilson, A. C., Colombe, Y., Brown, K. R., Knill, E., Leibfried, D. and Wineland, D. J., 'Tunable spin–spin interactions and entanglement of ions in separate potential wells', Nature **512**, 57–60 (2014) 10.1038/nature13565.

Wineland, D. J., Drullinger, R. E. and Walls, F. L., 'Radiation-pressure cooling of bound resonant absorbers', Physical Review Letters **40**, 1639 (1978).

Wineland, D. J., Monroe, C., Itano, W. M., Leibfried, D., King, B. E. and Meekhof, D. M., 'Experimental Issues in Coherent Quantum-State Manipulation of Trapped Atomic Ions', J.Res.Natl.Inst.Stand.Tech. (1998).

Wineland, D. J. and Dehmelt, H., 'Proposed 10^{14} $\Delta\nu < \nu$ Laser Fluorescence Spectroscopy on Tl+ Mono-Ion Oscillator III', Bulletin of the American Physical Society, 637 (1975).

Wineland, D. J. and Itano, W. M., 'Laser cooling of atoms', Physical Review A **20**, 1521 (1979).

Wittemer, M., 'Motional Control of Ions in a Triangular Trap Array', Masters thesis (Albert-Ludwigs-Universität, Freiburg, 2015).

Wittemer, M., Hakelberg, F., Kiefer, P., Schröder, J.-P., Fey, C., Schützhold, R., Warring, U. and Schaetz, T., 'Phonon Pair Creation by Inflating Quantum Fluctuations in an Ion Trap', Physical Review Letters **123** (2019) 10.1103/PhysRevLett.123.180502.

Yao, N., Jiang, L., Gorshkov, A., Maurer, P., Giedke, G., Cirac, J. and Lukin, M., 'Scalable architecture for a room temperature solid-state quantum information processor', Nature Communications **3** (2012) 10.1038/ncomms1788.

Zähringer, F., Kirchmair, G., Gerritsma, R., Solano, E., Blatt, R. and Roos, C. F., 'Realization of a Quantum Walk with One and Two Trapped Ions', Physical Review Letters **104** (2010) 10.1103/PhysRevLett.104.100503.

Zhang, J., Pagano, G., Hess, P. W., Kyprianidis, A., Becker, P., Kaplan, H., Gorshkov, A. V., Gong, Z.-X. and Monroe, C., 'Observation of a many-body dynamical phase transition with a 53-qubit quantum simulator', Nature **551**, 601–604 (2017) 10.1038/nature24654.

Zimmermann, K., Okhapkin, M. V., Herrera-Sancho, O. A. and Peik, E., 'Laser ablation loading of a radiofrequency ion trap', Applied Physics B **107**, 883–889 (2012) 10.1007/s00340-012-4884-1.